TITLE

The tumor microenvironment drives transcriptional phenotypes and their plasticity in metastatic pancreatic cancer

AUTHORS

Srivatsan Raghavan[1,2,3,4]*, Peter S. Winter[1,2,5,6]*#, Andrew W. Navia[1,2,5,6,7]*, Hannah L. Williams[1,3]*, Alan DenAdel[8,9], Radha L. Kalekar[1,2], Jennyfer Galvez-Reyes[2,5,6], Kristen E. Lowder[1,2], Nolawit Mulugeta[2,5,6], Manisha S. Raghavan[1,2], Ashir A. Borah[2], Kevin S. Kapner[1,2], Sara A. Väyrynen[1], Andressa Dias Costa[1,3], Raymond W.S. Ng[1,2], Junning Wang[1], Emma Reilly[1], Dorisanne Y. Ragon[1], Lauren K. Brais[1], Alex M. Jaeger[6], Liam F. Spurr[1,2], Yvonne Y. Li[1,2], Andrew D. Cherniack[1,2,3], Isaac Wakiro[1], Asaf Rotem[1,2,10], Bruce E. Johnson[1,3,4,10], James M. McFarland[2], Ewa T. Sicinska[3,11], Tyler E. Jacks[6], Thomas E. Clancy[1,3,12], Kimberly Perez[1,3,4], Douglas A. Rubinson[1,3,4], Kimmie Ng[1,3,4], James M. Cleary[1,3,4], Lorin Crawford[8,13,14], Scott R. Manalis[6,15], Jonathan A. Nowak[3,11,16], Brian M. Wolpin[1,3,4]π, William C. Hahn[1,2,3,4]π, Andrew J. Aguirre[1,2,3,4]π#, Alex K. Shalek[2,3,5,6,7,17]π#

AFFILIATIONS

[1]Department of Medical Oncology, Dana-Farber Cancer Institute, Boston, MA
[2]Broad Institute of MIT and Harvard, Cambridge, MA
[3]Harvard Medical School, Boston, MA
[4]Department of Medicine, Brigham and Women's Hospital, Boston, MA
[5]Institute for Medical Engineering & Science, Massachusetts Institute of Technology, Cambridge, MA
[6]Koch Institute for Integrative Cancer Research, Massachusetts Institute of Technology, Cambridge, MA
[7]Department of Chemistry, Massachusetts Institute of Technology, Cambridge, MA
[8]Center for Computational Molecular Biology, Brown University, Providence, RI
[9]Division of Applied Mathematics, Brown University, Providence, RI
[10]Center for Cancer Genomics, Dana-Farber Cancer Institute, Boston, MA
[11]Department of Oncologic Pathology, Dana-Farber Cancer Institute, Boston, MA
[12]Department of Surgery, Brigham and Women's Hospital, Boston, MA
[13]Department of Biostatistics, Brown University, Providence, RI
[14]Microsoft Research New England, Cambridge, MA
[15]Department of Biological Engineering, Massachusetts Institute of Technology, Cambridge, MA
[16]Department of Pathology, Brigham and Women's Hospital, Boston, MA
[17]Ragon Institute of MGH, MIT, and Harvard, Cambridge, MA

*Equal first author contribution
πEqual senior contribution
#To whom correspondence should be addressed:
Peter S. Winter, Ph.D., pswinter@mit.edu
Andrew J. Aguirre, M.D., Ph.D., andrew_aguirre@dfci.harvard.edu
Alex K. Shalek, Ph.D., shalek@mit.edu

SUMMARY

Bulk transcriptomic studies have defined classical and basal-like gene expression subtypes in pancreatic ductal adenocarcinoma (PDAC) that correlate with survival and response to chemotherapy; however, the underlying mechanisms that govern these subtypes and their heterogeneity remain elusive. Here, we performed single-cell RNA-sequencing of 23 metastatic PDAC needle biopsies and matched organoid models to understand how tumor cell-intrinsic features and extrinsic factors in the tumor microenvironment (TME) shape PDAC cancer cell phenotypes. We identify a novel cancer cell state that co-expresses basal-like and classical signatures, demonstrates upregulation of developmental and KRAS-driven gene expression programs, and represents a transitional intermediate between the basal-like and classical poles. Further, we observe structure to the metastatic TME supporting a model whereby reciprocal intercellular signaling shapes the local microenvironment and influences cancer cell transcriptional subtypes. In organoid culture, we find that transcriptional phenotypes are plastic and strongly skew toward the classical expression state, irrespective of genotype. Moreover, we show that patient-relevant transcriptional heterogeneity can be rescued by supplementing organoid media with factors found in the TME in a subtype-specific manner. Collectively, our study demonstrates that distinct microenvironmental signals are critical regulators of clinically relevant PDAC transcriptional states and their plasticity, identifies the necessity for considering the TME in cancer modeling efforts, and provides a generalizable approach for delineating the cell-intrinsic versus -extrinsic factors that govern tumor cell phenotypes.

KEYWORDS

Pancreatic cancer, Single-cell RNA sequencing, Cancer cell states, Transcriptional phenotypes, Plasticity, Patient-derived organoid models, Genotype-phenotype relationships, Tumor microenvironment, Liver metastases, Tumor heterogeneity

INTRODUCTION

Classification of human malignancies by genotype has provided important insights into tumor biology as well as a framework to guide therapeutic selection in many cancers (Hyman et al., 2017). However, tumors also exhibit clinically relevant transcriptional variation that can influence malignant progression and therapeutic response. The application of single-cell RNA-sequencing (scRNA-seq) to tumor specimens has afforded a means to characterize the malignant and non-malignant cellular components of the tumor microenvironment (TME) and their heterogeneity at unprecedented resolution (Kim et al., 2018; Patel et al., 2014; Puram et al., 2017; Sade-Feldman et al., 2019; Suva and Tirosh, 2019; Tirosh et al., 2016a; van Galen et al., 2019; Venteicher et al., 2017). These analytical approaches have further enabled the re-examination of existing transcriptional taxonomies, revealing structured heterogeneity within malignant populations and reframing our understanding of bulk measurements in multiple cancers (Filbin et al., 2018; Hovestadt et al., 2019; Neftel et al., 2019; Patel et al., 2014; Tirosh et al., 2016b; Venteicher et al., 2017).

The phenotypic variability observed in human tumors often reflects the underlying cancer cell genetics. Specific mutations can program cancer cell states and, in some cases, serve as biomarkers for treatment (Filbin et al., 2018; Hovestadt et al., 2019; van Galen et al., 2019; Venteicher et al., 2017). Yet, in other instances, transcriptional phenotypes are not strongly associated with specific mutational patterns (Nam et al., 2021). In these tumors, cell-extrinsic TME interactions may influence malignant cellular attributes, but our understanding of reciprocal signaling between malignant cells and the TME is rudimentary. Mapping the cell-intrinsic and -extrinsic factors that impact tumor cell states and determining which ones drive phenotypic transitions would yield important insights into the biologic basis for clinical disease phenotypes and drug resistance.

For pancreatic ductal adenocarcinoma (PDAC), bulk RNA-seq profiling has defined two major transcriptional programs, basal-like/squamous (hereafter referred to as basal) and classical. The basal subtype is strongly associated with a poorer prognosis and greater treatment resistance (Aguirre et al., 2018; Aung et al., 2018; Bailey et al., 2016; Cancer Genome Atlas Research Network, 2017; Chan-Seng-Yue et al., 2020; Collisson et al., 2011; Connor et al., 2019; Moffitt et al., 2015; O'Kane et al., 2020; Porter et al., 2019; Tiriac et al., 2018), but the roles of cell-intrinsic and -extrinsic factors in determining these cell states and their sensitivity to different therapies are not well understood. A limited number of genomic alterations, including *TP53* mutational status and *c-MYC* or *KRAS* amplifications, have been associated with the more therapy-resistant basal state (Bailey et al., 2016; Cancer Genome Atlas Research Network, 2017; Chan-Seng-Yue et al., 2020; Hayashi et al., 2020; Schleger et al., 2002). Recent studies have also suggested that high levels of KRAS expression and signaling can induce the basal state, but others have demonstrated that basal PDAC cells exhibit RAS-independence (Chan-Seng-Yue et al., 2020; Collisson

et al., 2011; Miyabayashi et al., 2020; Muzumdar et al., 2017). These findings suggest that while genomic activation of *KRAS* plays an important role in oncogenesis, other non-genetic and microenvironmental factors may also be critical in regulating downstream cellular states.

Although the majority of patients with PDAC present with and succumb to metastatic disease (Siegel et al., 2020), our current understanding of PDAC is largely derived from resected primary tumors (Aguirre et al., 2018; Cancer Genome Atlas Research Network, 2017; Siegel et al., 2020). While several recent studies have described the desmoplastic stromal microenvironment and immune infiltration in primary PDAC (Balachandran et al., 2019; Bernard et al., 2019; Biffi et al., 2019; Elyada et al., 2019; Ligorio et al., 2019; Ohlund et al., 2017), we lack a detailed characterization of the immune and stromal cells that constitute metastatic PDAC lesions. The local TME in the pancreas is likely different from metastatic sites in other organs (Ho et al., 2020), and given the strong association of transcriptional subtype with survival and drug resistance (Aguirre et al., 2018; Aung et al., 2018; Bailey et al., 2016; Cancer Genome Atlas Research Network, 2017; Chan-Seng-Yue et al., 2020; Collisson et al., 2011; Connor et al., 2019; Moffitt et al., 2015; O'Kane et al., 2020; Porter et al., 2019; Tiriac et al., 2018), understanding whether specific inputs from the metastatic niche can specify transcriptional phenotype is of great importance to targeting therapeutic resistance in PDAC.

To better understand the interplay between genetics, transcriptional state, and the metastatic TME, we developed and employed an optimized translational workflow to perform both high-resolution profiling of PDAC patient tissue using scRNA-seq (Gierahn et al., 2017; Hughes et al., 2020) and derivation of matched organoid models (Boj et al., 2015; Tiriac et al., 2018) from the same metastatic core needle biopsy. Using matched *in vivo* observations and *ex vivo* experimental studies, we describe a tumor cell atlas of metastatic PDAC, identify a new intermediate transitional PDAC cancer cell state, uncover distinct site- and subtype-specific TMEs, and demonstrate that microenvironmental signals are critical regulators of transcriptional subtypes and their plasticity.

RESULTS

A clinical pipeline for matched single-cell profiling and organoid model generation

We established a pipeline for collecting core needle biopsies from patients with metastatic PDAC (n=23) to generate matched scRNA-seq profiles and organoid models (**Figure 1A**; **Supplemental Figure S1A**; **Supplemental Table S1**). Most samples were obtained from metastatic lesions residing in the liver (19/23), and the majority (21/23) were analyzed by targeted DNA-sequencing, yielding the expected mutational pattern for this disease (**Figure 1B**) (Aguirre et al., 2018; Bailey et al., 2016; Cancer Genome Atlas Research Network, 2017). Our pipeline generated approximately 1,000 high-quality single cells per biopsy (n=23,042 total cells) and successful early-passage organoid cultures from 70% of patient tumor

135 samples (16/23 samples reaching at least passage 2; **Figure 1B**; **Supplemental Figure S1A**,**B**).
136 Dimensionality reduction and shared nearest neighbor (SNN) clustering of the biopsy cells revealed
137 substantial heterogeneity at the single-cell level (**Supplemental Figure S1C**,**D**; **Methods**). Consistent
138 with other studies of human cancer, we observed patient-specific and admixed clusters of single cells
139 suggesting the presence of both malignant and non-malignant cells in each biopsy (Kim et al., 2018;
140 Puram et al., 2017; Sade-Feldman et al., 2019; Tirosh et al., 2016a; van Galen et al., 2019). To confirm
141 which clusters were comprised of malignant cells, we inferred transcriptome-wide CNVs from our single-
142 cell data as previously described (Patel et al., 2014; Tirosh et al., 2016b). CNV alteration scores
143 separated putative cancerous and non-cancerous cells in each biopsy and demonstrated high
144 concordance with reference targeted DNA-seq (**Figure 1C**; **Supplemental Figure S1E**,**F**). CNV analysis
145 paired with manual inspection of expression patterns for known markers across single cells supported
146 the identification of cancerous cells as well as 11 unique non-cancerous cell types (**Figure 1D**,**E**;
147 **Supplemental Figure S1D-I**; **Supplemental Table S2**). Thus, we established a robust workflow capable
148 of recovering high quality malignant (n=7,740) and non-malignant (n=15,302) populations from metastatic
149 PDAC needle biopsies while also enabling simultaneous generation of matched organoid models.
150

151 **Tumor cell transcriptional subtypes in metastatic PDAC include an intermediate transitional state**
152 We applied principal component analysis (PCA) to examine transcriptional variation across cancer cells
153 from all biopsy samples. CNV-altered cells from one biopsy, PANFR0580, separated from the rest of the
154 samples (**Figure 1B**; **Supplemental Figure S2A**). Based on expression of known neuroendocrine
155 markers (*TTR, CHGA*) and subsequent pathology review we reclassified this sample as a pancreatic
156 neuroendocrine tumor (PanNET) and used it as a non-PDAC reference cell population. Among the
157 remaining 7,078 PDAC cells, we found that genes driving the first 3 PCs were enriched for signatures of
158 epithelial/mesenchymal transition [EMT, PC1, (Groger et al., 2012)], basal/classical state [PC2, (Moffitt
159 et al., 2015)], and cell cycle [PC3, (Tirosh et al., 2016a)] (**Supplemental Figure S2B**). When we scored
160 all malignant cells within our cohort for basal and classical gene expression, we observed that they
161 inhabited a graded continuum of expression states from strongly basal to strongly classical (**Figure 2A**).
162 Correlation analysis across malignant cells revealed 1,909 genes significantly associated with either
163 basal or classical expression scores (**Supplemental Figure S2C**; **Supplemental Table S3**; **Methods**).
164 Inspection of these genes revealed that basal cells are defined by squamous and mesenchymal features
165 and co-express programs associated with transforming growth factor beta (TGF-β) signaling, WNT
166 signaling, and cell cycle progression (Groger et al., 2012; Kim et al., 2017; Tirosh et al., 2016a).
167 Conversely, epithelial and pancreatic lineage programs are enriched in classical subtype PDAC cells
168 (**Supplemental Figure S2D**,**E**).

169 Strikingly, we observed that the basal and classical programs were not mutually exclusive; rather,
170 we identified a large population of cells that co-expressed features of both programs to varying degrees
171 (**Figure 2A**; **Supplemental Figure S3A**,**B**). In developmental contexts, cell state commitment is often a
172 continuous process where mixing/co-expression of state markers indicates state transitions (Nam et al.,
173 2021). Similarly, the large fraction of intermediate co-expressing cells identified in our single-cell
174 snapshots suggests state transitions may be an ongoing and frequent process in human PDAC tumors.
175 We identified 115 genes whose expression was correlated with this co-expressor intermediate state and
176 enriched for developmental, Ras signaling, and inflammation/stress response gene sets (**Figure 2B**;
177 **Supplemental Figure S3C**,**D**; **Supplemental Table S3**; **Methods**). Signatures of RAS signaling were
178 enriched in the intermediate state even compared with basal and classical programs, and, by contrast,
179 classical phenotypes were enriched for Akt-associated gene sets and showed little evidence of EMT or
180 RAS enrichments (**Figure 2A-B**; **Supplemental Figure S2E**).
181 Since this intermediate signature showed enrichment for developmental gene programs, we next
182 assessed whether this signature overlapped with any phenotypes recently reported in the normal
183 pancreas progenitor niche (Qadir et al., 2020). We found that both basal and classical gene expression
184 signatures were expressed by pro-ductal progenitor cells, while the intermediate gene expression
185 program was enriched in an undifferentiated, stress-responsive progenitor population (**Supplemental**
186 **Figure S3E**,**F**) (Qadir et al., 2020). Thus, based on its enrichment for developmental and stress-
187 responsive gene sets, overlap with populations in the normal progenitor niche, and co-expression of basal
188 and classical programs suggestive of a transitional state, we termed this phenotype "Intermediate
189 transitional" (IT) (**Figure 2C**).
190 To further contextualize this cell state, we compared signatures proposed by prior bulk RNA-
191 sequencing studies to clarify potential inter-relationships (Aguirre et al., 2018; Bailey et al., 2016; Chan-
192 Seng-Yue et al., 2020; Collisson et al., 2011; Moffitt et al., 2015). Pairwise correlation of all established
193 signatures in malignant cells revealed that many contribute overlapping information and reflect similar
194 underlying biology within either basal or classical clades, but that the IT signature is unique and not well
195 described by established bulk RNA-seq signatures (**Figure 2D**). Taken together, these findings suggest
196 that malignant PDAC cells organize in a tripartite cell state framework that spans committed basal and
197 classical phenotypes, with considerable signature co-expression in single cells (**Figure 2E**). Similar to
198 the variation in EMT scores observed in basal tumor cells (**Supplemental Figure S3A**) (Chan-Seng-Yue
199 et al., 2020; Connor et al., 2019), we noted heterogeneity among co-expressing cells for the IT program.
200
201 **Multiplex immunofluorescence confirms co-expressing IT cells in metastatic and primary PDAC**

202 To compare to bulk RNA-seq studies, we clustered pseudo-bulk averages of the malignant cells from
203 each biopsy and observed separation of tumors into those that expressed predominantly basal, classical,
204 or IT signatures (**Supplemental Figure S3G-I**). However, individual tumors exhibited significant
205 heterogeneity at the cellular level, with mixing of malignant cell populations expressing at least two and
206 frequently all three cell states within the same patient specimen (**Supplemental Figure S3J**). To validate
207 the extensive heterogeneity and the presence of co-expressing IT cells in our metastatic cohort, we used
208 a subtype-specific multiplex immunofluorescence (mIF) panel to categorize single tumor cells by their
209 patterns of marker detection in 10 matched cases from our single cell study (**Supplemental Figure S4A**;
210 **Supplemental Table S4**; **Methods**). We observed extensive overlap of basal and classical markers
211 within single cells at the protein level, corroborating the existence of co-expressing IT cells using an
212 orthogonal method (**Figure 2F**; **Supplemental Figure S4B**). Encouragingly, we observed significant
213 correlation within subtype (average r = 0.52) as compared to between subtypes (average r = 0.06, P <
214 10^{-7}, Student's T test) using this orthogonal method. We also observed high concordance between the
215 two methods, giving confidence that we are accurately sampling the distribution of states present in each
216 sample (average r = 0.45; **Supplemental Figure S4C**, white dots). As with scRNA-seq, we observed
217 mixing of basal, classical, and IT cells within individual patient specimens by mIF subtyping. The
218 frequency of co-expressing cells was correlated with balanced representation of pure basal and classical
219 phenotypes within individual samples, consistent with the co-expressing IT phenotype as a transitional
220 state (**Figure 2G**). Indeed, none of the tumors evaluated with mIF contained a mix of pure basal and
221 classical phenotypes in the absence of co-expressing IT cells. We also identified co-expressing cells in
222 primary tumor samples which suggests that IT phenotypes may be a general feature of PDAC tumors in
223 both the localized and metastatic settings (**Figure 2H**; **Supplemental Figure S4D**).
224

225 **Microenvironment is dominant to *KRAS* amplifications in determining transcriptional subtype**

226 We next searched for potential molecular regulators of the observed tumor cell transcriptional
227 heterogeneity. In PDAC, the vast majority of tumors harbor clonal *KRAS* point mutations, including all of
228 the PDAC samples in our cohort (**Figure 1B**). While point mutations in *KRAS* do not appear to determine
229 transcriptional subtype, several studies have suggested that amplifications in *KRAS* associate with more
230 basal features (Chan-Seng-Yue et al., 2020; Miyabayashi et al., 2020), while amplifications of lineage
231 transcription factors like *GATA6* associate with classical phenotypes (Chan-Seng-Yue et al., 2020). To
232 assess for such genotype-phenotype relationships in our single-cell cohort, we inferred copy number
233 variation for common PDAC alterations (*KRAS*, *TP53*, *SMAD4*, and *CDKN2A*) and lineage-associated
234 transcription factors (*HNF4G* and *GATA6*) from scRNA-seq expression data using a previously
235 established Hidden Markov model workflow (**Methods**) (Fan et al., 2018; Patel et al., 2014; Tirosh et al.,

236 2016b). Encouragingly, we observed a significant association between single-cell inferred *KRAS* copy
237 number gain and basal phenotypes (*P<0.03* Fisher's exact test), and also between inferred *CDKN2A*
238 copy loss and IT phenotypes (*P<0.003* Fisher's exact test; **Figure 3A**). While we found that cells derived
239 from samples with inferred *KRAS* amplifications had a strong preference for the basal subtype, these
240 cells could still span all three phenotypic categories or be predominantly classical within an individual
241 tumor (**Figure 3B-D**).
242 To further examine this genotype-to-phenotype association, we tested if *KRAS* amplification was
243 sufficient to specify the basal phenotype in an *ex vivo* environment. We initiated patient-derived organoid
244 cultures from matched PDAC biopsies and serially sampled them over time with scRNA-seq (**Figure 1A**).
245 CNV-confirmed "early" organoid cells (first passage measured, n=2,117 cells) derived from *KRAS*-
246 amplified biopsies maintained this genetic alteration in culture (**Figure 3E**, dark red). Despite their genetic
247 stability, cells with inferred *KRAS* amplifications exhibited a profound phenotypic shift from basal *in vivo*
248 to classical *ex vivo* (**Figure 3F**). Although selection of specific clones could play a role in this process,
249 most of these models maintained high CNV similarity to their parent tumor at the early time point. For
250 example, we observed that a CNV-defined clone from PANFR0575 with both *KRAS* and *GATA6*
251 amplifications was plastic and shifted from strongly basal *in vivo* to classical in early organoid culture
252 (**Figure 3G**). These observations provide strong evidence that phenotypic plasticity is an inherent feature
253 of malignant PDAC cells and demonstrate that *KRAS* amplification alone is not sufficient to lock the basal
254 state. Furthermore, they suggest that the tumor microenvironment can influence phenotype independent
255 of genotype in this context.
256
257 **Transcriptional heterogeneity is shaped by the microenvironment**
258 Given this strong phenotypic shift even for genetically similar samples, we next examined how *ex vivo*
259 transcriptional phenotypes differed across our larger organoid cohort relative to their cognate patient
260 samples. Globally, unbiased comparison of all malignant biopsy (7,078 cells) and organoid cells (n=14
261 models, 24,789 cells) revealed unique clusters for each sample and only two clusters that were admixed
262 by donor. These admixed cells exhibited expression programs consistent with non-malignant stromal
263 cells, had low overall CNV scores, and dissipated by later passages (**Supplemental Figure S5A-D**;
264 **Methods**). Overall, samples with high tumor-averaged basal or IT phenotypes exhibited lower rates of
265 long-term organoid propagation beyond passage 2 than models derived from classical tumors, where the
266 majority established long-term cultures (**Figure 4A**). When comparing early passage CNV-confirmed
267 organoids to their cognate patient tissue, culture in an *ex vivo* microenvironment caused greater deviation
268 in transcriptional phenotype than CNV-defined genotype (**Figure 4A**, $P < 10^{-6}$ Student's T test; **Methods**).

269 We next assessed which specific tumor cell attributes contributed to phenotypic divergence in the
270 *ex vivo* microenvironment. As with the *KRAS*-amplified samples, we observed a striking decrease in basal
271 gene expression ($P < 0.000001$) and, to a lesser but still significant extent ($P < 0.001$), the IT program
272 (**Figure 4B**, **top**). By contrast, aggregate classical gene expression remained largely unchanged in
273 organoid conditions (**Figure 4B**, **top**). This loss of basal expression was surprising, given the more
274 clinically aggressive and proliferative nature of basal tumors *in vivo* (**Supplemental Figure S3A**) (Connor
275 et al., 2019; Moffitt et al., 2015). Organoid-specific gene expression features that were not present *in vivo*
276 also emerged, including markers of epithelial identity, oxidative stress response pathways (e.g., NRF2
277 target genes), and amino acid metabolism (hereafter collectively referred to as "organoid-specific" gene
278 expression; **Figure 4B**, **bottom**; **Supplemental Table S5**). In general, models assumed a more classical
279 or organoid-specific phenotype over time in culture regardless of their parent tumor's transcriptional
280 identity (**Figure 4C**). Most models derived from basal or IT tumors exhibited early phenotypic deviation
281 and cessation of growth within 100 days of initiation (e.g., PANFR0552; **Supplemental Figure S5E**) or
282 outgrowth of only a sub-clone in culture (e.g., PANFR0489R; **Supplemental Figure S5F**). Classical
283 tumors, meanwhile, tended to maintain their genotype and phenotype both early in culture and at later
284 passages (e.g., PANFR0631; **Figure 4C**; **Supplemental Figure S5G**, clone A).
285 To better understand the contribution of clonal selection to this process, we performed linked
286 genotype and phenotype assessment from iterative passages. We identified CNV-defined subclones in
287 the parental biopsy and its associated serial organoid samples, and then assessed how the distribution
288 of transcriptional states within each subclonal population evolved over time in culture (**Methods**). In both
289 PANFR0489R and PANFR0575, *KRAS* amplification status remained invariant over time, but we
290 observed significant phenotypic plasticity and clonal selection in both cases. In PANFR0489R, the
291 predominantly basal clones *in vivo* rapidly decreased in abundance while other rarer clones with classical
292 or organoid-specific phenotypes emerged as the dominant ones (**Supplemental Figure S5H**). In
293 contrast, *in vivo* dominant clones from PANFR0575 were largely maintained at early passages but
294 diverged significantly in their phenotype, transiently expressing more classical and organoid-specific
295 phenotypes at passages 2 and 3 before eventually regaining basal transcriptional expression after >100
296 days in culture (**Supplemental Figure S5I**). Notably, the clones that came to dominate in PANFR0575
297 organoid culture (clones D and E, **Supplemental Figure S5I**) carried inferred *TP63* amplifications, a
298 squamous-specifying transcription factor (Somerville et al., 2018), suggesting that certain genotypes,
299 though rare, may still exert a strong effect despite opposing signals from the microenvironment. Taken
300 together, these findings emphasize the importance of optimizing culture conditions and performing deep
301 molecular characterization of patient-derived model systems to ensure faithful representation of the
302 tumor.

303 Divergence from *in vivo* phenotype, despite relative similarity in genotype, suggested that the
304 TME has a strong influence in determining PDAC cellular state. For each biopsy-organoid pair, we used
305 differential expression to nominate transcriptional programs that were present *in vivo* but missing from
306 *ex vivo* culture (**Figure 4D**; **Methods**). Broadly, genes preferentially expressed by malignant cells *in vivo*
307 were related to soluble cytokine signaling, cell-cell communication, and tumor-microenvironment
308 interactions, highlighting the absence of this crosstalk in organoid culture (**Figure 4E**). Hierarchical
309 clustering revealed subtype-dependent expression patterns for these *in vivo*-specific genes (**Figure 4F**;
310 **Supplemental Table S5**). For example, interferon response and EMT genes were significantly
311 upregulated in basal and IT malignant cells *in vivo* (clusters 1 and 2, **Figure 4F**), while genes associated
312 with cell-cell interactions and surface glycoproteins were more strongly expressed in IT and classical
313 cells (cluster 3, **Figure 4F**). Genes related to biological adhesion were more uniform in their expression
314 across the subtypes (cluster 4, **Figure 4F**). The relative absence of these TME-crosstalk genes in
315 organoid culture and their differences in expression across transcriptional subtypes *in vivo* suggest that
316 TME signals may play a role in specifying tumor cell phenotypes.
317
318 **Non-malignant composition of the metastatic microenvironment**
319 The presence of TME-associated expression patterns in cancer cells *in vivo* suggested there may be
320 subtype-dependent structure to, and instructive signaling from, the metastatic TME; however, relatively
321 little is known about the structure and composition of the metastatic microenvironment in PDAC. We first
322 analyzed the non-malignant cells (n=14,811) in the metastatic niche to further subclassify cell types and
323 provide a more complete picture of the immune/stromal composition of metastatic disease (**Figure 5A**).
324 Sub-clustering of T/NK cells revealed 4 cell types—*CD4*+ T, *CD8*+ T, NK, and *CD16*+ (*FCGR3A*+) NK
325 cells—each expressing the corresponding established markers (**Supplemental Figure S6A**,**B**;
326 **Methods**). Similarly, an unsupervised examination within the monocyte/macrophage compartment
327 revealed a tripartite continuum for tumor associated macrophages (TAMs), similar to one recently
328 described in colorectal cancer, comprised of inflammatory *FCN1*+ "monocyte-like" TAMs, *C1QC*+
329 phagocytic TAMs, and *SPP1*+ angiogenesis-associated TAMs (**Supplemental Figure S6C**,**D**;
330 **Supplemental Table S2**) (Zhang et al., 2020; Zilionis et al., 2019). Representative marker expression
331 across all previously described non-malignant cells is summarized in **Supplemental Figure S6E**.
332 Although most samples in our cohort were taken from liver metastases (19/23), several originated
333 from other sites including the omentum, adrenal gland, and peritoneum (**Figure 1B**, **"**other").
334 Interestingly, while we found equal distribution of immune cells among the anatomical sites,
335 mesenchymal cell populations clustered predominantly by the location of the metastatic lesion (**Figure**
336 **5B**,**C**). Excluding adrenal-specific endocrine cells (**Figure 4C**; subset 4, 40 cells), we identified 3

337 mesenchymal subclusters with relatively uniform expression for canonical cancer-associated fibroblast
338 (CAF) markers (**Figure 5C**; **Supplemental Figure S6F**). PCA of these cells revealed a continuum of
339 states along PC2, with uniform expression of the previously described myofibroblast (myCAF) signature
340 (Elyada et al., 2019; Ohlund et al., 2017) but further separating into cells favoring high expression of
341 dermal fibroblast-like genes (PC2 low, *FAP, PRXX1, SFRP2*) or pericyte-like genes (PC2 high, *RGS5,*
342 *MCAM, TBX2*; **Supplemental Figure S6G-I**; **Supplemental Table S2**) (Ascension et al., 2020;
343 Bartoschek et al., 2018; Di Carlo and Peduto, 2018; Hosaka et al., 2016; Pelon et al., 2020; Philippeos
344 et al., 2018). PC3 described a small subset of cells, derived largely from a single tumor (PANFR0489R),
345 that were highly consistent with the previously established inflammatory fibroblast (iCAF) program
346 (Elyada et al., 2019; Ohlund et al., 2017) (**Supplemental Figure S6H-J**).
347 While tumors from each location contained both mesenchymal subsets, we noted a strong organ-
348 specific skewing along PC2 with pericyte-like phenotypes being preferentially associated with liver
349 biopsies (**Figure 5D**,**E**; **Supplemental Figure S6K**). To validate these observations in larger cohorts, we
350 assessed bulk RNA-seq datasets using these dermal fibroblast- and pericyte-like CAF signature scores
351 and observed a similar predilection for the pericyte-like expression program in liver metastases (**Figure**
352 **5F**; **Methods**). Interestingly, tumors in the pancreas (n = 153 samples) favored expression of the dermal
353 fibroblast-like program, suggesting a substantially different mesenchymal microenvironment in primary
354 versus liver metastatic PDAC (**Figure 5F**). Thus, we observed diverse immune and stromal cell types in
355 the metastatic TME and identified site specific mesenchymal features unique to the liver metastatic niche
356 compared with primary disease.
357
358 **Transcriptional subtypes associate with distinct immune microenvironments**
359 After cataloging the cell types in the metastatic TME, we searched for associations between malignant
360 subtype and the immune microenvironment. For each tumor sample, we first computed the fractional
361 representation of each non-malignant cell type per biopsy. Five tumors were excluded from this analysis
362 on the basis of low cell counts (<200 cells) or indeterminant transcriptional subtype (PanNET or no tumor
363 cells captured; **Supplemental Figure S6L**). To describe the overall microenvironmental composition for
364 each tumor, we applied Simpson's diversity index, a measure of biodiversity commonly used in ecology
365 to describe the number of species (cell types) present in an ecosystem (tumor) and their relative
366 abundance. We observed that tumors with more classical or IT phenotypes exhibited greater
367 microenvironmental diversity, while strongly basal tumors had a more homogeneous TME (**Figure 6A**).
368 Hierarchical clustering over the relative abundance of each non-malignant subset across the biopsy
369 cohort revealed the specific cell types driving these overall diversity differences (**Figure 6B**,**C**).
370 Specifically, C1QC+ TAMs dominated the microenvironments of strongly basal tumors, and both CD8+

371 and CD4+ T cells were significantly depleted in basal contexts compared to the rest of the samples in the
372 cohort (**Figure 6C**,**D**). T cells most often originated from biopsies with higher IT malignant fractions
373 (**Figure 6B**,**C**) and their abundance was positively correlated with this malignant phenotype in our cohort
374 (**Figure 6E**). We also broadly observed these patterns within TCGA bulk RNA-sequencing data of other
375 epithelial malignancies (Cancer Genome Atlas Research et al., 2013), where we observed evidence for
376 reduced levels of immune-related gene expression in tumors with high basal/squamous gene expression
377 (**Supplemental Figure S6M**, cluster 4). Taken together, these findings suggest coordinated interactions
378 between malignant phenotypes and the local TME with decreased immune cell diversity and a greater
379 degree of immune exclusion associated with basal contexts (**Figure 6F**).
380

381 **The soluble microenvironment shapes PDAC cellular phenotypes**

382 Based on our observations that: 1) the microenvironment influences malignant phenotype independent
383 of genotype; 2) gene expression programs associated with cytokine signaling, EMT, and cell-cell
384 interaction are enriched *in vivo* but missing from cells cultured as organoids; and, 3) malignant states and
385 immune cell infiltration are coordinated in a subtype-specific manner, we hypothesized that incorporation
386 of soluble factors specific to the TME of each transcriptional subtype may drive tumor cell state shifts
387 (**Figure 7A**). Complete PDAC organoid media (**Supplemental Table S6**) (Boj et al., 2015; Tiriac et al.,
388 2018) contains various growth factors that could skew malignant transcriptional state, so we first tested
389 the effects of withdrawing various soluble factors. We cultured four organoid models in media without any
390 additives ("Minimal" media, containing only Glutamax, anti-microbials, HEPES buffer, and Advanced
391 DMEM/F12 media; **Figure 7B**; **Supplemental Table S6**; **Methods**). We observed a robust increase in
392 basal gene expression and a decrease in organoid-specific gene expression in specimens cultured for 6
393 days in minimal media relative to those in complete organoid media ("Complete", **Figure 7B**). Although
394 we found that the fraction of cycling cells in minimal media decreased, the organoids continued to grow
395 under these conditions and exhibited stable CNV profiles, indicating that these responses were unlikely
396 to be driven by acute selection (**Supplemental Figure S7A**,**B**). We cultured one model, PANFR0562, in
397 minimal media for a longer duration and observed that the phenotypic distribution shifted even further
398 toward IT and basal phenotypes (**Figure 7C**), demonstrating that recovery of all three states is possible
399 *ex vivo*. Since minimal medium lacks both serum and mitogens to support prolonged cell growth, we also
400 tested whether culturing organoids in a reduced organoid media formulation ("OWRNA", complete
401 organoid media with removal of WNT3A, RSPONDIN-1, NOGGIN, and A83-01; **Supplemental Table**
402 **S6**; **Methods**) supported proliferation while allowing expression of basal and IT phenotypes. We found
403 that organoids maintained under OWRNA conditions began to express basal and IT features while also
404 strengthening classical gene expression and continuing to proliferate (**Supplemental Figure S7C**).

405 To assess whether these microenvironment-driven effects on transcriptional states were specific
406 to organoid models or also observed in other cell culture models, we examined PDAC cell lines, as these
407 are also commonly used to study PDAC biology but are grown in different culture conditions. We
408 compared bulk RNA expression data from patient tumors (n=219) (Aguirre et al., 2018; Cancer Genome
409 Atlas Research Network, 2017), our own organoid cohort (n=44), and established cell lines (n=49, CCLE)
410 (Barretina et al., 2012; Ghandi et al., 2019) and observed strong culture method-dependent phenotypic
411 skews wherein most organoid models expressed classical phenotypes while cell lines exhibited basal
412 phenotypes (**Supplemental Figure S7D**,**E**). This observation suggests neither platform accurately
413 represents the full repertoire of transcriptional states seen in patients and provides additional evidence
414 that environmental conditions can profoundly influence transcriptional state. We ruled out the effects of
415 extracellular matrix dimensionality from media formulation by culturing established 3-dimensional (3D)
416 organoid models as 2-dimensional (2D) cell lines on tissue culture plastic in the same organoid media—
417 this had little effect on transcriptional subtype across the models tested (**Supplemental Figure S7F**).
418 Next, we took each model type (cell lines and organoids) and cultured it in the reciprocal media condition
419 to ask whether media alone could influence transcriptional subtype. Organoid cells grown in standard
420 cancer cell line medium ("RP10", RPMI-1640 with 10% fetal bovine serum) gained expression of basal
421 programs (**Supplemental Figure S7C**), while CFPAC1 (an established PDAC cell line) lost basal and
422 classical features and gained organoid-specific gene expression when grown in complete organoid media
423 ("Complete media", **Supplemental Figure S7G**). Taken together, these findings demonstrate that the
424 microenvironment is an instrumental contributor to shaping malignant phenotypes in PDAC. Moreover,
425 the cell state plasticity suggests the possibility of testing subtype-specific conditions to support the full
426 repertoire of *in vivo* phenotypes.
427

428 **Applying subtype-specific TME signals drives patient-relevant subtype heterogeneity**

429 Finally, we hypothesized that specific factors from subtype-specific TMEs could recover clinically relevant
430 transcriptional heterogeneity *ex vivo* (**Figure 7A**). *In vivo,* the secreted factor milieu surrounding tumor
431 cells originates from at least two sources that may influence malignant phenotype: tumor cells themselves
432 ("autocrine" factors) and non-tumor cells ("paracrine" factors, **Figure 7A**). First, to nominate possible
433 autocrine signals, we identified tumor cell secreted factors specific to the three subtypes and noted
434 distinct cytokines expressed by each (**Figure 7D**; **Supplemental Table S7**; **Methods**). Since malignant
435 cells derived from predominantly basal and IT tumors lose their phenotype in organoid culture, we first
436 tested factors specific to IT and basal states *in vivo*. *TGFB2* was the top differentially expressed secreted
437 factor shared by tumor cells in both basal and IT TMEs (**Figure 7D**). Organoids cultured with TGF-β
438 ligands exhibited a loss of classical expression programs and a near complete shift toward IT and basal

phenotypes, matching what we observed *in vivo* (**Figure 7E**). Reemergence of basal phenotypes in both minimal media (**Figure 7C**), and TGF-β conditions (**Figure 7E**) suggest that different types of microenvironmental pressure can lead to the basal phenotype. Moreover, they suggest that culture conditions can be tuned to achieve compositional differences spanning pure classical, heterogenous, and pure basal phenotypes, akin to those seen *in vivo*.

Using a similar approach, we next searched for differentially expressed paracrine factors supplied by the non-tumor cells in the TME from each subtype. Here, we noted an increasing number of differentially expressed factors in IT and basal contexts, likely reflecting the specific immune cell type enrichments: TAM and T cell dominant in basal and IT TMEs, respectively (**Figure 6A-C**; **Figure 7F**; **Supplemental Table S7**). We then mapped each subtype-specific paracrine factor to its cognate cell type to summarize the overall cell type and secreted factor combinations that shape the subtype-specific TMEs in metastatic PDAC (**Figure 7G**). Interestingly, we found that *IFNG* originating from *CD8+* T cells was most highly expressed in the IT TME (**Figure 7F**,**G**). This was consistent with a relatively higher T cell fraction in IT tumors (**Figure 6B**,**F**) and the relative increase in IFN responsive gene expression in IT and basal tumor cells (**Figure 4E**,**F**). Given these corroborating correlative data, we directly tested whether exogenous IFNγ could induce transcriptional plasticity towards an IT state. Cells exposed to IFNγ showed a dramatic shift toward the IT state with concomitant decrease in expression of classical signatures (**Figure 7H**). In contrast with exogenous TGF-β (**Figure 7E**), microenvironmental IFNγ seemed to more specifically induce an IT state, as these cells did not fully transition to basal phenotypes at later timepoints (**Figure 7H**). These findings demonstrate that the microenvironment plays a critical role in specifying tumor transcriptional phenotypes and provide evidence for significant PDAC tumor cell plasticity in response to microenvironmental cues.

DISCUSSION

Here, by linking single-cell profiling of *in vivo* patient specimens to matched organoid models, we have built an essential comparative dataset to disentangle the contributions of cell-intrinsic versus -extrinsic factors to cancer cell transcriptional states in metastatic PDAC. We leveraged the precision afforded by scRNA-seq to identify a new PDAC cell state that co-expresses the basal and classical programs and behaves as a transitional intermediate between the basal and classical subtypes. Importantly, the identification of large fractions of co-expressing IT cells in human tumor biopsies using both mIF and scRNA-seq suggests interconversion between the classical and basal subtypes occurs frequently in response to various cues *in vivo* and implies that this intermediate state may be a hallmark of intratumoral plasticity and tumor cell transcriptional evolution. In fact, in contrast to prior reports (Chan-Seng-Yue et al., 2020), all tumors that had mixed but discrete populations of basal and classical cells also exhibited

473 proportional fractions of co-expressing IT cells. Our matched organoid studies provide strong evidence
474 that this extensive transcriptional heterogeneity is heavily influenced by the microenvironment, a finding
475 that is further reinforced by the identification of subtype-dependent TME structure. As such, this work
476 provides a detailed description of the PDAC metastatic niche, critical insight into the role of the
477 microenvironment in determining cancer cell phenotype in PDAC, and a general framework for
478 discovering and manipulating these relationships across cancer contexts.

479 Although mutations in *KRAS* play a critical role in pancreatic oncogenesis, PDAC cells have also
480 been shown to adopt more RAS-independent phenotypes as a mechanism of resistance to KRAS
481 suppression (Muzumdar et al., 2017). Our findings help to reconcile these opposing observations by
482 suggesting that KRAS target gene expression is more strongly associated with the IT cell state than either
483 basal or classical extremes. This finding suggests that while upregulation of KRAS signaling by
484 amplification or other mechanisms may play an important role in the transition toward the basal state
485 (Chan-Seng-Yue et al., 2020; Miyabayashi et al., 2020), it may become less functionally important once
486 this state transition is complete. Furthermore, the presence of IT cells enriched for *KRAS* and
487 inflammatory response gene expression is reminiscent of phenotypes seen in mouse models that suggest
488 inflamed progenitor-like cells as those that tolerate *KRAS* mutations and initiate tumorigenesis (Alonso-
489 Curbelo et al., 2021; Li et al., 2021).

490 Our single-cell data support the association between *KRAS* amplifications and the basal state *in*
491 *vivo*; however, when we compared our matched *KRAS* amplified biopsy and organoid cells, we saw that
492 this genotype did not lock cells into the basal state, and that microenvironmental conditions were a
493 dominant factor in determining tumor cell transcriptional subtype. Serial sampling of organoid models
494 across successive passages demonstrated both phenotypic drift and sub-clonal outgrowth, mirroring the
495 genetic evolution of PDXs and cell lines in culture (Ben-David et al., 2017; Ben-David et al., 2018), and
496 highlighting the complex interplay between genetics and microenvironmental influences on transcriptional
497 plasticity and clonal selection. This facile transition between subtypes has important implications for drug
498 treatment, and future studies using lineage tracing approaches are needed to better understand the
499 evolutionary dynamics in this system and how to track and exploit these processes therapeutically.
500 Additional studies into the epigenetic regulatory mechanisms underlying PDAC state transitions will also
501 be a critical next step in further delineating the relationships between genotype, microenvironment, and
502 phenotype.

503 Although we have identified co-expressing IT cells in both primary and metastatic tumors, the
504 transcriptional programs associated with co-expression may differ between these contexts. We
505 hypothesize that the basal state may be a common phenotypic endpoint for PDAC tumor cells in response
506 to microenvironmental stress, with superimposed transcriptional variation depending upon the specific

507 stressors a given tumor cell must overcome to reach this state. Supporting this concept is the observation
508 that cells exhibiting basal phenotypes show concomitant expression of EMT, IFN response, or hypoxia
509 response signatures, and these expression patterns may be driven by the specific microenvironment
510 (Benci et al., 2016; Connor et al., 2019). In addition, our finding that diverse microenvironmental signals,
511 including nutrient deprivation ("Minimal media"), autocrine and stromal signals (TGF-β), and immune
512 signals (IFNγ), induce the transition away from the classical subtype further supports this conclusion. We
513 postulate that IT intermediates likely house similar context-dependent complexity depending on the tissue
514 of residence.

515 Similar to malignant cells, the non-malignant cell types in the metastatic TME were varied in
516 phenotype and overall composition. Although we mainly sampled liver metastases, we identified strong
517 differences between mesenchymal populations from different biopsy sites. We observed that the liver
518 metastatic niche was enriched for pericyte-like myofibroblasts (Bartoschek et al., 2018; Di Carlo and
519 Peduto, 2018; Hosaka et al., 2016; Pelon et al., 2020), while other sites of metastasis and primary disease
520 were enriched for dermal fibroblast-like phenotypes. Given the pivotal role that has been suggested for
521 the fibrotic TME in primary disease (Ho et al., 2020; Sahai et al., 2020), these findings carry important
522 implications for targeting the stromal compartment in primary versus metastatic PDAC. For example,
523 inhibitors targeting FAP have recently shown preclinical efficacy (Fabre et al., 2020), but we observe FAP
524 expression favors dermal fibroblast-like cells but not pericyte-like myofibroblasts which are more
525 prevalent in liver metastases. As such, examination of these fibroblast phenotypes across larger sample
526 sets may help to identify additional clinically relevant variation in tumor-fibroblast crosstalk, and site-
527 specific combinatorial strategies may be needed to effectively target the PDAC tumor stroma.

528 We show how scRNA-seq can be employed to define the structure of the metastatic niche and
529 uncover formerly unappreciated relationships between tumor transcriptional phenotype and the local
530 TME. Although traditionally thought of as a uniformly "immune-cold" tumor, our findings highlight that the
531 immune microenvironment in metastatic PDAC harbors a layer of complexity closely linked to tumor cell
532 transcriptional subtype that may provide new avenues for therapeutic targeting. Notably, we observed
533 high levels of *IFNG* expression by CD8+ T cells and coordinated elevation in IFN response gene
534 expression in IT and basal malignant cells. We recapitulated this shift from a classical to a more IT state
535 in organoid models exposed to IFNγ, suggesting that malignant adaptation to signals from the TME may
536 contribute to driving IT and basal phenotypes. Similar to the relationship between inflammation and
537 tumorigenesis (Alonso-Curbelo et al., 2021; Li et al., 2021), we speculate that as tumors become inflamed
538 and immune-activated, malignant cells display enhanced plasticity, transition to an IT state in response,
539 and then progress to a fully basal phenotype with concomitant immune evasion and exclusion. These
540 relationships may have implications for PDAC response to immunotherapy given that a productive

541 immune response may promote more aggressive basal phenotypes (Benci et al., 2016; Li et al., 2018).
542 Notably, we observed evidence for basal expression signatures with a corresponding paucity of immune
543 cell type signatures in multiple other epithelial cancers, suggesting that coordination of malignant and
544 immune responses in basal contexts may be a broadly relevant phenomenon across many cancer types.
545 Additional studies with co-culture, mouse models, or serial samples from patients on active
546 immunotherapy may further clarify these coordinated and reciprocal tumor-immune interactions.

547 More generally, our approach using matched *in vivo* malignant populations as a reference for *ex*
548 *vivo* perturbations and model generation provides a critical framework for understanding the signals that
549 drive clinically relevant phenotypes but are missing from organoid and cell line cultures. The genetic
550 evolution of *ex vivo* models is a well-established phenomenon which carries functional consequences
551 (Ben-David et al., 2019; Ben-David et al., 2018). Our study highlights similar *ex vivo* evolution for
552 transcriptional variation, but also provides a strategy to rescue malignant phenotypes by re-introduction
553 of soluble signals needed for their support *in vivo*. This approach may offer a more tractable system for
554 state-specific high throughput screening compared with more complex heterotypic co-cultures or PDX
555 systems. With a catalogue of matched *in vivo* phenotypes as a reference, this workflow empowers not
556 only model fidelity, but enhances our ability to learn the phenotypic boundary conditions for individual
557 tumors. For example, we can begin to define whether certain pressures induce cell state transitions in
558 specific subsets of *ex vivo* models and identify which combinations of factors impede or synergistically
559 enhance these transitions. Furthermore, these studies highlight how model generation in different growth
560 contexts—organoids, cell lines, spheroids—may lead to the identification of emergent tumor cell
561 properties. Learning these rules across different tumor contexts and understanding which non-malignant
562 cell types participate *in vivo* would allow for the full appreciation of the symbiotic relationships within tumor
563 ecosystems and provide a valuable foundation for leveraging microenvironmental manipulation to control
564 tumor cell phenotype and behavior.

565 In sum, our data demonstrate coordinated phenotypic evolution driven by reciprocal interactions
566 between malignant cells and the TME in PDAC. Just as we consider therapeutic combinations to target
567 tumor cell intrinsic properties, paracrine interactions with the TME may equally drive tumor cell phenotype
568 and thus require consideration in designing combination strategies. We provide a framework for relating
569 malignant cells, the TME, and patient-derived model systems that may be applicable in other tumor types
570 with clinically relevant transcriptional variation across the malignant and microenvironmental
571 compartments.
572

ACKNOWLEDGEMENTS

We thank the study participants and their families for enabling this research. This work was funded by the Lustgarten Foundation Dedicated Laboratory Program (B.M.W., A.J.A.), Dana-Farber Cancer Institute Hale Center for Pancreatic Cancer Research (A.J.A., B.M.W., W.C.H.), the Doris Duke Charitable Foundation (A.J.A.), Pancreatic Cancer Action Network (A.J.A., B.M.W.), NIH-NCI K08 CA218420-02 (A.J.A.), P50 CA127003 (A.J.A., B.M.W.), U01 CA176058 (W.C.H.), U01 CA224146 (W.C.H., A.J.A.), U01 CA210171 (B.M.W.), U01 28020510 (W.C.H., A.K.S.), 1U2CCA23319501 (A.K.S.), U54 CA217377 (W.C.H., S.R.M., A.K.S.), U01 CA250549 (W.C.H., S.R., A.J.A.), Stand Up To Cancer (B.M.W.), Noble Effort Fund (B.M.W.), Wexler Family Fund (B.M.W.), Promises for Purple (B.M.W.), Hope Funds for Cancer Research Postdoctoral Fellowship (S.R.), Harvard Catalyst/The Harvard Clinical and Translational Science Center UL1 TR002541 (S.R.), Koch Institute for Integrative Cancer Research at MIT and the Dana-Farber/Harvard Cancer Center Bridge Project (W.C.H., S.R.M., S.R.), Dana-Farber Cancer Institute Gloria Spivak Faculty Advancement Fund (S.R.), Hopper-Belmont Foundation Inspiration Award (S.R.), Marcotte Center for Cancer Research (B.E.J.), Finnish Cultural Foundation (S.A.V.), Orion Research Foundation sr (S.A.V.), Broman Family Fund for Pancreatic Cancer Research (K.N.), Ludwig Center for Molecular Oncology at MIT (A.W.N.), Searle Scholars Program (A.K.S.), Beckman Young Investigator Program (A.K.S.), Sloan Fellowship in Chemistry (A.K.S.), and the Pew-Stewart Scholars Program for Cancer Research (A.K.S.). We also thank Bryan Bryson for helpful discussions of macrophage phenotypes.

AUTHOR CONTRIBUTIONS

S.R., P.S.W., B.M.W., W.C.H., A.J.A., and A.K.S. conceived and led the study. S.R., P.S.W., A.W.N., H.L.W., R.L.K., J.G.R., K.E.L., N.M., M.S.R., R.W.S.N., J.W., I.W., A.R., and E.S. designed and conducted experiments. S.R., P.S.W., A.W.N., H.L.W., A.D., A.A.B., K.S.K., A.M.J., L.F.S., Y.Y.L., A.D.C., and J.M.M. analyzed and interpreted data. S.A.V., A.D.C., E.R., D.R., L.K.B., A.R., A.M.J., T.E.C., K.P., D.A.R., K.N., J.M.C., and J.A.N. contributed patient samples, clinical data, and intellectual input. B.E.J., T.J., L.C., J.A.N., S.R.M., B.M.W., W.C.H., A.J.A., and A.K.S. supervised aspects of the project. S.R. and P.S.W. wrote the manuscript with input from A.W.N., H.L.W., S.R.M., B.M.W., W.C.H., A.J.A., and A.K.S. and review by all other co-authors.

DECLARATION OF INTERESTS

B.M.W. reports research support from Celgene, Eli Lilly and consulting for BioLineRx, Celgene, G1 Therapeutics, GRAIL. W.C.H. is a consultant for Thermo Fisher, Solasta Ventures, MPM Capital, Tyra Biosciences, iTeos, Frontier Medicines, KSQ Therapeutics, Jubilant Therapeutics, RAPPTA

Therapeutics, and Paraxel. A.K.S. reports compensation for consulting and/or SAB membership from Merck, Honeycomb Biotechnologies, Cellarity, Cogen Therapeutics, Orche Bio, and Dahlia Biosciences. A.J.A. has consulted for Oncorus, Inc., Arrakis Therapeutics, and Merck & Co., Inc, and has research funding from Mirati Therapeutics, Deerfield, Inc. and Novo Ventures that are unrelated to this project. S.R.M. is a founder of Travera. J.M.C. has received research funding from Merck, Tesaro, AstraZeneca, Bayer, and Esperas Pharma, has served as a consultant to Bristol Myers Squib, and has received travel funding from Bristol Myers Squib. A.R. is an employee of AstraZeneca and an equity holder in Celsius Therapeutics and NucleAI. Y.Y.L. reports equity from g.Root Biomedical Services. A.D.C. reports research support from Bayer. K.N. reports research support from Revolution Medicines, Evergrande Group, Genentech, Gilead Sciences, Celgene, Trovagene, Pharmavite, and Tarrex Biopharma, is a member of SABs for Bayer, Seattle Genetics, and Array Biopharma, and has consulted for X-Biotix Therapeutics.

Figure 1

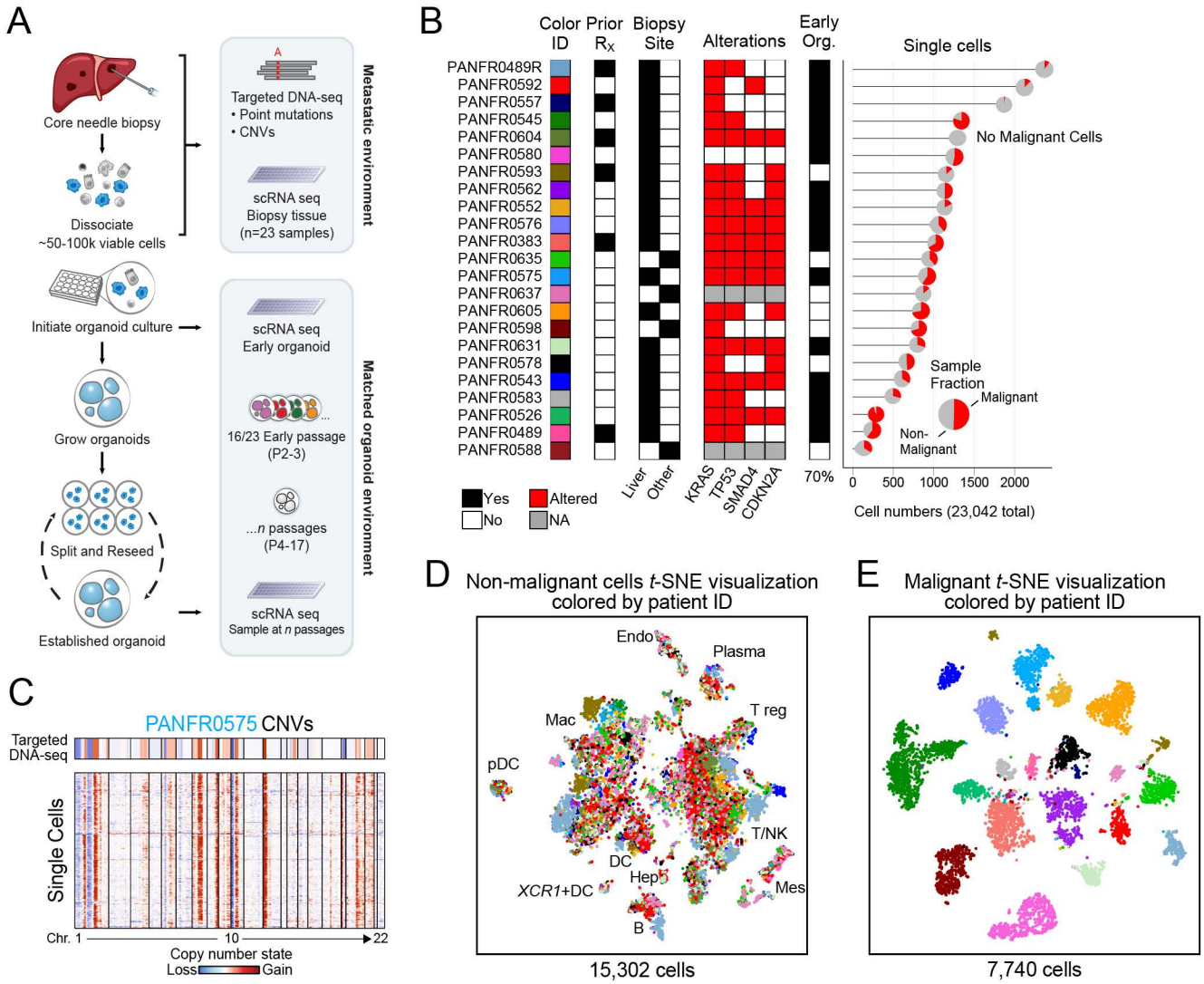
A
Core needle biopsy
Dissociate
~50-100k viable cells
Targeted DNA-seq
• Point mutations
• CNVs
scRNA seq
Biopsy tissue
(n=23 samples)
Metastatic environment
Initiate organoid culture
Grow organoids
Split and Reseed
Established organoid
scRNA seq
Early organoid
16/23 Early passage
(P2-3)
...n passages
(P4-17)
scRNA seq
Sample at n passages
Matched organoid environment
B
Color ID
Prior Rx
Biopsy Site
Alterations
Early Org.
Single cells
PANFR0489R
PANFR0592
PANFR0557
PANFR0545
PANFR0604
PANFR0580
PANFR0593
PANFR0562
PANFR0552
PANFR0576
PANFR0383
PANFR0635
PANFR0575
PANFR0637
PANFR0605
PANFR0598
PANFR0631
PANFR0578
PANFR0543
PANFR0583
PANFR0526
PANFR0489
PANFR0588
Liver
Other
KRAS
TP53
SMAD4
CDKN2A
70%
No Malignant Cells
Sample Fraction
Malignant
Non-Malignant
0
500
1000
1500
2000
Cell numbers (23,042 total)
Yes
No
Altered
NA
C
PANFR0575 CNVs
Targeted DNA-seq
Single Cells
Chr. 1
10
22
Copy number state
Loss
Gain
D
Non-malignant cells t-SNE visualization colored by patient ID
Endo
Plasma
T reg
Mac
pDC
T/NK
DC
Hep
XCR1+DC
Mes
B
15,302 cells
E
Malignant t-SNE visualization colored by patient ID
7,740 cells

619 **Figure 1. A clinical pipeline for matched single-cell RNA-seq and organoid generation from**
620 **metastatic PDAC biopsies.**
621 **(A)** Pipeline for collecting patient samples, and dissociation and allocation for scRNA-seq and parallel
622 organoid development.
623 **(B)** Clinical and molecular features for all patients included in the dataset (R_x = Therapy; Other = Adrenal
624 (PANFR0637), Omentum (PANFR0635, PANFR0598), Peritoneum (PANFR0588); Org. at P2 =
625 Organoid measured at passage 2). Mutations were determined by bulk targeted DNA-seq (Red, Altered;
626 White, wildtype; Grey, Data not available). Number of single cells captured per biopsy and their malignant
627 and non-malignant fraction is visualized at the right.
628 **(C)** Example bulk targeted DNA-seq (top) and single-cell inferred CNV profiles (rows, bottom) arranged
629 by chromosome (columns) from PANFR0575.
630 **(D-E)** *t*-distributed stochastic neighbor embedding (*t*-SNE) visualization for non-malignant (**D**) and
631 malignant (**E**) single cells in the biopsy cohort. Cells are colored by patient as in **B**. Endo, Endothelial;
632 Mes, Mesenchymal; B, B-cell; Hep, Hepatocyte; DC, Dendritic cell; pDC, Plasmacytoid dendritic cell;
633 Mac, Macrophage; T, T-cell; NK, Natural killer cell.
634
635 *See also Supplemental Figures S1 & S2; Supplemental Tables S1 & S2.*

Figure 2

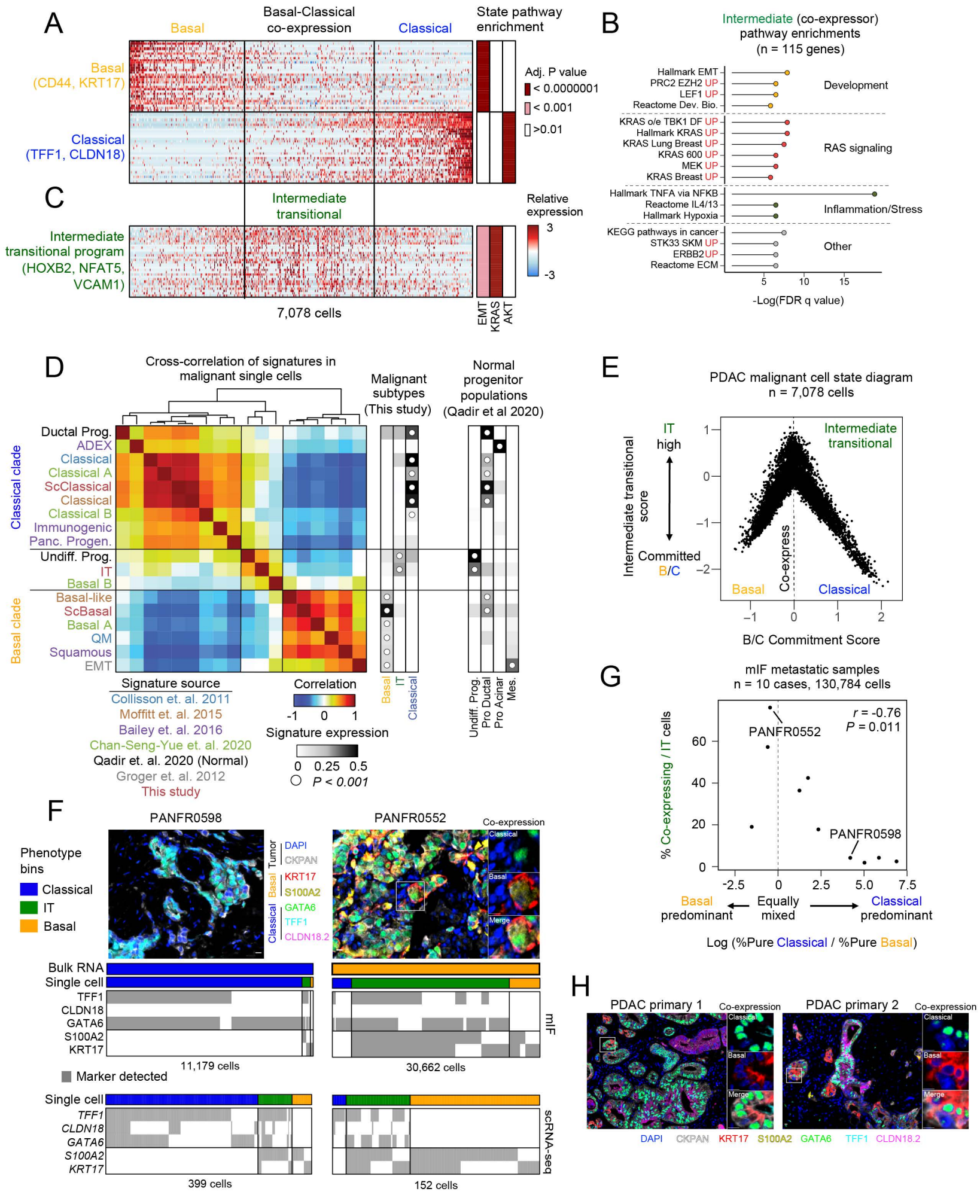
A
Basal
Basal-Classical co-expression
Classical
State pathway enrichment
Basal (CD44, KRT17)
Classical (TFF1, CLDN18)
Adj. P value
< 0.0000001
< 0.001
>0.01
C
Intermediate transitional
Intermediate transitional program (HOXB2, NFAT5, VCAM1)
Relative expression
3
-3
7,078 cells
EMT
KRAS
AKT
B
Intermediate (co-expressor) pathway enrichments (n = 115 genes)
Hallmark EMT
PRC2 EZH2 UP
LEF1 UP
Reactome Dev. Bio.
Development
KRAS o/e TBK1 DF UP
Hallmark KRAS UP
KRAS Lung Breast UP
KRAS 600 UP
MEK UP
KRAS Breast UP
RAS signaling
Hallmark TNFA via NFKB
Reactome IL4/13
Hallmark Hypoxia
Inflammation/Stress
KEGG pathways in cancer
STK33 SKM UP
ERBB2 UP
Reactome ECM
Other
5
10
15
-Log(FDR q value)
D
Cross-correlation of signatures in malignant single cells
Malignant subtypes (This study)
Normal progenitor populations (Qadir et al 2020)
Ductal Prog.
ADEX
Classical
Classical A
ScClassical
Classical
Classical B
Immunogenic
Panc. Progen.
Undiff. Prog.
IT
Basal B
Basal-like
ScBasal
Basal A
QM
Squamous
EMT
Classical clade
Basal clade
Basal
IT
Classical
Undiff. Prog.
Pro Ductal
Pro Acinar
Mes.
Signature source
Collisson et. al. 2011
Moffitt et. al. 2015
Bailey et. al. 2016
Chan-Seng-Yue et. al. 2020
Qadir et. al. 2020 (Normal)
Groger et. al. 2012
This study
Correlation
-1
0
1
Signature expression
0
0.25
0.5
P < 0.001
E
PDAC malignant cell state diagram
n = 7,078 cells
IT high
Intermediate transitional score
Committed B/C
Intermediate transitional
Co-express
Basal
Classical
1
0
−1
−2
−1
0
1
2
B/C Commitment Score
G
mIF metastatic samples
n = 10 cases, 130,784 cells
r = -0.76
P = 0.011
PANFR0552
PANFR0598
% Co-expressing / IT cells
60
40
20
0
-2.5
0
2.5
5.0
7.5
Basal predominant
Equally mixed
Classical predominant
Log (%Pure Classical / %Pure Basal)
F
PANFR0598
PANFR0552
Co-expression
Phenotype bins
Classical
IT
Basal
Tumor
DAPI
CKPAN
Basal
KRT17
S100A2
Classical
GATA6
TFF1
CLDN18.2
Classical
Basal
Merge
Bulk RNA
Single cell
TFF1
CLDN18
GATA6
S100A2
KRT17
mIF
11,179 cells
30,662 cells
Marker detected
Single cell
TFF1
CLDN18
GATA6
S100A2
KRT17
scRNA-seq
399 cells
152 cells
H
PDAC primary 1
PDAC primary 2
Co-expression
Classical
Basal
Merge
DAPI
CKPAN
KRT17
S100A2
GATA6
TFF1
CLDN18.2

636 **Figure 2. An intermediate transitional state bridges basal and classical phenotypes.**
637 **(A)** Heatmaps depict the expression of basal and classical expression programs and highlight the co-
638 expressing intermediates (n=30 genes each).
639 **(B)** Gene set enrichment analysis for the 115 genes specific to the co-expressing intermediate state.
640 **(C)** The intermediate transitional ("IT") expression program (n = 30 genes) is enriched by co-expressing
641 cells. Enrichment adjusted *P*-values (hypergeometric test) for EMT, *KRAS*, and *AKT* gene sets are
642 indicated at right for each gene expression program in **A** and **C**.
643 **(D)** Cross-correlation between new and previously proposed expression signatures (rows and columns;
644 text color = source, below) in our PDAC single-cells. Average expression for each signature (rows) is
645 shown at the right for cells in the malignant subtypes from our cohort and the normal pancreatic progenitor
646 cells from Qadir et al., 2020. White dot indicates the subset with the highest average significant
647 expression for each signature (Kruskal-Wallis test); no white dot indicates no significant expression.
648 **(E)** Malignant cell state diagram for PDAC. Basal-classical commitment score (x axis) and IT score (y
649 axis) for all 7,078 malignant cells (**Methods**).
650 **(F)** Multiplex immunofluorescence analysis (mIF) identifies co-expressing IT cells in matched metastatic
651 samples. Top are representative images from two cases (white box indicates region for co-expression
652 insets at right), and bottom indicates marker detection patterns for mIF and matched scRNA-seq data
653 (**Methods**). Scale bar represents 10 μm.
654 **(G)** Frequency of co-expressing IT cells is correlated with balanced representation of pure basal and
655 classical phenotypes by mIF within individual samples. Log ratio of % basal and classical cells in each
656 sample (x axis) versus their % co-expressing / IT cells (y axis).
657 **(H)** Co-expressing IT cells are also identified in primary PDAC samples by mIF. Scale bar represents 10
658 μm.
659
660 *See also Supplemental Figures S2, S3 & S4; Supplemental Tables S3 & S4.*

Figure 3

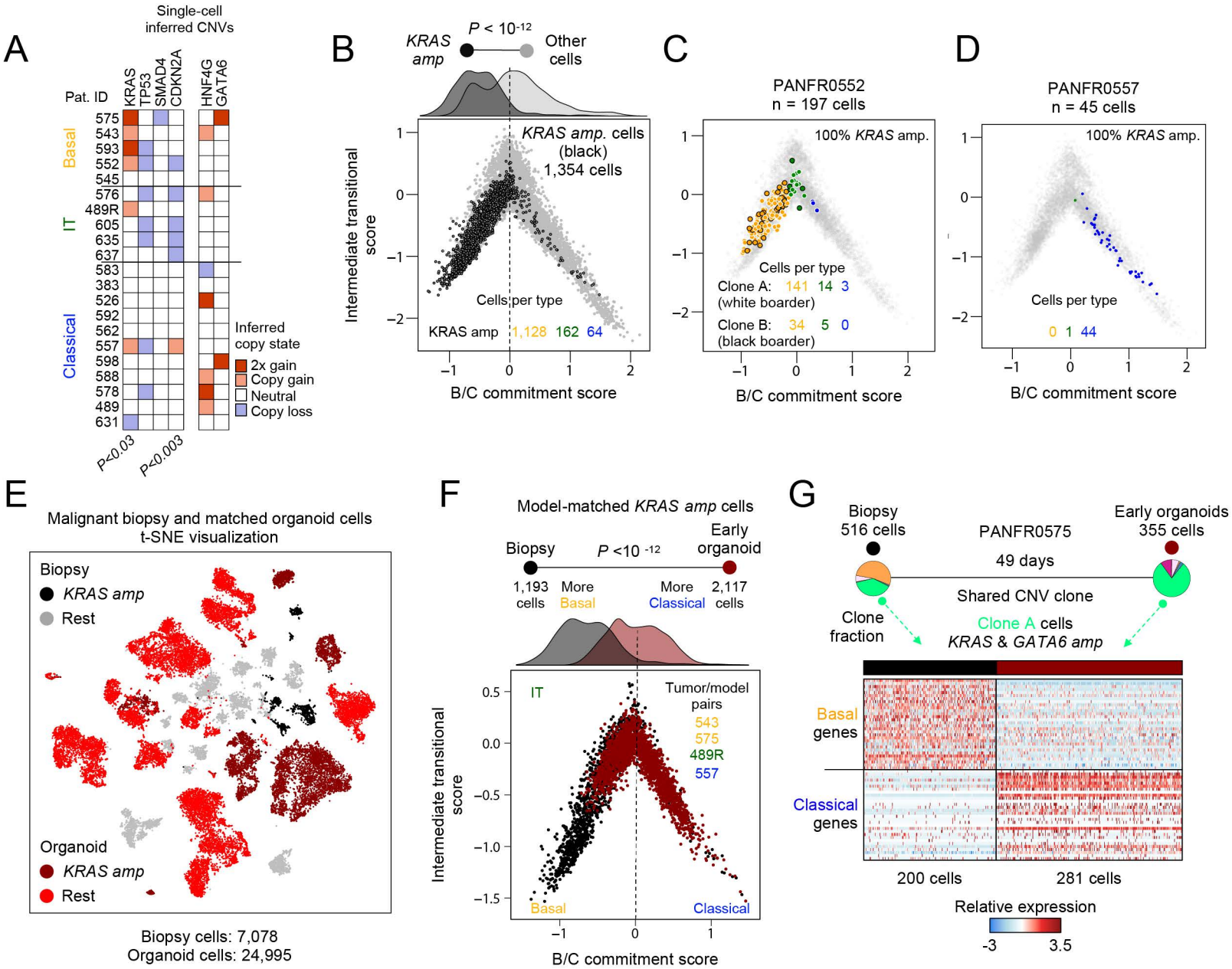
A
Single-cell inferred CNVs
Pat. ID
KRAS
TP53
SMAD4
CDKN2A
HNF4G
GATA6
Basal
IT
Classical
575
543
593
552
545
576
489R
605
635
637
583
383
526
592
562
557
598
588
578
489
631
P<0.03
P<0.003
Inferred copy state
2x gain
Copy gain
Neutral
Copy loss
B
KRAS amp
P < 10-12
Other cells
KRAS amp. cells (black) 1,354 cells
Cells per type
KRAS amp 1,128 162 64
Intermediate transitional score
B/C commitment score
C
PANFR0552
n = 197 cells
100% KRAS amp.
Cells per type
Clone A: 141 14 3
(white boarder)
Clone B: 34 5 0
(black boarder)
B/C commitment score
D
PANFR0557
n = 45 cells
100% KRAS amp.
Cells per type
0 1 44
B/C commitment score
E
Malignant biopsy and matched organoid cells
t-SNE visualization
Biopsy
KRAS amp
Rest
Organoid
KRAS amp
Rest
Biopsy cells: 7,078
Organoid cells: 24,995
F
Model-matched KRAS amp cells
Biopsy
P <10 -12
Early organoid
1,193 cells
More Basal
More Classical
2,117 cells
IT
Tumor/model pairs
543
575
489R
557
Basal
Classical
Intermediate transitional score
B/C commitment score
G
Biopsy
516 cells
PANFR0575
49 days
Early organoids
355 cells
Shared CNV clone
Clone fraction
Clone A cells
KRAS & GATA6 amp
Basal genes
Classical genes
200 cells
281 cells
Relative expression
-3
3.5

661 **Figure 3. Microenvironment dictates phenotype in *KRAS*-amplified tumor cells.**
662 **(A)** Single-cell inferred copy number alterations for each sample in the biopsy cohort (**Methods**). Tumors
663 are grouped by expression of their dominant subtype based on the clustering in **Supp. Fig. S3G**, *P*-
664 values comparing presence of each alteration among the groups (Basal, Classical, IT) are determined
665 by Fisher's exact test.
666 **(B)** Malignant cell state diagram as in **Figure 2E** but highlighting all *in vivo KRAS*-amplified tumor cells
667 (black border) across the states.
668 **(C)** Similar to **B**, but highlighting PANFR0552 *KRAS*-amplified malignant cell heterogeneity. White and
669 black borders correspond to separate CNV sub-clones (both *KRAS* amplified) and color fill denotes
670 transcriptional subtype.
671 **(D)** Similar to **B**, but highlighting PANFR0557 *KRAS*-amplified malignant cell heterogeneity. Color fill
672 denotes transcriptional subtype.
673 **(E)** *t*-SNE visualization of all biopsy (grey and black) and matched organoid cells (red and dark red) from
674 iterative passages. *KRAS*-amplified tumor cells from *in vivo* specimens (black) and organoid models (dark
675 red) are highlighted with distinct colors.
676 **(F)** Cell state diagram for all cells with inferred *KRAS* amplifications in biopsy (grey) and organoid (red)
677 microenvironments. *P*-value compares biopsy versus early passage organoid score distributions (top
678 density) and was determined by student's T test.
679 **(G)** Clonal fractions (pie charts) from the *KRAS*-amplified PANFR0575 sample in biopsy and organoid
680 conditions. Heatmap shows the relative expression in single cells from plastic clone A (bright green) in
681 both conditions.

Figure 4

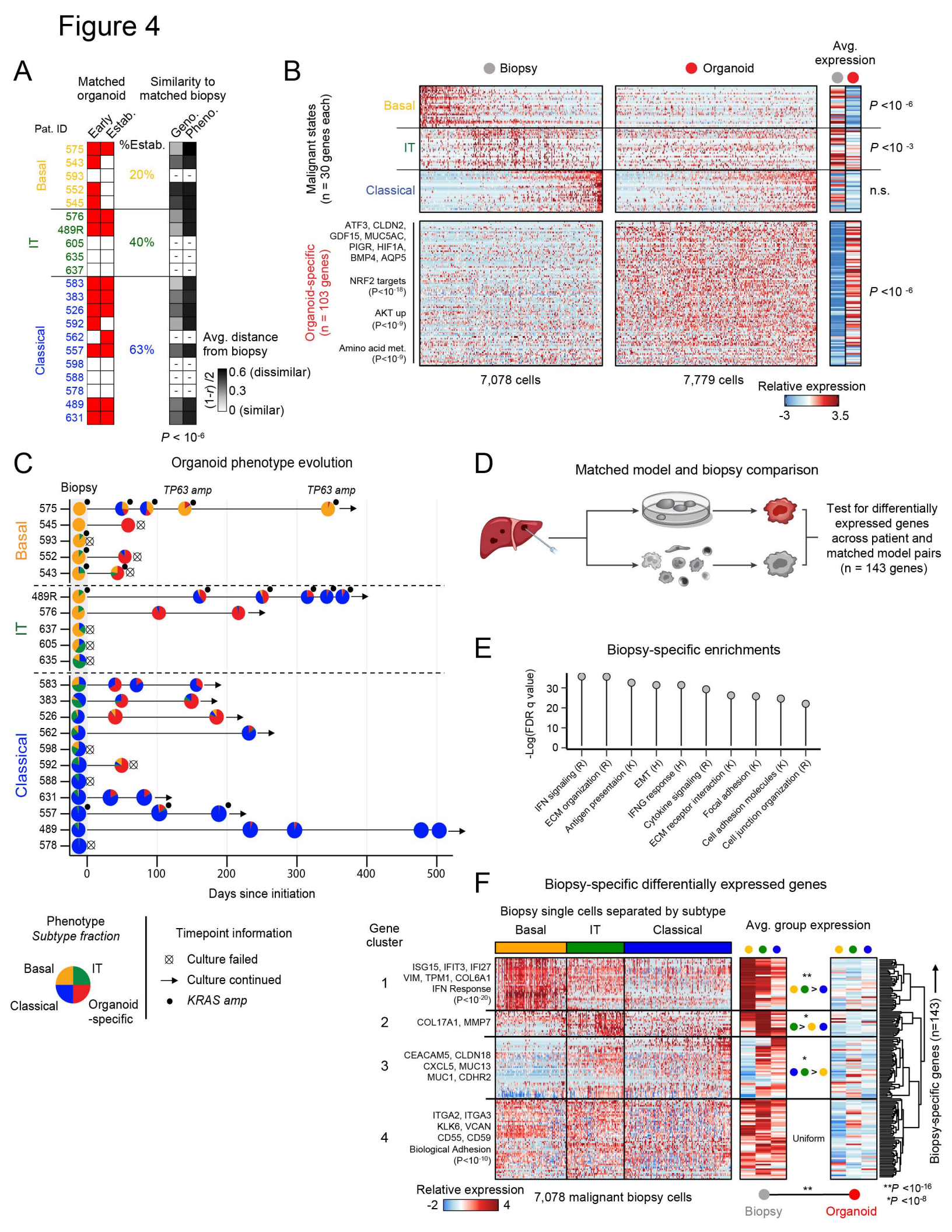
A
Matched organoid
Similarity to matched biopsy
Pat. ID
Early Estab.
Geno. Pheno.
%Estab.
Basal
IT
Classical
575
543
593
552
545
576
489R
605
635
637
583
383
526
592
562
557
598
588
578
489
631
20%
40%
63%
Avg. distance from biopsy
(1-r) /2
0.6 (dissimilar)
0.3
0 (similar)
P < 10-6
B
Biopsy
Organoid
Avg. expression
Malignant states (n = 30 genes each)
Basal
IT
Classical
P <10 -6
P <10 -3
n.s.
Organoid-specific (n = 103 genes)
ATF3, CLDN2, GDF15, MUC5AC, PIGR, HIF1A, BMP4, AQP5
NRF2 targets (P<10-18)
AKT up (P<10-9)
Amino acid met. (P<10-9)
P <10 -6
7,078 cells
7,779 cells
Relative expression
-3
3.5
C
Organoid phenotype evolution
Biopsy
TP63 amp
TP63 amp
Basal
IT
Classical
Days since initiation
0
100
200
300
400
500
Phenotype
Subtype fraction
Basal
IT
Classical
Organoid -specific
Timepoint information
Culture failed
Culture continued
KRAS amp
D
Matched model and biopsy comparison
Test for differentially expressed genes across patient and matched model pairs (n = 143 genes)
E
Biopsy-specific enrichments
-Log(FDR q value)
30
20
10
0
IFN signaling (R)
ECM organization (R)
Antigen presentaion (K)
EMT (H)
IFNG response (H)
Cytokine signaling (R)
ECM receptor interaction (K)
Focal adhesion (K)
Cell adhesion molecules (K)
Cell junction organization (R)
F
Biopsy-specific differentially expressed genes
Biopsy single cells separated by subtype
Basal
IT
Classical
Avg. group expression
Gene cluster
1
ISG15, IFIT3, IFI27
VIM, TPM1, COL6A1
IFN Response
(P<10-20)
2
COL17A1, MMP7
3
CEACAM5, CLDN18
CXCL5, MUC13
MUC1, CDHR2
4
ITGA2, ITGA3
KLK6, VCAN
CD55, CD59
Biological Adhesion
(P<10-10)
Uniform
Biopsy-specific genes (n=143)
Relative expression
-2
4
7,078 malignant biopsy cells
Biopsy
Organoid
**P <10-16
*P <10-8

682 **Figure 4. Organoid culture microenvironment selects against the basal state with phenotypic**
683 **evolution over time.**
684 **(A)** Sampling from each model initiated as an organoid. Red fill represents measurements at an Early
685 time point and if that biopsy established a long-term culture (Estab.). Right grey scale heat indicates the
686 distance (**Methods**) between each biopsy-early organoid pair for CNVs (Geno.) or transcriptional subtype
687 (Pheno.). *P*-value for Geno. vs Pheno. differences determined by student's T test.
688 **(B)** Relative expression for the malignant programs (top) and organoid-specific genes (bottom) in biopsy
689 cells (left) and their matched, early passage organoid cells (n=13 models; right). Parenthetical *P*-values
690 (left) indicate hypergeometric test for enrichment of pathways in the indicated gene clusters. Far right
691 heat is average expression for all genes in each group, *P*-values determined by student's T test.
692 **(C)** Swimmer's plot shows the evolution of organoid phenotype in the culture microenvironment. Each
693 point indicates a passage when organoids were sampled with scRNA-seq, and pie chart fill indicates the
694 fraction of single cells binned as each transcriptional subtype.
695 **(D)** Schematic for matched tumor-organoid differential expression analysis.
696 **(E)** Top differentially expressed genes *in vivo* (143 genes) are TME-associated and enrich for TME-
697 associated pathways. All top enrichments shown are highly significant (*P*-value < 10^{-12}).
698 **(F)** Hierarchical clustering in biopsy cells (columns) of the relative expression for the 143 TME-associated
699 genes preferentially expressed *in vivo* (rows). Cells are binned in the single-cell heatmap and the
700 averages at right by their originating tumor's average transcriptional subtype. Gene-level averages are
701 split by biopsy (left) and organoid cells (right). Parenthetical *P*-values (left) indicate hypergeometric test
702 for enrichment of pathways in the indicated gene clusters. For within-group differences in expression for
703 biopsy averages, *P*-values are computed by one-way ANOVA followed by Tukey's HSD and compare
704 averaged expression of each gene cluster between cells from different biopsy subsets (middle heatmap;
705 **P*-value < 10^{-8}; ***P*-value < 10^{-16}). Overall biopsy versus organoid average expression difference for all
706 143 genes is determined by Student's T test.
707
708 *See also Supplemental Figure S5; Supplemental Table S5.*
709
710

Figure 5

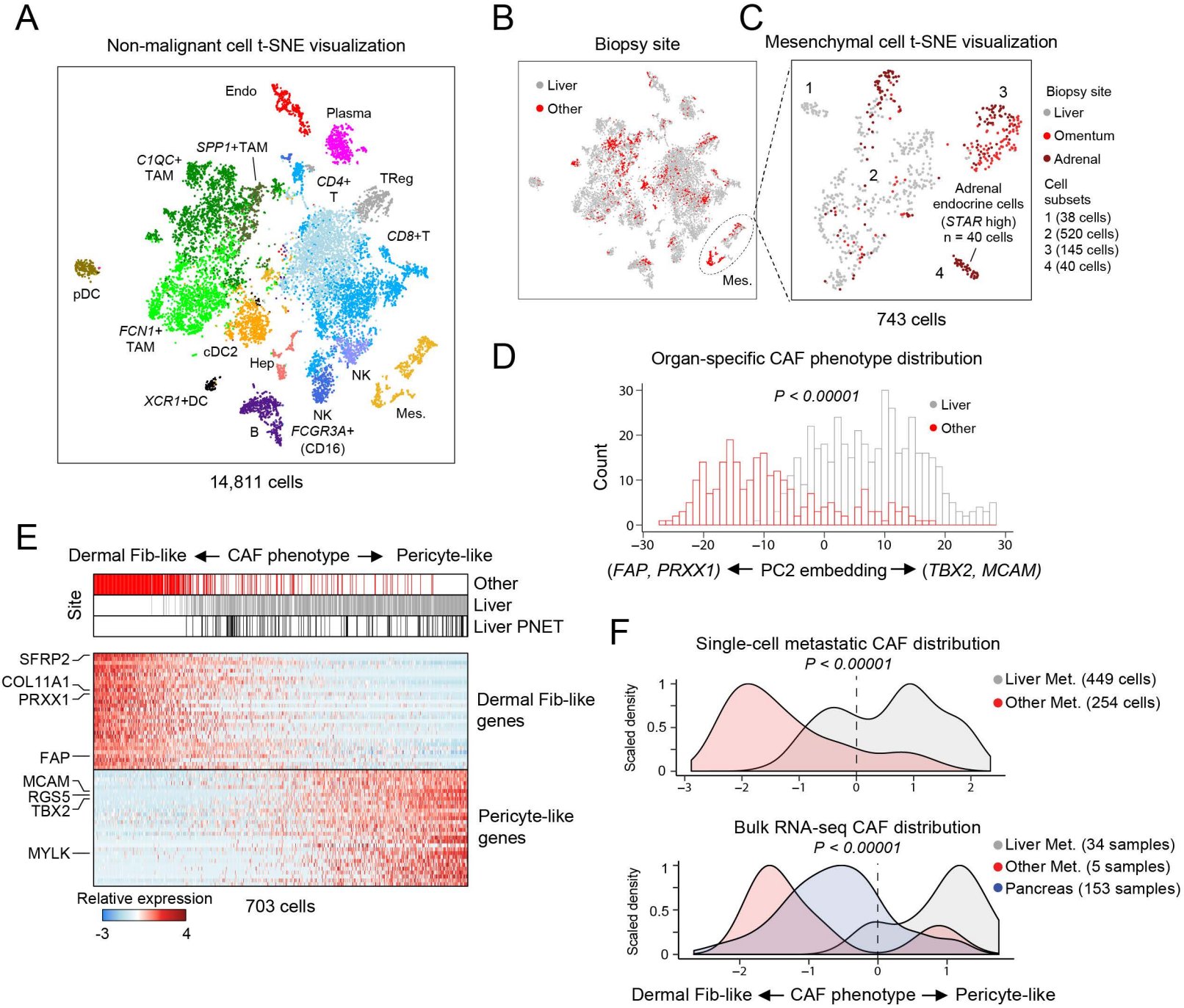
A
Non-malignant cell t-SNE visualization
Endo
Plasma
SPP1+TAM
C1QC+ TAM
CD4+ T
TReg
CD8+T
pDC
FCN1+ TAM
cDC2
Hep
NK
XCR1+DC
NK
Mes.
B
FCGR3A+ (CD16)
14,811 cells
B
Biopsy site
Liver
Other
Mes.
C
Mesenchymal cell t-SNE visualization
1
2
3
4
Adrenal endocrine cells (STAR high) n = 40 cells
743 cells
Biopsy site
Liver
Omentum
Adrenal
Cell subsets
1 (38 cells)
2 (520 cells)
3 (145 cells)
4 (40 cells)
D
Organ-specific CAF phenotype distribution
P < 0.00001
Liver
Other
Count
(FAP, PRXX1) ← PC2 embedding → (TBX2, MCAM)
E
Dermal Fib-like ← CAF phenotype → Pericyte-like
Site
Other
Liver
Liver PNET
SFRP2
COL11A1
PRXX1
FAP
MCAM
RGS5
TBX2
MYLK
Dermal Fib-like genes
Pericyte-like genes
Relative expression
-3
4
703 cells
F
Single-cell metastatic CAF distribution
P < 0.00001
Liver Met. (449 cells)
Other Met. (254 cells)
Scaled density
Bulk RNA-seq CAF distribution
P < 0.00001
Liver Met. (34 samples)
Other Met. (5 samples)
Pancreas (153 samples)
Scaled density
Dermal Fib-like ← CAF phenotype → Pericyte-like

711 **Figure 5. Immune heterogeneity and distinct fibroblast phenotypes exist in the liver metastatic**
712 **microenvironment.**
713 **(A)** *t*-SNE visualization of non-malignant cells identified in the metastatic microenvironment,
714 abbreviations are the same as in **Figure 1D** (TAM, tumor associated macrophage; NK, natural killer).
715 **(B)** Same visualization as in **A**, but cells are colored by sampling site (Liver, grey; Other, red). Only the
716 mesenchymal cells (dotted circle, Mes.) have appreciable separation by anatomical site.
717 **(C)** *t*-SNE visualization of sub-clustering (SNN) performed on mesenchymal cells colored by their
718 anatomical site. Cell subsets (1-4) determined by SNN clustering.
719 **(D)** Frequency of CAFs (y axis, cell count) across PC2 scores, colored by site of biopsy tissue. *P*-value
720 determined by student's T test.
721 **(E)** Heatmap for relative expression of the Dermal Fibroblast-like (PC2 low) and Pericyte-like (PC2 high)
722 programs. Anatomical site is shown for each cell (top).
723 **(F)** Density plots for CAF phenotype score in single cells from our metastatic cohort (top) or previously
724 published PDAC bulk RNA-seq profiles (bottom) (Aguirre et al., 2018; Cancer Genome Atlas Research
725 Network, 2017), fill indicates anatomical site. *P*-value determined by student's T test (top) or by ANOVA
726 followed by Tukey's HSD (bottom).
727
728 *See also Supplemental Figure S6; Supplemental Table S2.*

Figure 6

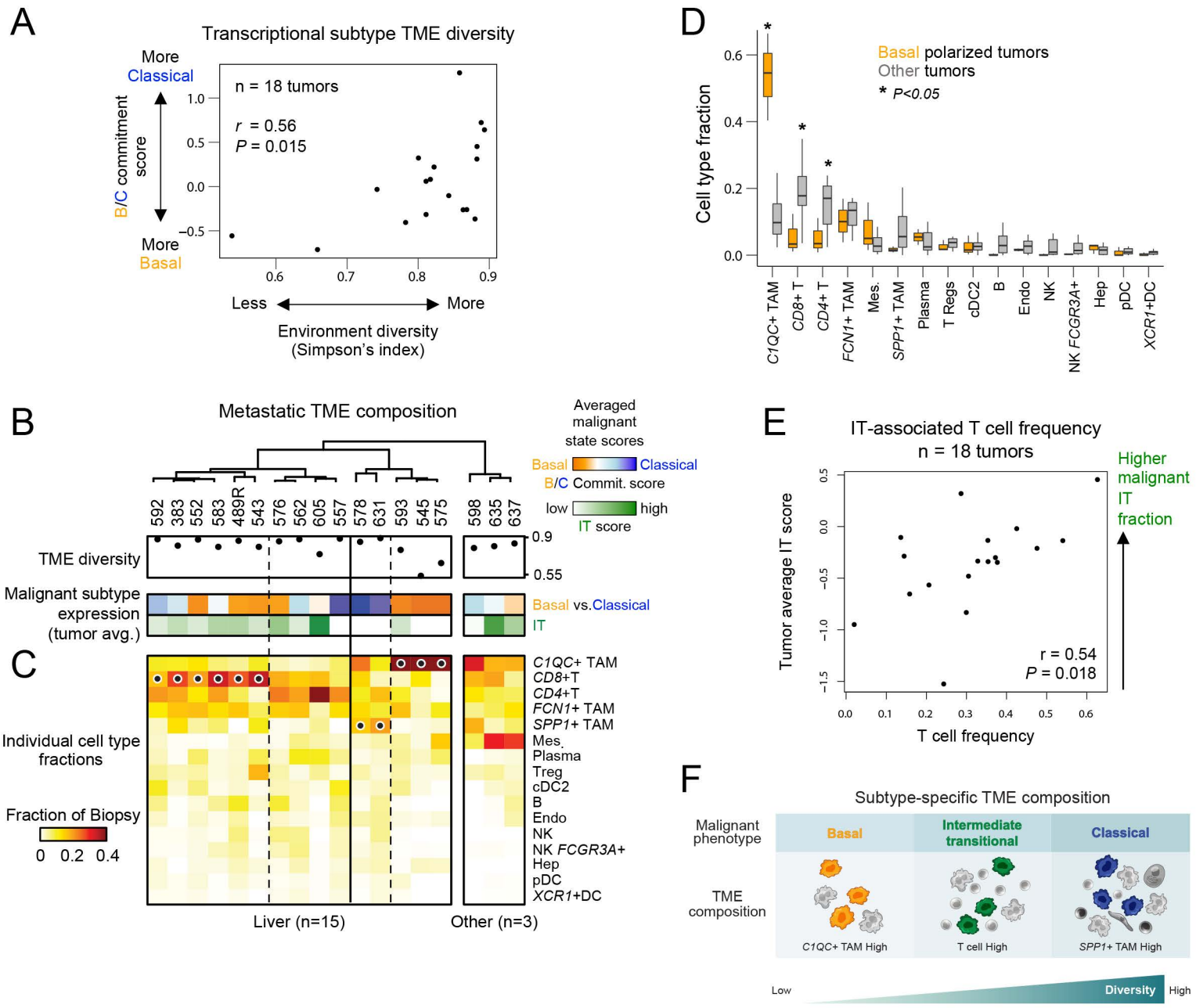
A
Transcriptional subtype TME diversity
More Classical
B/C commitment score
More Basal
n = 18 tumors
r = 0.56
P = 0.015
Less
More
Environment diversity (Simpson's index)
B
Metastatic TME composition
Averaged malignant state scores
Basal
Classical
B/C Commit. score
low
high
IT score
592 383 552 583 489R 543 576 562 605 557 578 631 593 545 575 598 635 637
TME diversity
Malignant subtype expression (tumor avg.)
Basal vs.Classical
IT
C
Individual cell type fractions
Fraction of Biopsy
0 0.2 0.4
C1QC+ TAM
CD8+T
CD4+T
FCN1+ TAM
SPP1+ TAM
Mes.
Plasma
Treg
cDC2
B
Endo
NK
NK FCGR3A+
Hep
pDC
XCR1+DC
Liver (n=15)
Other (n=3)
D
Basal polarized tumors
Other tumors
* P<0.05
Cell type fraction
C1QC+ TAM
CD8+ T
CD4+ T
FCN1+ TAM
Mes.
SPP1+ TAM
Plasma
T Regs
cDC2
B
Endo
NK
NK FCGR3A+
Hep
pDC
XCR1+DC
E
IT-associated T cell frequency
n = 18 tumors
Higher malignant IT fraction
Tumor average IT score
r = 0.54
P = 0.018
T cell frequency
F
Subtype-specific TME composition
Malignant phenotype
TME composition
Basal
Intermediate transitional
Classical
C1QC+ TAM High
T cell High
SPP1+ TAM High
Low
Diversity
High

729 **Figure 6. Transcriptional subtypes associate with distinct metastatic microenvironments.**
730 **(A)** Correlation between microenvironment diversity (Simpson's Index, x axis) and the average malignant
731 basal-classical commitment score for each biopsy (y axis).
732 **(B)** Dot plot indicates the Simpson's Index calculated for each biopsy and heat bars indicate each tumor's
733 average malignant cell expression for each of the malignant transcriptional programs.
734 **(C)** Fraction of each non-malignant cell type (heat, rows) in each biopsy sample (columns). Dots indicate
735 top statistically significant cell type frequency differences calculated using Kruskal-Wallis test with
736 multiple hypothesis correction. Samples are ordered as in **B.**
737 **(D)** Box plots compare cell type fraction between the basal polarized tumors with low diversity
738 (PANFR0593, 575, 545) and all others. *P*-value determined by student's T test.
739 **(E)** Correlation between T cell fraction and IT malignant score.
740 (**F**) Schematic summarizing associations between microenvironmental diversity, non-malignant
741 infiltrates, and tumor subtype.
742
743 *See also Supplemental Figure S6; Supplemental Table S2.*

Figure 7

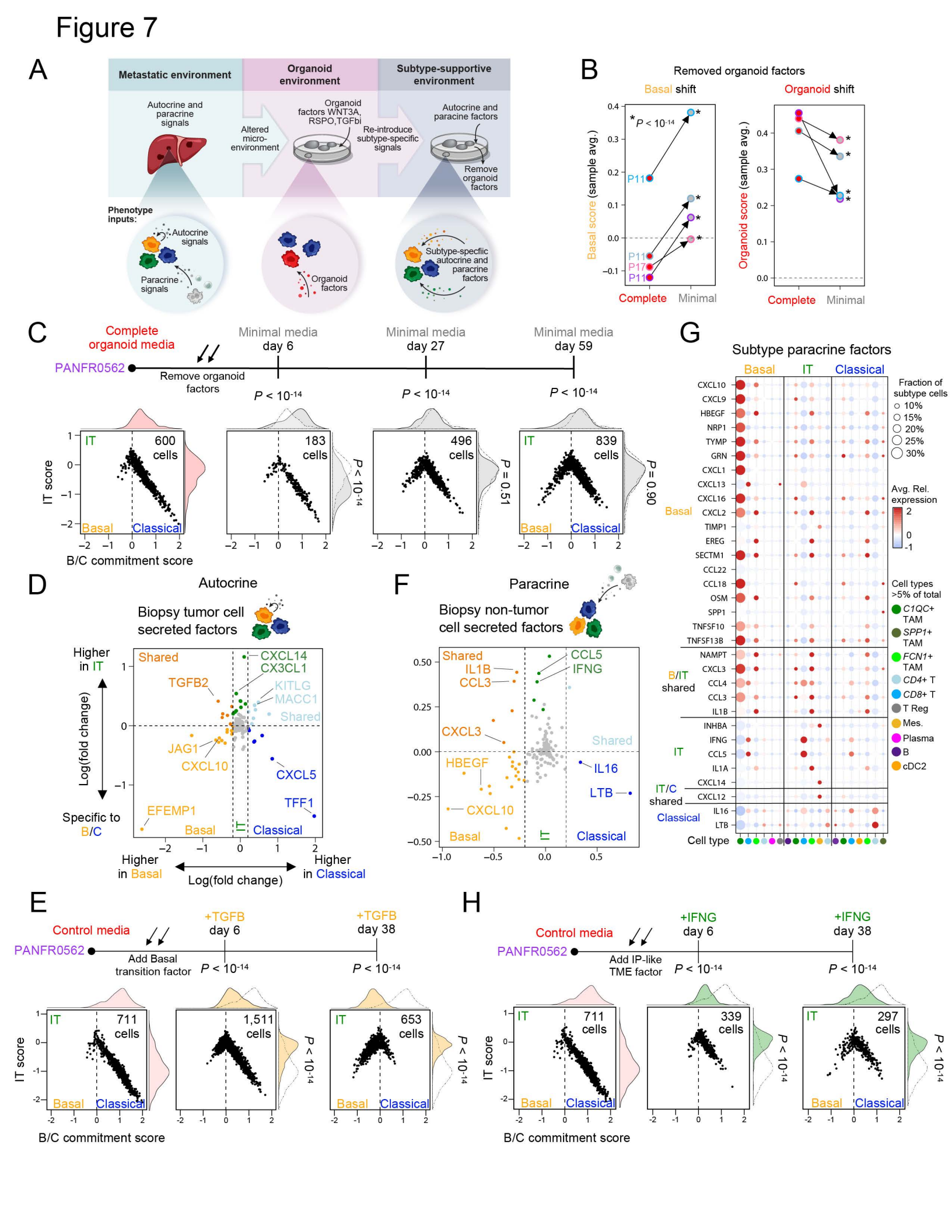
A
Metastatic environment
Organoid environment
Subtype-supportive environment
Autocrine and paracrine signals
Altered micro-environment
Organoid factors WNT3A, RSPO,TGFbi
Re-introduce subtype-specific signals
Autocrine and paracine factors
Remove organoid factors
Phenotype inputs:
Autocrine signals
Paracrine signals
Organoid factors
Subtype-specfic autocrine and paracrine factors
B
Removed organoid factors
Basal shift
Organoid shift
Basal score (sample avg.)
Organoid score (sample avg.)
P < 10-14
P11
P17
Complete
Minimal
C
Complete organoid media
PANFR0562
Remove organoid factors
Minimal media day 6
Minimal media day 27
Minimal media day 59
P < 10-14
P = 0.51
P = 0.90
IT score
IT
600 cells
183 cells
496 cells
839 cells
Basal
Classical
B/C commitment score
D
Autocrine
Biopsy tumor cell secreted factors
Higher in IT
Specific to B/C
Log(fold change)
Shared
CXCL14
CX3CL1
TGFB2
KITLG
MACC1
JAG1
CXCL10
CXCL5
TFF1
EFEMP1
Higher in Basal
Higher in Classical
F
Paracrine
Biopsy non-tumor cell secreted factors
CCL5
IFNG
IL1B
CCL3
CXCL3
HBEGF
IL16
LTB
G
Subtype paracrine factors
Basal
IT
Classical
Fraction of subtype cells
10%
15%
20%
25%
30%
Avg. Rel. expression
Cell types >5% of total
C1QC+ TAM
SPP1+ TAM
FCN1+ TAM
CD4+ T
CD8+ T
T Reg
Mes.
Plasma
B
cDC2
CXCL10
CXCL9
HBEGF
NRP1
TYMP
GRN
CXCL1
CXCL13
CXCL16
CXCL2
TIMP1
EREG
SECTM1
CCL22
CCL18
OSM
SPP1
TNFSF10
TNFSF13B
NAMPT
CXCL3
CCL4
CCL3
IL1B
INHBA
IFNG
CCL5
IL1A
CXCL14
CXCL12
IL16
LTB
B/IT shared
IT/C shared
Cell type
E
Control media
PANFR0562
Add Basal transition factor
+TGFB day 6
+TGFB day 38
711 cells
1,511 cells
653 cells
H
Control media
PANFR0562
Add IP-like TME factor
+IFNG day 6
+IFNG day 38
711 cells
339 cells
297 cells

744 **Figure 7. Tumor subtype-specific secreted microenvironmental factors rescue malignant**
745 **transcriptional heterogeneity.**
746 **(A)** Schematic describing microenvironmental inputs *in vivo* ("Metastatic environment"*)* versus *ex vivo*
747 ("Organoid environment") to tumor phenotype. Right panel ("Subtype-supportive environment") describes
748 an overall strategy to recover malignant transcriptional heterogeneity by removing organoid factors (**B,**
749 **C**) and adding state-specific autocrine (**D, E**) or paracrine (**F-H**) factors.
750 **(B)** Tied dot plot represents the sample average basal score (left) and organoid-specific score (right) in
751 the indicated conditions. Lines tie samples and color outlines indicate sample identity as in **Figure 1B**.
752 *P*-value compares respective single cell distributions within models and was calculated by student's T
753 test.
754 **(C)** Cell state diagrams for organoid cells cultured in complete medium or at 3 time points in minimal
755 media. *P*-values for group differences between B/C commitment (top) and IT scores (right) were
756 calculated by ANOVA followed by Tukey's HSD. *P*-values displayed are for that timepoint vs. the
757 complete media condition.
758 **(D)** Differential expression (Wilcoxon rank sum test) for known secreted factors by *in vivo* tumor cells
759 (autocrine) between basal and classical (x axis) and IT malignant cells and the rest (y axis). Subtype-
760 specific genes that pass significance after multiple hypothesis correction ($P < 0.05$) are colored by their
761 group association.
762 **(E)** Cell state diagrams with marginal density plots for organoid cells cultured in control medium (OWRNA,
763 reduced organoid medium) or at 2 time points in control media with TGF-β. *P*-values for group differences
764 between B/C commitment (top) and IT scores (right) were calculated by ANOVA followed by Tukey's
765 HSD. *P*-values displayed are for that timepoint vs. the control media condition.
766 **(F)** Differential expression (Wilcoxon rank sum test) for known secreted factors by all non-malignant cells
767 (paracrine) found in basal and classical (x axis) and IT biopsies and the rest (y axis). Subtype-specific
768 genes expressed by non-malignant cells that pass significance after multiple hypothesis correction ($P <$
769 0.05) are colored by their group association.
770 **(G)** Dot plot for the subtype-specific significant differentially expressed paracrine factors. Subtype-specific
771 non-malignant cell types (columns) and significant genes (rows) are binned by subtype association as in
772 **Figure 6C** and **Figure 7F**. Dot size represents that cell type's fraction within tumors of each subtype, and
773 fill color indicates average expression. Only cell types with a fractional representation >5% from each
774 subtype are visualized.
775 **(H)** Cell state diagrams with marginal density plots for organoid cells cultured in control medium (OWRNA,
776 reduced organoid medium, as in **E**) or at 2 time points in control media with IFNγ. *P*-values for group

777 differences between B/C commitment (top) and IT scores (right) were calculated by ANOVA followed by
778 Tukey's HSD. *P*-values displayed are for that timepoint vs. the control media condition.
779
780 *See also Supplemental Figure S7; Supplemental Table S6 & S7.*

781 **METHODS**

782

783 **RESOURCE AVAILABILITY**

784

785 **Lead Contact**

786 Further information and requests for resources and reagents should be sent to and will be fulfilled by
787 Dr. Alex Shalek (shalek@mit.edu).

788

789 **Data Availability**

790 The single-cell RNA sequencing data reported in this paper will be deposited in a central data sharing
791 repository (Genomic Data Commons) under the NCBI Database of Genotypes and Phenotypes (dbGaP).
792 Code will be available upon request.

793

794 **Tissue collection and dissociation.** Investigators obtained written, informed consent from patients with
795 pancreatic cancer for Dana-Farber/Harvard Cancer Center Institutional Review Board (IRB)-approved
796 protocols 11-104, 17-000, 03-189, and/or 14-408 for tissue collection, molecular analysis, and organoid
797 generation. Core needle biopsy specimens were collected and the first core was sent for pathologic
798 analysis. One or more additional cores were then allocated for scRNA-seq and organoid generation.

799 Samples were minced into small portions using a scalpel and then digested at 37°C for 15 minutes
800 using digest medium that consisted of human complete organoid medium (see below), 1 mg/mL
801 collagenase XI (Sigma Aldrich), 10 μg/mL DNase (Stem Cell Technologies), and 10 μM Y27632 (Selleck)
802 (Tiriac et al., 2018). In our initial process optimization, we found that dissociation times below 30 minutes,
803 while not always completely digesting all biopsy material and potentially affecting the representation of
804 difficult to dissociate cell types (e.g., fibroblasts), resulted in greater cell viability and improved RNA
805 quality downstream. After digestion, cells were washed, treated with ACK lysing buffer (Gibco) to lyse
806 red blood cells, washed again, and counted using a hemocytometer with 0.4% Trypan blue (Gibco) added
807 at 1:1 dilution for viability assessment. We allowed residual tissue chunks to settle before selecting a
808 predominance of single cells for counting and Seq-Well processing. We allocated between 10,000 and
809 15,000 viable cells per Seq-Well array based upon total cell counts, and where possible we prepared two
810 arrays per sample. Most samples were processed and loaded onto Seq-Well arrays within 2-3 hours of
811 biopsy acquisition.

812

813 **Organoid generation and sampling.** Cells remaining after scRNA-seq allocation were initiated and
814 maintained as patient-derived organoid cultures as previously described (Boj et al., 2015; Tiriac et al.,
815 2018). In brief, digested cells were seeded in 3-dimensional (3D) Growth-factor Reduced Matrigel
816 (Corning) and fed with human complete organoid medium containing advanced DMEM/F12 (Gibco), 10
817 mM HEPES (Gibco), 1x GlutaMAX (Gibco), 500 nM A83-01 (Tocris), 50 ng/mL mEGF (Peprotech), 100
818 ng/mL mNoggin (Peprotech), 100 ng/mL hFGF10 (Peprotech), 10 nM hGastrin I (Sigma), 1.25 mM N-
819 acetylcysteine (Sigma), 10 mM Nicotinamide (Sigma), 1x B27 supplement (Gibco), R-spondin1
820 conditioned media 10% final, Wnt3A conditioned media 50% final, 100 U/mL penicillin/streptomycin
821 (Gibco), and 1x Primocin (Invivogen) (**Supplemental Table S6**). 10 μM Y27632 (Selleck) was included
822 in the culture medium of newly initiated samples until the first media exchange. For propagation,
823 organoids were dissociated with TrypLE (Gibco) before re-seeding into fresh Matrigel and culture
824 medium.

825 After initial processing of fresh tissue specimens, we monitored samples closely for organoid
826 growth. We did not passage organoids at set time intervals, as there was significant variability in the time
827 needed to establish relatively robust growth of organoids (**Figure 4C**). Instead, we maintained early
828 passage organoids until they reached relative confluence, and then passaged them at low split ratios
829 (1:1, 1:1.5, or 1:2 dilutions) in complete organoid medium to promote continued growth. In one case,
830 PANFR0489R, cells persisted as individuals and small organoids after initiation in complete organoid
831 medium, but did not grow and expand cell numbers significantly. Approximately 15 weeks after initiation,
832 we switched a portion of the surviving cells to organoid medium without A83-01 or mNoggin, and
833 observed renewed growth of organoids under these media conditions but not of those that remained in
834 complete organoid medium. Consequently, we expanded this sample in media without A83-01 or
835 mNoggin, including performing early passage scRNA-seq. After several additional passages, once the
836 organoids were robustly growing, we were able to transition back to complete organoid medium with no
837 apparent change in growth rate, morphology, or transcriptional phenotype. All other serially sampled
838 organoids were maintained and assessed by scRNA-seq in complete medium.

839 For scRNA-seq of organoid samples, we passaged organoids and allowed them to grow for 6
840 days before then dissociating, counting, and allocating 15,000 viable cells for Seq-Well. By standardizing
841 the collection of organoid scRNA-seq samples at 6 days after passaging, we tried to minimize bias arising
842 from cell cycle differences in samples at different degrees of confluence.

843

844 **Testing organoid phenotypes under different matrix and media conditions.** For adaptation of
845 patient-derived organoids onto 2-dimensional (2D) culture surfaces as patient-derived cell lines, tissue
846 culture plates were pre-coated with 100 μg/mL Matrigel dissolved in basal media for 2 hours at 37°C

847 before washing with PBS. Established organoid models were dissociated and seeded onto these
848 Matrigel-coated culture wells in complete organoid media. In parallel, a portion of these passage-matched
849 organoid cells were re-seeded into Matrigel droplets as above. Cells were cultured in both matrix
850 conditions in complete organoid media until they were confluent, approximately 2-3 weeks. Cells were
851 collected and lysed using Trizol before snap freezing. RNA was isolated and purified as described below
852 ("Bulk RNA-sequencing of organoids" section) using chloroform extraction, aqueous phase isolation, and
853 processing using the Qiagen AllPrep DNA/RNA/miRNA Universal kit before being submitted for
854 sequencing.

855 For scRNA-seq assessment of organoid phenotypes when cultured under different media
856 conditions, established organoid models were passaged as above by dissociating and reseeding into
857 Matrigel droplets. A portion of the cells were cultured with complete organoid media ("Complete media"),
858 while a distinct portion of passage-matched cells were cultured in "Minimal" media, which consisted of
859 advanced DMEM/F12 (Gibco), 10 mM HEPES (Gibco), 1x GlutaMAX (Gibco), 100 U/mL
860 penicillin/streptomycin (Gibco), and 1x Primocin (Invivogen) (**Supplemental Table S6**). Cells were
861 cultured for 6 days before being collected, dissociated, and aliquoted for scRNA-seq. Images were taken
862 with an Olympus XM10 camera mounted to an Olympus CKX41 microscope 1 day after seeding and
863 again after 11 days in culture to assess organoid growth in both conditions. The portion of cells cultured
864 in minimal media were maintained in the same conditions for a longer duration and harvested again for
865 scRNA-seq at 27 days and 59 days after the initial introduction of minimal media. To mirror the standard
866 scRNA-seq workflow, the cells harvested at the 27- and 59-day timepoints were collected 6 days after
867 passaging.

868 In addition to the minimal media experiment, organoid cells were also cultured in standard cell
869 line media ("RP10"), which contains RPMI-1640 (Gibco) and 100 U/mL penicillin/streptomycin (Gibco)
870 with 10% fetal bovine serum (Sigma), or in reduced organoid media "OWRNA", which consists of
871 advanced DMEM/F12 (Gibco), 10 mM HEPES (Gibco), 1x GlutaMAX (Gibco), 50 ng/mL mEGF
872 (Peprotech), 100 ng/mL hFGF10 (Peprotech), 10 nM hGastrin I (Sigma), 1.25 mM N-acetylcysteine
873 (Sigma), 10 mM Nicotinamide (Sigma), 1x B27 supplement (Gibco), 100 U/mL penicillin/streptomycin
874 (Gibco), and 1x Primocin (Invivogen) (i.e. complete organoid medium with removal of WNT3A,
875 RSPONDIN-1, NOGGIN, and A-8301; **Supplemental Table S6**). Furthermore, OWRNA reduced
876 organoid medium served as the baseline control medium when assessing the effect of specific factors
877 (IFNGγ and TGF-β1) from the TME on transcriptional phenotypes. Cells were cultured for 6 days before
878 being collected, dissociated, and aliquoted for scRNA-seq in each of the following conditions: RP10,
879 OWRNA, OWRNA with 50 ng/mL IFNGγ (Peprotech), and OWRNA with 5 ng/mL TGFB1 (Peprotech)
880 (**Supplemental Table S6**). The cells cultured under the IFNGγ and TGF-β1 conditions were maintained

881 in culture and harvested again for scRNA-seq 38 days after being introduced to these new media
882 conditions. For these longer duration timepoints, cells were again passaged 6 days before collecting for
883 scRNA-seq.
884
885 **Testing transcriptional phenotype changes in an established cell line under organoid media**
886 **conditions.** For scRNA-seq assessment of transcriptional phenotypes of the established pancreatic
887 cancer cell line CFPAC1 under different media conditions, CFPAC1 cells were cultured in parallel in
888 either standard cell line medium RP10 or complete organoid medium. Cells were cultured for 6 days
889 before being collected, dissociated, and aliquoted for scRNA-seq. Additionally, the CFPAC1 cells cultured
890 under complete organoid medium were maintained in the same conditions and harvested again for
891 scRNA-seq 33 days after the initial introduction of complete organoid medium. CFPAC1 cells grown in
892 complete media for the later 33-day timepoint were collected 6 days after passaging, and media was
893 refreshed 3 days after this final passage.
894
895 **Single-cell RNA-seq (scRNA-seq) data library generation, sequencing, and alignment.** ScRNA-seq
896 processing followed the Seq-Well protocol, uniquely compatible with low-input samples (Gierahn et al.,
897 2017; Hughes et al., 2020). Briefly, arrays were preloaded with RNA capture beads (ChemGenes) and
898 stored in quenching buffer until used. Prior to cell loading, arrays were resuspended in 5 mL RPMI-1640
899 medium with 10% fetal bovine serum (both from Gibco, hereafter referred to as RP10). After dissociation,
900 single-cell suspensions were manually counted and diluted to 15,000 cells per 200 μL of RP10 when cell
901 numbers allowed. Excess RP10 was aspirated from the array and cells were loaded onto arrays. Excess
902 cells were washed off with PBS (4x5 mL, Gibco), briefly left in RPMI (5 mL) and cell+bead pairs were
903 sealed for 40 minutes at 37°C using a polycarbonate membrane (Fisher Scientific NC1421644). Arrays
904 were rocked in lysis buffer for 20 minutes and RNA was hybridized onto the beads for 40 minutes. Beads
905 were removed and reverse transcription was performed overnight using Maxima H Minus Reverse
906 Transcriptase (Thermo Fisher EP0753). Prior to sequencing, the beads underwent an exonuclease
907 treatment (NewEngland Biolabs M0293L) and second strand synthesis *en masse* followed by whole
908 transcriptome amplification (WTA, Kapa Biosystems KK2602) in 1,500 bead reactions (50 μL). cDNA was
909 isolated using Agencourt AMPure XP beads (Beckman Coulter, A63881) at 0.6X SPRI (solid-phase
910 reversible immobilization) followed by a 1X SPRI and quantified using a Qubit dsDNA High Sensitivity
911 assay kit (Thermo Fisher Q32854). Library preparation was performed using Nextera XT DNA
912 tagmentation (Illumina FC-131-1096) and N700 and N500 indices specific to a given sample. Tagmented
913 and amplified sequences were purified with a 0.6X SPRI. cDNA was loaded onto either an Illumina
914 Nextseq (75 Cycle NextSeq500/550v2 kit) or Novaseq (100 Cycle NovaSeq6000S kit, Broad Institute

915 Genomics Platform) at 2.4 pM. Regardless of platform, the paired end read structure was 21 bases (cell
916 barcode and UMI) by 50 bases (transcriptomic information) with an 8 base pair (bp) custom read one
917 primer. The demultiplex and alignment protocol was followed as previously described (Macosko et al.,
918 2015). While Novaseq data were directly output as FASTQs, Nextseq BCL files were converted to
919 FASTQs using bcl2fastq2. The resultant Nextseq and Novaseq FASTQs were demultiplexed by sample
920 based on Nextera N700 and N500 indices. Reads were then aligned to the hg19 transcriptome using the
921 cumulus/dropseq_tools pipeline on Terra maintained by the Broad Institute using standard settings.
922
923 **Bulk RNA-sequencing of organoids.** RNA was obtained for bulk RNA-sequencing from established
924 organoids using one of two approaches. Dissociated organoids were resuspended into cold Matrigel,
925 added as droplets to tissue culture plates (Greiner BioOne), and allowed to polymerize for 30 minutes
926 before addition of media. Organoids were grown for 14-21 days (until confluent) under these conditions
927 with regular media changes. At the time of harvest, cells were washed with cold phosphate buffered
928 saline (PBS) at 4°C, then lysed with Trizol (Invitrogen) before snap-freezing. To isolate RNA, we
929 performed chloroform extraction with isolation of the aqueous phase before processing RNA as per
930 protocols outlined in the Qiagen AllPrep DNA/RNA/miRNA Universal kit.
931 In the second approach, dissociated organoids were resuspended in a solution of 10% Matrigel
932 in complete organoid media (volume/volume) and cultured in ultra-low-attachment culture flasks
933 (Corning). Organoids were grown for 14-21 days (until confluent) before pelleting, washing with cold PBS
934 at 4°C until most Matrigel was dissipated, and then snap frozen. For RNA isolation, cell pellets were
935 homogenized using buffer RLT Plus (Qiagen) and a Precellys homogenizer. Samples were then
936 processed for both DNA extraction and RNA isolation as per the Qiagen AllPrep DNA/RNA/miRNA
937 Universal kit. Purified RNA was then submitted for sequencing by the Broad Institute Genomics Platform.
938 In brief, total RNA was quantified using the Quant-iT RiboGreen RNA Assay Kit (Thermo Fisher
939 R11490) and normalized to 5 ng/μL. Following plating, 2 μL of a 1:1000 dilution of ERCC RNA controls
940 (Thermo Fisher 4456740) were spiked into each sample. An aliquot of 200 ng for each sample was
941 transferred into library preparation which uses an automated variant of the Illumina TruSeq Stranded
942 mRNA Sample Preparation Kit. This method preserves strand orientation of the RNA transcript, and
943 uses oligo dT beads to select mRNA from the total RNA sample followed by heat fragmentation and
944 cDNA synthesis from the RNA template. The resultant 400 bp cDNA then goes through dual-indexed
945 library preparation: 'A' base addition, adapter ligation using P7 adapters, and PCR enrichment using P5
946 adapters. After enrichment, the libraries were quantified using Quant-iT PicoGreen (1:200 dilution;
947 Thermo Fisher P11496). After normalizing samples to 5 ng/μL, the set was pooled and quantified using

948 the KAPA Library Quantification Kit for Illumina Sequencing Platforms. The entire process was performed
949 in 96-well format and all pipetting was done by either Agilent Bravo or Hamilton Starlet.
950 Pooled libraries were normalized to 2 nM and denatured using 0.1 N NaOH prior to sequencing.
951 Flowcell cluster amplification and sequencing were performed according to the manufacturer's protocols
952 using the NovaSeq 6000. Each run was a 101 bp paired-end with an eight-base index barcode read.
953 Data were analyzed using the Broad Picard Pipeline which includes de-multiplexing and data aggregation
954 (https://broadinstitute.github.io/picard/). FASTQ files were then processed as described below (see Bulk
955 RNA-sequencing analysis).
956
957 **Multiplex immunofluorescence imaging.** A multi-marker panel was developed to characterize tumor
958 cell subtype in formalin-fixed paraffin-embedded (FFPE) 4μm tissue sections using multiplex
959 immunofluorescence. The panel comprises markers associated with either a basal (Keratin-17: Thermo
960 Fisher MA513539 and s100a2: Abcam 109494) or classical (cldn18.2: Abcam 241330, GATA6: CST
961 5851 and TFF1: Abcam 92377) subtype. Additionally, DAPI (Akoya Biosciences FP1490) was included
962 for identification of nuclei and pan-cytokeratin (AE1/AE3: DAKO M3515; C11: CST 4545) for identification
963 of epithelial cells. Secondary Opal Polymer HRP mouse and rabbit (ARH1001EA), Tyramide signal
964 amplification and Opal fluorophores (Akoya Biosciences) were used to detect primary antibodies (Keratin-
965 17, Opal 520; s100a2, Opal 650; GATA6, Opal 540; cldn18.2, Opal 570; TFF1, Opal 690; panCK, Opal
966 620). Prior to use in multiplex staining, primary antibodies were first optimized via immunohistochemistry
967 on control tissue to confirm contextual specificity. Monoplex immunofluorescence and iterative multiplex
968 fluorescent staining were then used to optimize staining order, antibody-fluorophore assignments and
969 fluorophore concentrations. Multiplex staining was performed using a Leica BOND RX Research Stainer
970 (Leica Biosystems, Buffalo, IL) with sequential cycles of antigen retrieval, protein blocking, primary
971 antibody incubation, secondary antibody incubation, and fluorescent labeling. Overview images of
972 stained slides were acquired at 10X magnification using a Vectra 3.0 Automated Quantitative Imaging
973 System (Perkin Elmer, Waltham, MA) and regions of interest (ROIs) were selected for multispectral image
974 acquisition at 20X. After unmixing using a spectral library of single-color references, each image was
975 inspected to ensure uniform staining quality and adequate tumor representation.
976
977 **Data analysis**
978 **Mutation and CNV identification from bulk DNA-sequencing.** For targeted DNA-sequencing of clinical
979 samples, next-generation sequencing using a custom-designed hybrid capture library preparation was
980 performed on an Illumina HiSeq 2500 with 2x100 paired-end reads, as previously described (Garcia et
981 al., 2017; Sholl et al., 2016). Sequence reads were aligned to reference sequence b37 edition from the

982 Human Genome Reference Consortium using bwa, and further processed using Picard (version 1.90,
983 http://broadinstitute.github.io/picard/) to remove duplicates and Genome Analysis Toolkit (GATK, version
984 1.6-5-g557da77) to perform localized realignment around indel sites. Single nucleotide variants were
985 called using MuTect v1.1.45, insertions and deletions were called using GATK Indelocator. Copy number
986 variants and structural variants were called using the internally-developed algorithms RobustCNV and
987 BreaKmer followed by manual review (Abo et al., 2015). RobustCNV calculates copy ratios by performing
988 a robust linear regression against a panel of normal samples. The data were segmented using circular
989 binary segmentation, and event identification was performed based on the observed variance of the data
990 points (Bi et al., 2017).
991 We computed the cytoband-level copy number calls and weighted (by length) average segment
992 means across the covered regions of each cytoband using ASCETS (Spurr et al., 2020). Briefly,
993 cytobands were considered amplified/deleted if more than 70% of the covered regions had a log2 copy
994 ratio of greater than 0.2/less than -0.2, and were considered neutral if more than 70% of the covered
995 regions had a log2 copy ratio between -0.2 and 0.2.
996
997 **Single-cell data quality pre-processing and initial cell type discovery.** All single-cell data analysis
998 was performed using the R language for Statistical Computing (v3.5.1). Each biopsy sample's digital
999 gene expression (DGE) matrix (cells x genes) was trimmed to exclude low quality cells (<400 genes
1000 detected; <1,000 UMIs; >50% mitochondrial reads) before being merged together (preserving all unique
1001 genes) to create the larger biopsy dataset. The merged dataset was further trimmed to remove cells with
1002 >8,000 genes which represent outliers and likely doublet cells. We also removed genes that were not
1003 detected in at least 50 cells. The same metrics were applied to the organoid single-cell cohort (see below).
1004 On a per cell basis, UMI count data was divided by total transcripts captured and multiplied by a scaling
1005 factor of 10,000. These normalized values were then natural log transformed for downstream analysis
1006 (i.e. log-normalized cell x gene matrix). Initial exploration of the data was performed using the R package
1007 Seurat (v2.3.4) and followed two steps: 1) SNN-guided quality assessment and 2) cell type composition
1008 determination. In step 1, we intentionally left cells in the DGE matrix of dubious quality (e.g. %
1009 mitochondrial reads >25% but <50%), performed principal component analysis (PCA) over the variable
1010 genes (n = 1,070 genes), and input the first 50 PCs (determined by Jackstraw analysis implemented
1011 through Seurat) to build an SNN graph and cluster the cells (res = 1; k.param = 40). The inclusion of
1012 poor-quality cells essentially acts as a variance "sink" for other poor-quality cells and they cluster together
1013 based on their shared patterns in quality-associated gene expression. This method helped to nominate
1014 additional low quality (e.g. defined exclusively by mitochondrial genes) or likely doublet cells (e.g. clusters
1015 defined by co-expression of divergent lineage markers) which were removed from the dataset (n=1,678

1016 cells). This led to an overall high-quality dataset of single-cells with a low overall faction of mitochondrial
1017 reads (median = 0.09) for downstream analysis (**Supplemental Figure S1B**)
1018 Using the trimmed dataset, we proceeded to step 2 using a very similar workflow as above but
1019 with slightly altered input conditions for defining clusters. Here we used PCs 1-45 and their associated
1020 statistically significant genes for building the SNN graph and determining cluster membership (resolution
1021 = 1.2; k.param = 40). This identified the 36 clusters shown (visualized using *t*-SNE; perplexity, 40;
1022 iterations, 2,500) in **Supplemental Figure S1C**. The expression of known markers was used to collapse
1023 clusters containing shared lineage information. For example, clusters 1, 2, and 4 all express high levels
1024 of macrophage markers—*CD14*, *FCGR3A (CD16)*, *CD68*—and were accordingly collapsed for this first
1025 pass analysis (**Supplemental Figure S1C,G**). To aid our cell type identification, we performed a ROC
1026 test implemented in Seurat to confirm the specificity (power > 0.6) of the top marker genes used to discern
1027 the cell types. Combined with inferred CNV information (see below), this analysis confirmed the presence
1028 of 11 broad non-malignant cell types in our biopsy dataset (**Supplemental Table S2**). Variation in the
1029 SNN graph parameters above did not strongly affect cell type identification.
1030
1031 **Single-cell CNV identification.** To confirm the identity of the putative malignant clusters identified in
1032 **Supplemental Figure S1D**, we estimated single-cell CNVs as previously described by computing the
1033 average expression in a sliding window of 100 genes within each chromosome after sorting the detected
1034 genes by their chromosomal coordinates (Patel et al., 2014; Tirosh et al., 2016b). We used all T/NK, Fib,
1035 Hep, and Endo cells identified above as reference normal populations for this analysis. Complete
1036 information on the inferCNV workflow used for this analysis can be found here
1037 https://github.com/broadinstitute/inferCNV/wiki. To compare with bulk targeted DNA-sequencing, we
1038 collapsed individual probes to cytoband-level information (weighted average of log2 ratios across each
1039 cytoband, see above) within each sample. ScRNA-seq-inferred CNVs showed high concordance across
1040 samples with the bulk measurements and suggests that, at least by this metric, we are likely sampling
1041 the same dominant clones within sequential but distinct cores from each needle biopsy procedure
1042 (**Supplemental Figure S1E**). For plotting CNV profiles in putative malignant versus normal cells
1043 (**Supplemental Figure S1F**), we computed the average CNV signal for the top 5% of altered cells in
1044 each biopsy and correlated all cells in that biopsy to the averaged profile as has been previously
1045 described (Tirosh et al., 2016a). Relation of this correlation coefficient to the CNV score (mean square
1046 deviation from diploidy) in the single cells from each biopsy shows consistent separation of malignant
1047 from non-malignant cells, and, combined with membership in patient-specific SNN clusters, substantiates
1048 the identification of malignant cells in our dataset.
1049

1050 **Subclonal analysis with single-cell inferred CNVs.** The inferCNV workflow can be used to call
1051 subclonal genetic variation with high sensitivity and is comprehensively outlined here
1052 https://github.com/broadinstitute/inferCNV/wiki (Fan et al., 2018; Patel et al., 2014; Tirosh et al., 2016b).
1053 Briefly, we used a six-state Hidden Markov Model (i6-HMM) to predict relative copy number status
1054 (complete loss to >3x gain) across putative altered regions in each cell. A Bayesian latent mixture model
1055 then evaluated the posterior probability that a given copy number alteration is a true positive. We set a
1056 relatively stringent cutoff for this step (BayesMaxPNormal = 0.2) to only include high probability
1057 alterations for downstream clustering. The results of this filtered i6-HMM output were then used to cluster
1058 the single cells using Ward's method. We used inferCNV's "random trees" method to test for statistical
1059 significance ($P < 0.05$, 100 random permutations for each split) at each tree bifurcation and only retained
1060 subclusters that had statistical evidence underlying the presumed heterogeneity. To track subclonal
1061 heterogeneity between biopsy and matched organoid cells in **Figure 3G** and **Supplemental Figure S5E-**
1062 **I**, the above workflow was implemented within each biopsy and the relevant matched organoid samples,
1063 essentially treating all cells as the same "tumor" and allowing the CNVs to determine cell sorting agnostic
1064 to sample-of-origin. The results of the HMM output can be used to infer gene-level information based on
1065 which genes are in the affected window. This (like the rest of the HMM workflow) is computed over groups
1066 of cells (e.g. samples or sub-clones) and used to map *KRAS* and other alterations to samples (**Figure**
1067 **3A-F**) or sub-clones (**Figure 3G, Supplemental Figure S5E-I**).
1068
1069 **Subclustering of malignant and non-malignant cells.** Detailed phenotyping required splitting the
1070 dataset into malignant and non-malignant fractions. After subsetting to only the malignant cells, we re-
1071 scaled the data and ran PCA including the first 35 PCs for SNN clustering and *t*-SNE visualization. This
1072 PCA was used to determine the PanNET identity for PANFR0580 (**Supplemental Figure S2A**). After
1073 removing PANFR0580, we repeated the steps above and used this new PCA for the remainder of PDAC
1074 malignant cell analysis. Subsequent phenotyping for malignant cells is discussed below (**Generation of**
1075 **expression signatures/scores**). A similar approach was used for calling the non-malignant subsets in
1076 **Figure 5A**. To determine the specific phenotypes within T/NK, macrophage, and mesenchymal
1077 populations, we separately subclustered these groups using PCs 1-20 and a resolution of 0.6 in each
1078 case. Of note, subclustering within the macrophages revealed a distinct cluster of cells co-expressing
1079 markers of both T/NK cells and macrophages (n=491 cells). We discarded these cells as likely doublets,
1080 as have others, and re-ran the macrophage PCA and clustering (Zhang et al., 2020; Zilionis et al., 2019).
1081 These cells are included in the full dataset in case they are of interest to others. Each unbiased analysis
1082 helped to define the non-malignant phenotypes summarized in **Figures 5 & 6** and **Supplemental Figure**
1083 **S6**.

1084

1085 **Generation of expression signatures/scores.** All expression scores were computed as previously
1086 described by taking a given input set of genes and comparing their average relative expression to that of
1087 a control set (n=100 genes) randomly sampled to mirror the expression distribution of the genes used for
1088 the input (Tirosh et al., 2016b). While all scores were computed in the same way, choosing the genes for
1089 input varied. We have outlined the relevant approaches below. Where correlations (Pearson's *r)* are
1090 performed over genes, we used the log-transformed UMI count data for each case. Unless otherwise
1091 noted, we selected the top 30 statistically significant genes for each signature (>3 s.d. above the mean
1092 for shuffled data) for visualization and scoring.

1093 ***Cell cycle****.* We utilized previously established signatures for G1/S (n=43 genes) and G2/M (n=55
1094 genes) to place each cell along this dynamic process (Tirosh et al., 2016a). After inspecting the
1095 distribution of scores in the complete dataset, we considered any cell >1.5 s.d. above the mean for either
1096 the G1/S or the G2/M scores to be cycling (van Galen et al., 2019).

1097 ***Basal and classical programs.*** We started by scoring each malignant single cell for the basal-
1098 like and classical genes identified by Moffitt et al., 2015 as these were well described by unbiased
1099 analysis in our data (PCA, **Supplemental Figure S2B**). To determine programs associated with basal
1100 and classical phenotypes, we correlated the aforementioned basal and classical scores to the entire gene
1101 expression matrix containing malignant cells and selected the 1,909 genes significantly associated with
1102 either subtype (r > 0.1; >3 s.d. above the mean for shuffled data, full data in **Supplemental Table S3**).
1103 Biological pathway correlates for basal and classical mirrored previous work, and are summarized in
1104 **Supplemental Figure S3D**,**E**. For visualization, we use the "scCorr" basal and classical genes (top 30
1105 correlated genes for each). We used these basal and classical scores to order the cells by their
1106 polarization or "score difference", simply the difference of the two scores, and revealed a significant
1107 fraction of cells co-expressing intermediate levels of both phenotypes (**Supplemental Figure S3A**,**B**).

1108 ***Intermediate transitional program.*** Intermediate cells showed associations with features across
1109 several additional PCs, but lacked a single dominant axis. To define a consensus set of genes that are
1110 preferentially expressed by cells in this intermediate state, we computed the Euclidean distance to the
1111 line representing equal basal and classical co-expression for each cell. To limit the influence of cell quality
1112 on this analysis and to specifically identify genes related to co-expression, we used cells from each group
1113 (basal, intermediate, and classical) with fractionally low mitochondrial genes (<0.2) and non-zero basal
1114 or classical expression (basal or classical score > 0) and correlated their Euclidean distance
1115 (**Supplemental Figure S3C**) to the entire gene expression matrix of malignant cells. Next, for each gene
1116 positively associated with this intermediate state (Pearson's r >0), we subtracted the second highest
1117 correlation coefficient for each subtype-associated gene (basal and classical), and then re-ranked the

1118 matrix by this corrected value. This enriched for genes more specific to the intermediate state by
1119 excluding those that were also associated with basal or classical programs. We then selected the 115
1120 genes with a corrected correlation value >0.1 (*P< 0.00001*, shuffled data) as our intermediate transitional
1121 (IT) signature (**Supplemental Figure S3D**, **Supplemental Table S3**). Single cells were classified based
1122 on Euclidian distance where <0.2 are defined as intermediate transitional and the remainder (Euclidian
1123 distance >0.2) by their maximal of either basal or classical scores. We binned each organoid cell (e.g.
1124 **Figure 4B**,**C**) by its maximal expression for one of the 3 *in vivo* scores (basal, classical, or IT). Here a
1125 cell must be within 1 s.d. of the mean expression for a given subtype *in vivo*, else it was considered
1126 "organoid-specific" as this program was superimposed on all organoid cells, regardless of their subtype
1127 identity (**Figure 4B**). We used these classifications to summarize overall tumor composition and visualize
1128 the groups. Tumor heterogeneity measures were not significantly affected by changing these cutoffs.

1129 ***Non-Malignant programs.*** TAM signatures were determined similar to above and previous work
1130 (van Galen et al., 2019; Zhang et al., 2020; Zilionis et al., 2019). Using PCA as an anchor (**Supplemental**
1131 **Figure S6C**), we correlated expression within the TAM compartment to either *FCN1*, *SPP1*, or *C1QC*
1132 (top loaded genes on each relevant PC) and merged the resultant correlation coefficients for every
1133 detected gene to the 3 subtypes into one matrix (i.e. a 16,920 x 3 matrix). For each TAM type (i.e. vector
1134 of correlation coeffects to each marker), we first ranked the matrix by decreasing correlation coefficient,
1135 selected only the most significantly associated genes to that type (r > 0.1; >3 s.d. above the mean for
1136 shuffled data), subtracted the second highest correlation coefficient for each subtype-associated gene,
1137 and then re-ranked the matrix by this corrected value. We repeated this procedure for each TAM subtype
1138 independently. This ensures that the genes selected are specific to a given TAM subset and do not
1139 describe general TAM features. The top 30 genes for each were used for scoring and visualization
1140 (**Supplemental Table S2**; **Supplemental Figure S6D**).

1141 CAF phenotypes were determined using a similar workflow. To examine fibroblast heterogeneity,
1142 we removed a subset of adrenal endocrine cells (cluster 4, 40 cells; **Figure 5C**) and then performed PCA
1143 of mesenchymal cells. PC1 was driven by spillover genes (likely contributed from ambient RNA) and
1144 lacked any coherent biological program and was not considered further. PCs 2 and 3 by contrast where
1145 consistent with variable mesenchymal (PC2) and inflammatory (PC3) CAF phenotypes. All these cells
1146 scored highly for previous myCAF gene expression programs so this phenotype did not fully explain the
1147 heterogeneity in mesenchymal cells, but did suggest their identity as CAFs. Again, using correlation, we
1148 determined the genes driving low PC2 scores (Dermal-like), and high PC2 scores (Pericyte-like), as well
1149 as those associated with the high PC3 scores (Inflammatory). As before, we used the top 30 genes for
1150 each subset scoring and visualization. These same genes (Dermal-like and Pericyte-like) were used to

1151 examine bulk RNA-seq profiles and their difference in each sample quantifies which phenotype is favored
1152 in the bulk averages (**Figure 5F**).
1153
1154 **TME associations.** We determined the transcriptional-subtype-dependent composition of the TME
1155 (**Figure 6A**-**C**) following two steps. First, we computed the Simpson's Index (measure of ecological
1156 diversity) using the count of each non-malignant cell type captured from each sample as input (**Figure**
1157 **6A**,**B**) and correlated each biopsy's diversity score to its basal vs. classical commitment score.
1158 Importantly, the number of non-malignant cells captured from each biopsy was not associated with basal
1159 vs. classical commitment score (r = 0.09). Next, to understand which cell types drive these differences,
1160 we computed the fractional representation for every non-malignant cell type in each core needle biopsy
1161 and determined their pairwise correlation distance (Pearson's *r*) followed by hierarchical clustering using
1162 Ward's method (dendrogram in **Figure 6B**). For both of these analyses we only used samples with >200
1163 non-malignant cells captured (**Supplemental Figure S6L**).
1164
1165 **Matched organoid clustering and cell-typing.** After applying similar quality metrics as above, we
1166 performed PCA, SNN clustering, and *t*-SNE embedding for 31,867 cells including organoid cells and all
1167 malignant cells from primary PDAC biopsies (PCs 1-50; resolution=1.2; k.param=45; perplexity=45;
1168 max_iter=2,500), and identified 39 total clusters. Organoids clustered separately from their matched
1169 biopsies, suggesting expression and/or CNV related drift in culture. Only two SNN clusters—clusters 4
1170 and 32—were admixed by sample. We determined the specific gene expression programs in these two
1171 clusters via differential expression testing by Wilcoxon rank sum test ($P < 0.05$, Bonferroni correction;
1172 log(fold change) > 0.5). These comparisons were done in a "1 versus rest" fashion, testing for genes
1173 defining each cluster (4 or 32) compared to the entire dataset. Their expression profiles were consistent
1174 with fibroblasts (cluster 32) and epithelial cells (cluster 4; **Supplemental Figure S5B**,**C**).
1175
1176 **Correlation distances for genotype and phenotype.** To generate correlation distances for genotype
1177 and phenotype, each single cell in a biopsy-organoid pair was represented by two vectors of information:
1178 (i) a phenotype vector containing expression values for basal and classical genes (scCorr basal and
1179 classical genes, n = 60 genes) and (ii) a genotype vector containing the average CNV score for each
1180 cytoband. The phenotype and genotype distances between every single cell within a biopsy/early
1181 organoid pair was computed from these vectors using a correlation-based (Pearson's *r*) distance metric
1182 of the form $d = (1-r)/2$. This resulted in two distance matrices of n x n dimension where n is the total
1183 number of cells from each biopsy/early organoid sample pair. Values in **Figure 4A** are computed by
1184 averaging the values for *d* between only early organoid and matched biopsy cells.

1185

1186 **Matched biopsy vs. organoid malignant cell comparison.** For CNV-confirmed malignant cells from
1187 each biopsy and its matched organoid (earliest passage), we used differential expression (Wilcoxon rank
1188 sum test; $P < 0.05$, Bonferroni correction; log(fold change) > 0.3) to understand the features lost from
1189 malignant cells in the *in vivo* setting and gained when transitioning into growth in organoid culture. We
1190 required any gene to be significantly differentially expressed in at least 3 model-biopsy comparisons to
1191 summarize the consistent changes. We repeated this same workflow for both organoid- and biopsy-
1192 specific genes (**Supplemental Table S5**) outlined in **Figure 4B** and **Figure 4D-F**, respectively.

1193

1194 **Biopsy paracrine and autocrine subtype-specific factor analysis.** Factors present in the TME but
1195 absent from organoid culture could originate from at least two sources, the tumor cells themselves
1196 (autocrine) or non-tumor cells in the local microenvironment (paracrine). We examined any gene with
1197 gene ontology annotations related to "cytokines", "chemokines", or "growth factors" and took the union of
1198 these lists, yielding 321 genes, 218 of which were detected in our dataset. For "autocrine" factors we
1199 performed differential expression between malignant cells binned as basal and classical, and then IT vs
1200 rest. A gene was considered differentially expressed if it passed a $P < 0.05$ with Bonferroni correction
1201 and a log(fold change) > 0.2 in one of these comparisons. Genes were then assigned to subtypes based
1202 on the log fold change direction (**Figure 7D**, **Supplemental Table S7**). Paracrine factors were
1203 determined in a similar manner with slight modifications. We grouped non-tumor cells into basal, classical
1204 or IT based on the average expression and clustering for malignant programs from their respective tumor
1205 samples (**Supplemental Figure S3G**,**H**). We then assessed for differential expression between all cells
1206 from a given group and the rest using the same cutoffs as above and sorted factors into subtypes based
1207 on their log fold change directionality (**Figure 7F**, **Supplemental Table S7**). We then visualized which
1208 cell type contributed the highest average expression for each factor in the cell types from the respective
1209 TMEs (**Figure 7G**).

1210

1211 **Bulk RNA-sequencing analysis.** FASTQs for bulk RNA expression profiles were downloaded from the
1212 relevant repository (TCGA, https://toil.xenahubs.net; PDAC Cell lines,
1213 https://portals.broadinstitute.org/ccle), available in-house (Panc-Seq, metastatic PDAC), or generated for
1214 this study (organoid cohort) (Aguirre et al., 2018; Cancer Genome Atlas Research et al., 2013; Cancer
1215 Genome Atlas Research Network, 2017; Ghandi et al., 2019). All were processed using the same
1216 pipeline. Briefly, each sample's sequences were marked for duplicates and then mapped to hg38 using
1217 STAR. After running QC checks using RNAseqQC, gene-level count matrices were generated using
1218 RSEM. Instructions to run the pipeline are given in the Broad CCLE github repository

1219 https://github.com/broadinstitute/ccle_processing. Length-normalized values (TPM) were then
1220 transformed according to log2(TPM+1) for downstream analysis. The entire dataset was scaled and
1221 centered to allow relative comparisons across sample types (e.g. tumors, organoids, and cell lines).
1222 Signature scores were computed as above (e.g. basal and classical; see **Generation of expression**
1223 **signatures/scores** above) (Puram et al., 2017).
1224
1225 **Tumor phenotyping from mIF data.** Supervised machine learning algorithms were applied for tissue
1226 and cell segmentation (inForm 2.4.1, Akoya Biosciences). Single-cell-level imaging data were exported
1227 and further processed and analyzed using R (v3.6.2). To assign phenotypes to individual tumor epithelial
1228 cells, mean expression intensity in the relevant subcellular compartment was first used to classify cells
1229 as positive or negative for each of the 5 markers. Combinatorial expression patterns for the five markers
1230 were then used to phenotypically classify cells as basal, classical, co-expressing / IT or marker negative
1231 (3 combinations of 2 basal markers, 7 combinations of 3 classical markers, 1 pan-marker negative, 21
1232 combinations of co-expression of basal and classical markers, **Supplemental Figure S4A,**
1233 **Supplemental Table S4**). Tumor subtype composition was assessed by calculating the fraction of total
1234 tumor cells positive for each cell phenotype (**Supplemental Figure S4B**, excluding pan-marker negative
1235 cells).

1236 **SUPPLEMENTAL INFORMATION**

1237

1238 **Supplemental Table S1. Cohort patient characteristics.**

1239 *Related to Figure 1*

1240

1241 **Supplemental Table S2. Normal cell type markers.**

1242 *Related to Figures 1, 5 & 6*

1243

1244 **Supplemental Table S3. Malignant phenotype single-cell gene correlates.**

1245 *Related to Figure 2*

1246

1247 **Supplemental Table S4. mIF marker combinations and cell counts.**

1248 *Related to Figure 2*

1249

1250 **Supplemental Table S5. Organoid- and in vivo malignant-specific gene expression features.**

1251 *Related to Figure 4*

1252

1253 **Supplemental Table S6. Organoid and cell line models and media formulations for perturbation**

1254 **experiments.**

1255 *Related to Figure 7*

1256

1257 **Supplemental Table S7. Subtype-specific autocrine and paracrine secreted factors.**

1258 *Related to Figure 7*

Supplemental Table S1, related to Figure 1. Cohort patient characteristics

This table details the demographic and clinical characteristics of patients whose biopsy samples were used in this study.

Sample (scRNA-seq ID)	Patient age at initial diagnosis	Gender	Ethnicity	Stage at initial diagnosis	Histology	Site of biopsy	Number of cores collected	Number of cores for scRNA-seq/organoids	Treatment of primary disease	Metastatic treatments prior to biopsy	Patient status (alive/ deceased)	Survival time from initial diagnosis (days)[1]
PANFR0383	76	Male	Caucasian	Metastatic	PDAC	Liver	7	2	None	Gemcitabine/Nab-paclitaxel/Anti-hepatocyte growth factor antibody	Deceased	302
PANFR0489 and PANFR0489R[2]	67	Female	Caucasian	Localized	PDAC	Liver	6	2	Whipple; FOLFOX/Nab-paclitaxel; Capecitabine + radiation	Gemcitabine/Nab-paclitaxel; Gemcitabine; 5-FU/Liposomal irinotecan; FOLFOX	Deceased	2068
PANFR0526	72	Male	Caucasian	Metastatic	PDAC	Liver	5	2	None	None	Deceased	10
PANFR0543	65	Male	Caucasian	Metastatic	PDAC	Liver	7	5	None	None	Deceased	120
PANFR0545	75	Female	Caucasian	Metastatic	PDAC	Liver	5	2	None	None	Deceased	94
PANFR0552	49	Female	Caucasian	Localized	PDAC	Liver	4	2	FOLFIRINOX; Whipple; Gemcitabine/Nab-paclitaxel	None	Deceased	536
PANFR0557	44	Female	Caucasian	Localized	PDAC	Liver	4	3	Distal pancreatectomy; Gemcitabine/ Capecitabine	FOLFIRINOX; FOLFIRI	Deceased	1291
PANFR0562	76	Female	Other	Metastatic	PDAC	Liver	5	2	None	None	Deceased	111
PANFR0575	79	Female	Asian	Metastatic	PDAC	Liver	5	2	None	None	Deceased	32
PANFR0576	63	Male	Caucasian	Metastatic	PDAC	Liver	5	2	None	None	Deceased	159
PANFR0578	62	Female	Caucasian	Metastatic	PDAC	Liver	4	1	None	FOLFIRINOX; Lung metastatectomy; FOLFIRINOX; 5-FU + radiation; Olaparib; Whipple	Alive	1863
PANFR0580	53	Male	Caucasian	Metastatic	PanNET	Liver	6	2	None	None	Alive	687
PANFR0583	61	Male	Caucasian	Metastatic	PDAC	Liver	5	2	None	None	Deceased	52
PANFR0588	71	Female	Caucasian	Metastatic	PDAC	Peritoneum	6	2	None	None	Deceased	227
PANFR0592	37	Male	Caucasian	Locally advanced	PDAC	Liver	4	2	FOLFIRINOX; Whipple	None	Deceased	376

PANFR0593	63	Male	Caucasian	Localized	PDAC	Liver	4	2	Distal pancreatectomy; FOLFIRINOX	Gemcitabine/Nab-paclitaxel/Trastuzumab	Alive	199 (lost to follow up)
PANFR0598	75	Male	Caucasian	Metastatic	PDAC	Omentum	7	2	None	None	Alive	586
PANFR0604	67	Female	Caucasian	Metastatic	PDAC	Liver	8	2	None	FOLFIRINOX	Deceased	952
PANFR0605	75	Male	Caucasian	Metastatic	PDAC	Liver	8	3	None	None	Deceased	322
PANFR0631	66	Male	Caucasian	Metastatic	PDAC	Liver	12	2	None	None	Alive	566
PANFR0635	76	Female	Caucasian	Metastatic	PDAC	Omentum	7	3	None	None	Alive	512
PANFR0637	65	Male	Caucasian	Metastatic	PDAC	Adrenal gland	4	2	None	None	Deceased	149

Footnotes

1. Patient survival was calculated as time from initial diagnosis to death or last documented follow up for patients who are alive.
2. This patient had two samples, PANFR0489 and PANFR0489R, collected at different time points along their treatment course.

Supplemental Figure S1, related to Figure 1

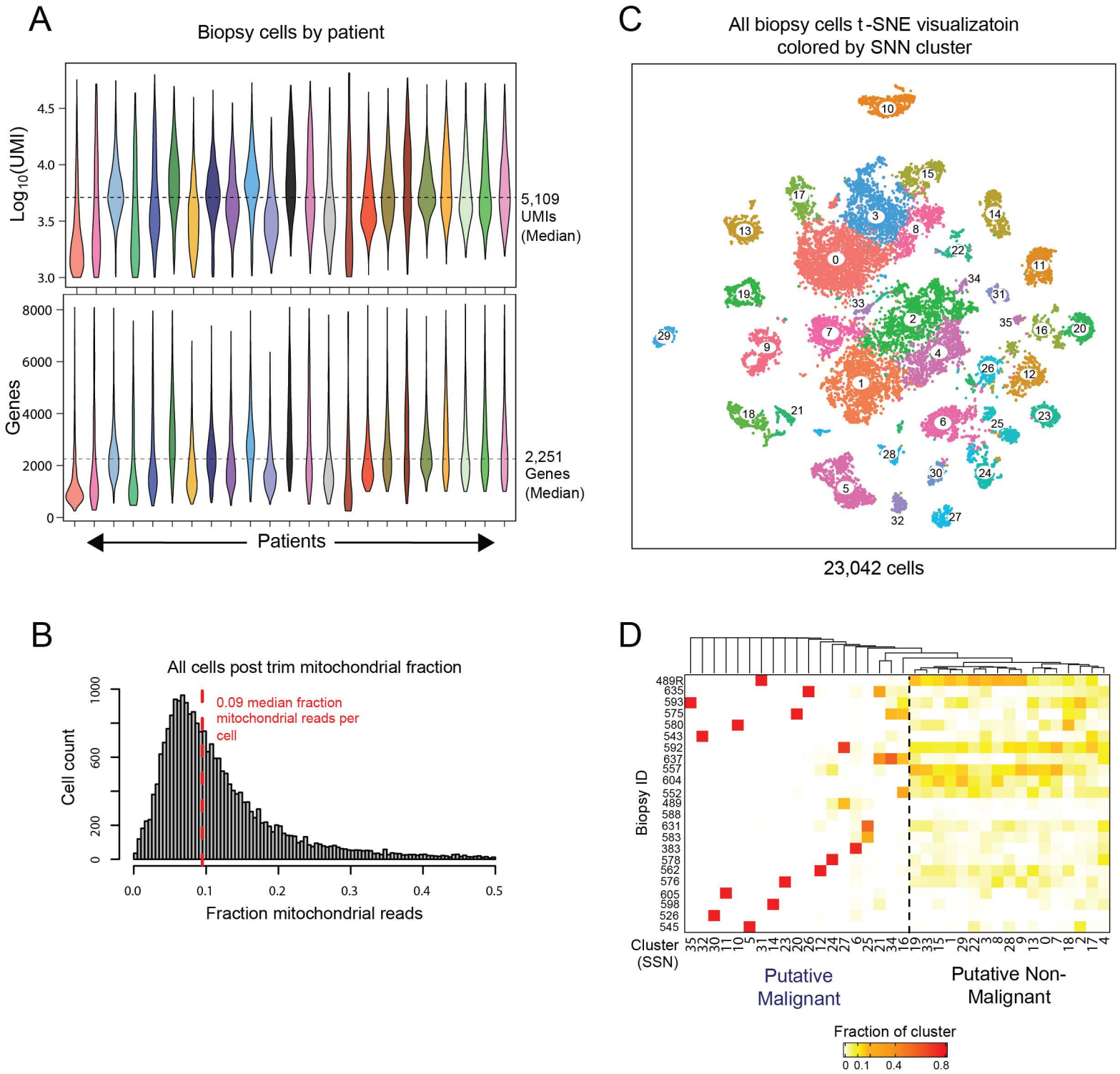

Supplemental Figure S1, related to Figure 1

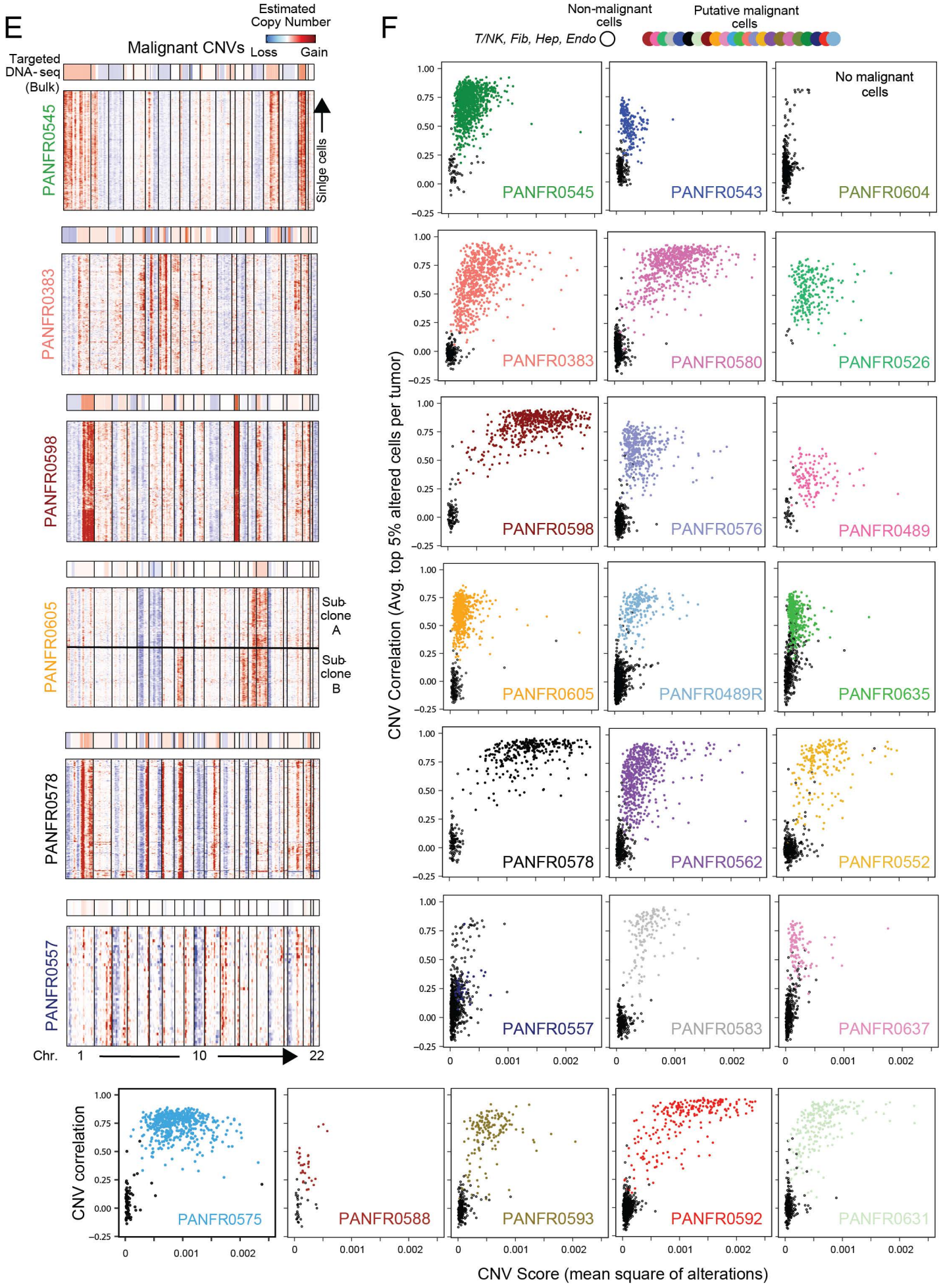

Supplemental Figure S1, related to Figure 1

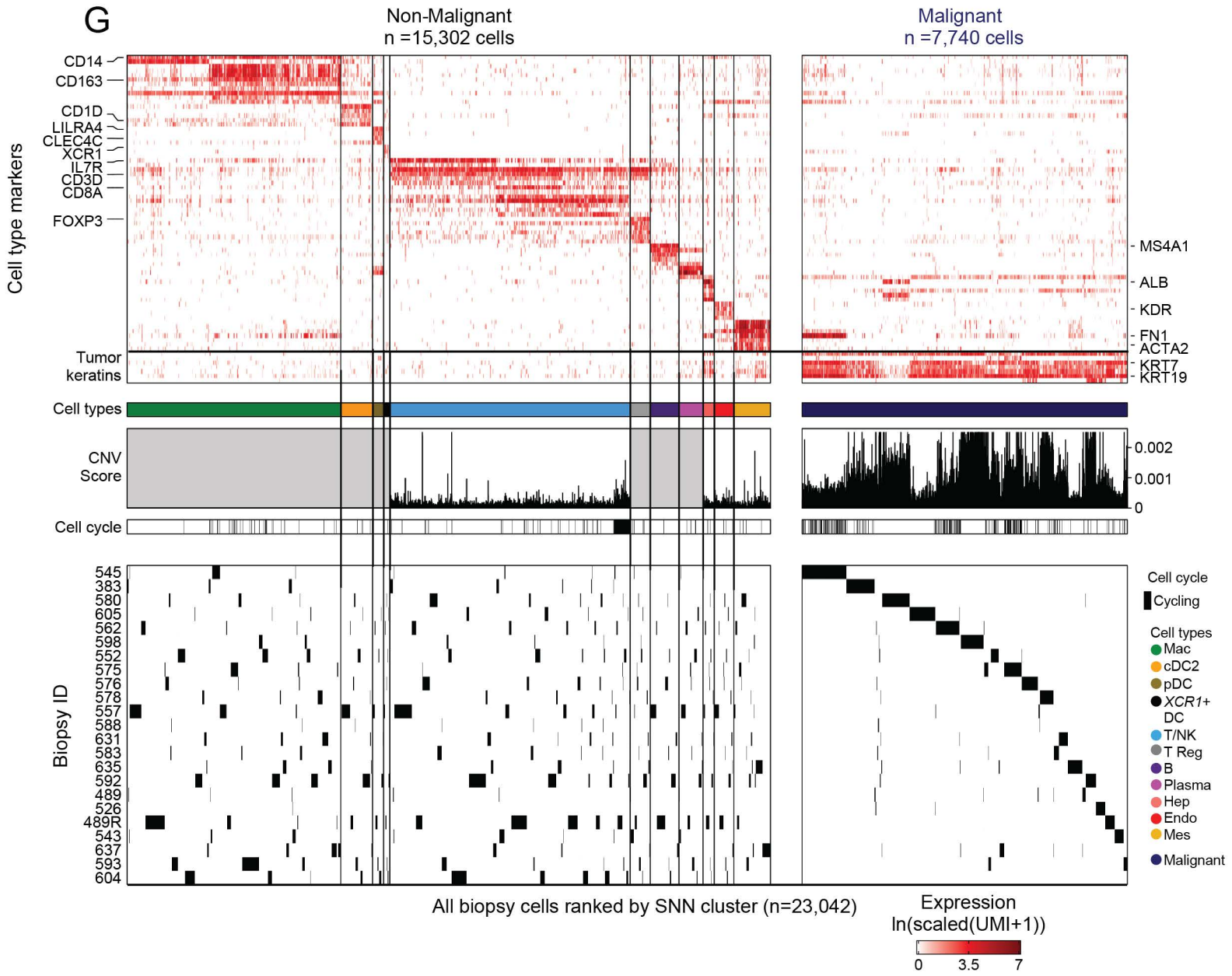

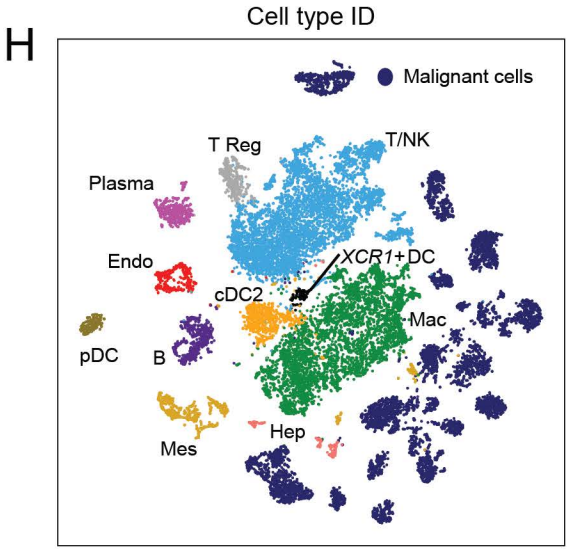

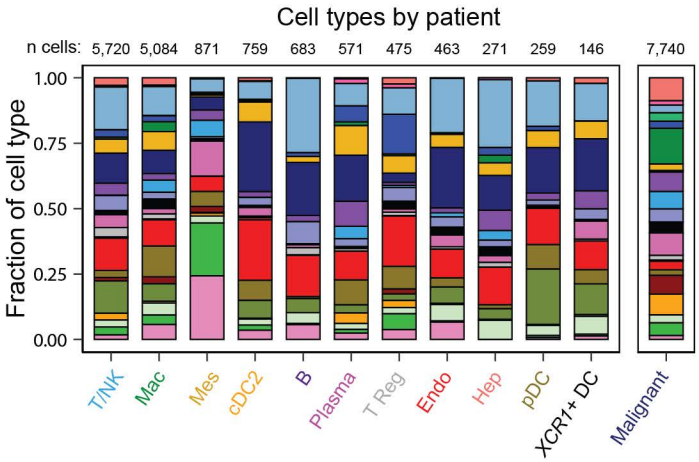

1259 **Supplemental Figure S1. Quality metrics, unsupervised cell type identification, and malignant cell**
1260 **confirmation across the biopsy cohort.**
1261 *Related to Figure 1*
1262 **A**, Distribution of unique molecules and genes captured in quality cells per biopsy, median values are
1263 indicated for each metric (dotted line) and violin plots are colored by patient (top, Log_{10}(UMIs); bottom,
1264 number of genes).
1265 **B**, Distribution of fraction mitochondrial reads across the entire trimmed biopsy dataset (n = 23,042 cells).
1266 Red dotted line denotes the median.
1267 **C**, *t*-SNE visualization of the entire single-cell biopsy dataset colored by the SNN clusters identified (inset
1268 numbers).
1269 **D**, Distribution of single cells captured per biopsy across the identified SNN clusters. In general, a
1270 patient's malignant cells are expected to form unique clusters driven by CNVs. Owing to this feature, the
1271 data are split into putative malignant and non-malignant groups of clusters.
1272 **E**, Heatmaps represent select scRNA-seq-derived copy number profiles where expression across the
1273 transcriptome is organized by chromosome (columns) for each single putative malignant cell (rows) from
1274 a given biopsy. Top bar indicates reference bulk targeted DNA-seq for the same patient and shows strong
1275 concordance with the single-cell derived profiles.
1276 **F**, CNV correlation (averaged top 5% of altered cells per biopsy) versus CNV score (mean square of
1277 modified expression) for each single putative malignant (colored points) and reference normal cell (empty
1278 black circles) within a given biopsy. Only a single sample, PANFR0604, did not contain any malignant
1279 cells.
1280 **G**, Overview of cell-typing for all cells in the biopsy dataset. Cells are ordered by SNN cluster and
1281 separated by cell types. Top heatmap represent expression levels for a subset of select markers (n=73
1282 genes) used to identify cell types. Color bar indicates cell types and binarized cell cycle phenotypes are
1283 labeled (black, cycling; white, not). CNV scores (mean square of alterations per cell) used to parse
1284 malignant from non-malignant are shown using T/NK, endothelial, fibroblasts, and hepatocytes as
1285 reference; grey boxes denote normal cell types where we did not compute reference CNV scores. Bottom
1286 panel shows biopsy of origin for each cell. The data are split by non-malignant (n = 15,302) and malignant
1287 (7,740) identity.
1288 **H**, *t*-SNE visualization as in **S1C** but colored by cell types identified**,** abbreviations as in **Figure 1D**.
1289 **I**, Fraction of each cell type contributed by each biopsy sample (color fill, patient ID; as in **Figure 1B**), cell
1290 type totals are noted at the top of each bar.

Supplemental Figure S2, related to Figures 1 & 2

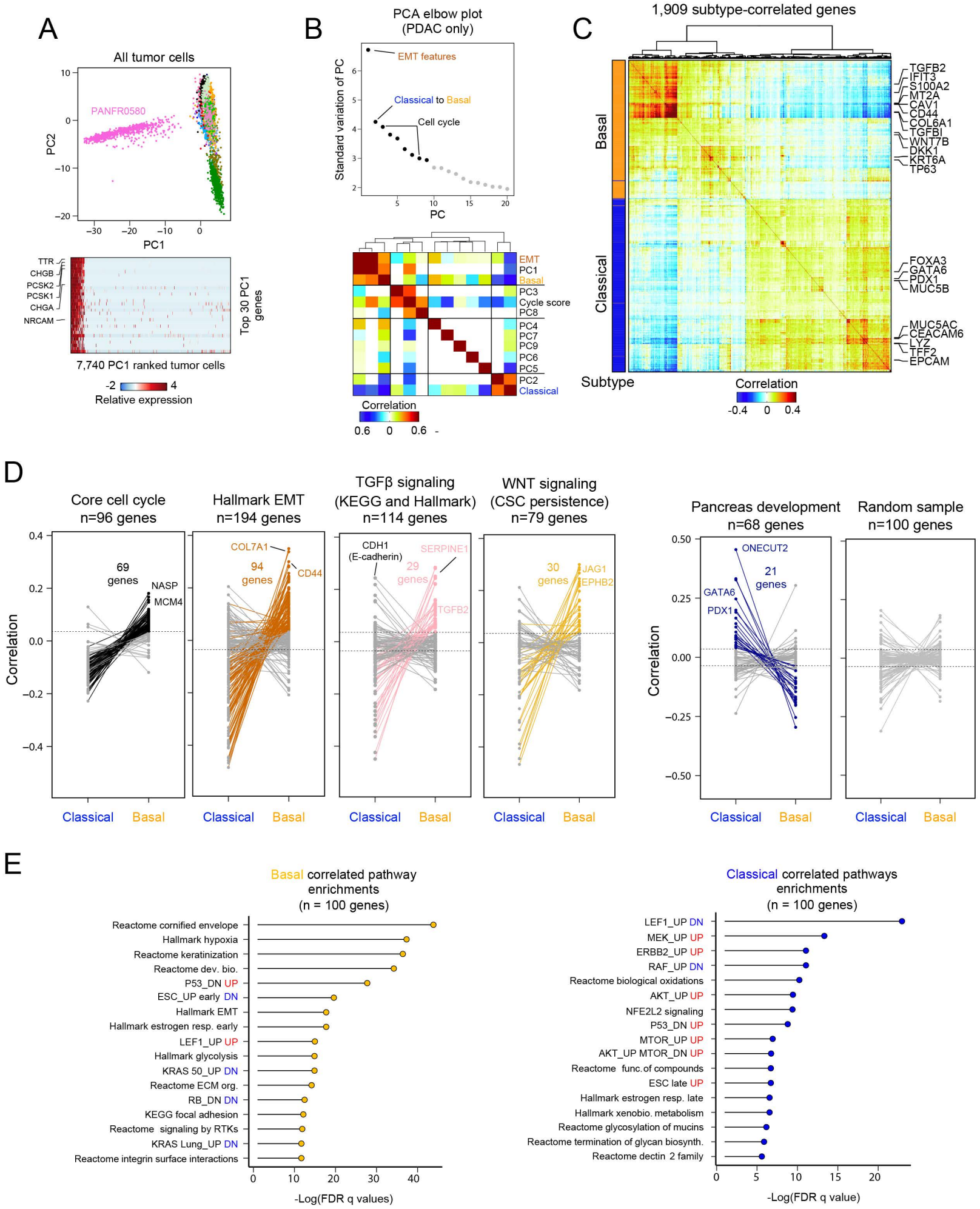

1291 **Supplemental Figure S2. Identifying and contextualizing basal and classical associated biology.**
1292 *Related to Figures 1 & 2*
1293 **A**, Principal component analysis (PCA) and scatter plot for PC1 and PC2 across all malignant cells
1294 (n=7,740) separates PANFR0580's malignant cells (n=662) from the rest of the samples. Cells are
1295 colored by patient ID (as in **Figure 1B**). Heatmap for genes with the strongest negative loading on PC1
1296 (n=30) denote a neuroendocrine identity (*TTR, CHGB*). This tumor was later classified by histology as a
1297 pancreatic neuroendocrine tumor (PanNET).
1298 **B**, Principal component (PC) elbow plot showing the standard deviation for the first 20 components
1299 calculated over the verified PDAC malignant cell variable genes (**Methods**). Line is drawn at the putative
1300 "elbow" (black versus grey points) as inclusion of additional PCs described overlapping information or
1301 quality metrics. Cross-correlational analysis for each single-cell's embeddings across first 9 PCs (black
1302 points) and scores for literature curated gene sets describing EMT, classical and basal, and cell cycle
1303 phenotypes. PC1 positively correlates with EMT, basal, and to a degree, cell cycling. Cells with positive
1304 embeddings on PC2 are correlated with classical phenotypes and anti-correlated with basal and EMT
1305 phenotypes, suggesting these phenotypes are anti-correlated across a continuum of expression. PC3
1306 and PC8 describe cells with high cell cycle scores. The other PCs do not associate significantly with
1307 these phenotypes.
1308 **C**, Pairwise correlation of genes significantly associated with basal (PC1/negative PC2) or classical (PC2)
1309 expression states. Left bar indicates the subtype association of each gene (orange, basal; blue,
1310 classical).
1311 **D**, Tied dot plots depicting the correlation coefficient for each gene (points) to either basal or classical
1312 phenotypes from select literature-derived gene sets, indicated at the top of each plot, which summarize
1313 aspects of subtype associated biology. Dotted lines represent significance threshold (3 SD above the
1314 mean of shuffled data), points and lines are colored if that gene passes the threshold and select genes
1315 are indicated.
1316 **E**, GSEA pathway enrichments for top 100 genes correlated to either basal or classical expression
1317 scores.

Supplemental Figure S3, related to Figure 2

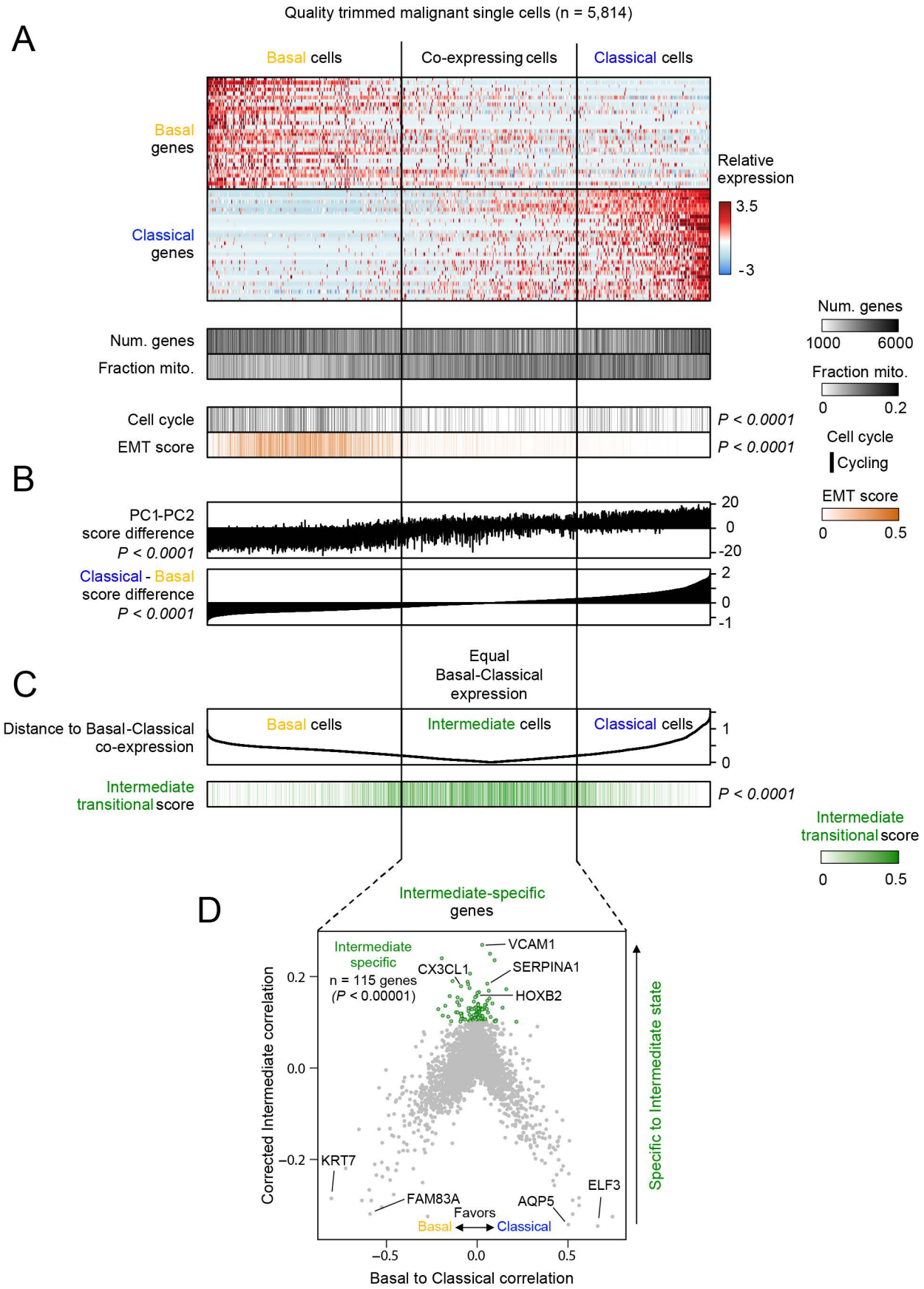

Supplemental Figure S3, related to Figure 2

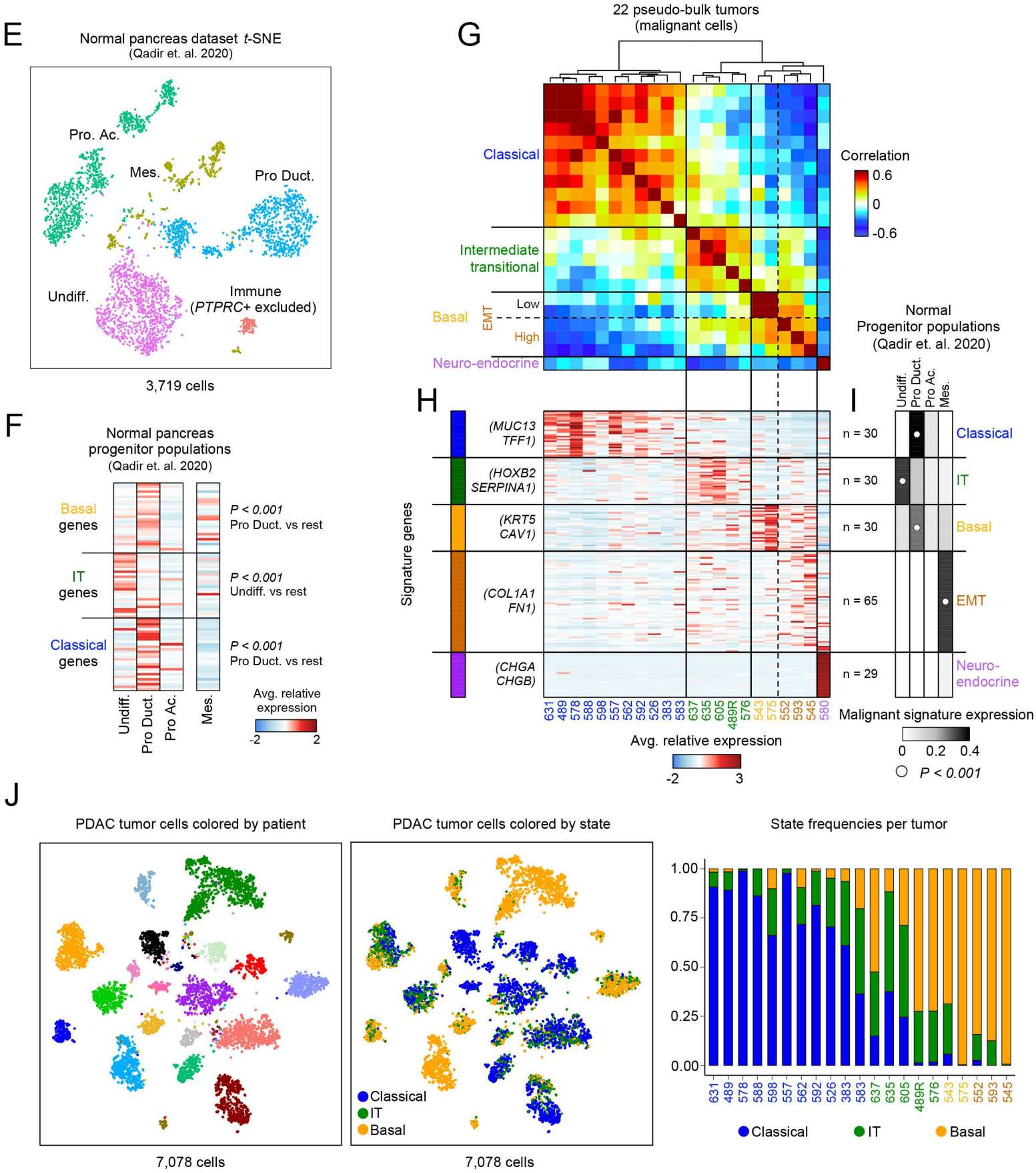

1318 **Supplemental Figure S3. Cells with intermediate co-expressing phenotypes express a distinct**
1319 **gene program.**
1320 *Related to Figure 2*
1321 **A**, Expression of basal and classical gene programs, with cells ordered by their basal-classical score
1322 difference. Quality metrics, EMT scores and the binarized cell cycle program are shown for each single
1323 cell below the heatmap.
1324 **B**, PC1 and 2 difference (top) and Classical – Basal score difference (bottom) are shown. Cells with equal
1325 basal and classical expression are associated with intermediate PC scores and cells are ordered as in
1326 **S3A**.
1327 **C**, Euclidian distance for each cell to co-expression (y = x) of basal (x) and classical (y) expression scores.
1328 Bottom track indicates the score derived from the genes specific to the intermediate state shown in **S3D**
1329 and explained in **Methods**.
1330 **D**, Gene correlation to either basal or classical score (x axis) or the corrected intermediate correlation
1331 (Euclidean distance in **S3C**, **Methods**). Green highlighted genes have corrected intermediate correlation
1332 >0.1 (*P<0.00001* above shuffled). *P*-value for binarized cycling group differences in **S3A** was calculated
1333 using Fisher's Exact test. *P*-values for EMT score in **S3A** and group differences in **S3B** and **S3C** were
1334 calculated by Kruskal-Wallis test with multiple hypothesis correction.
1335 **E**, *t*-SNE visualization after dimensionality reduction and re-clustering for the normal progenitor
1336 populations identified in Qadir et al., 2020. Cell types are collapsed to those favoring Acinar (Pro Ac.),
1337 Ductal (Pro Duct.), or Undifferentiated (Undiff.) subsets. Mesenchymal cells (Mes.) are included as a non-
1338 epithelial reference and the small subset of immune cells was excluded from the comparisons.
1339 **F**, Averaged expression of all three malignant programs in normal pancreatic progenitor niche subsets
1340 and mesenchymal cells defined in Qadir et al., 2020. *P*-values for each set of genes are computed by
1341 Kruskal-Wallis test with multiple hypothesis correction.
1342 **G**, Pairwise correlation for biopsies with malignant cells (n = 22). Data are correlation coefficients for the
1343 average expression of all signature genes in the malignant cells from a given biopsy. EMT genes are
1344 from Groger et al., 2012. Clade identities are at left with the one PanNET tumor (PANFR0580) included
1345 for comparison and PANFR0604 not included due to lack of malignant cells captured.
1346 **H**, Average expression for the 184 genes used for clustering in **S3G**. Clade identity colors match text
1347 color in **S3G** and individual samples (columns) are ordered as in **S3G** and sample ID numbers are
1348 provided below.
1349 **I**, Scores for the expression of genes in **S3H** (grey scale heat) across the 4 main cell types found in the
1350 pancreatic progenitor niche (Qadir et al., 2020). White dot indicates the normal subset with the highest

1351 average expression for each malignant program (Kruskal-Wallis test), none of the normal subsets
1352 significantly express the Neuroendocrine gene signature.
1353 **J**, *t*-SNE visualization for malignant single cells in the biopsy cohort demonstrates intratumoral
1354 transcriptional heterogeneity at the single-cell level. Cells are colored by patient (left) or by transcriptional
1355 subtype (right).

Supplemental Figure S4, related to Figure 2

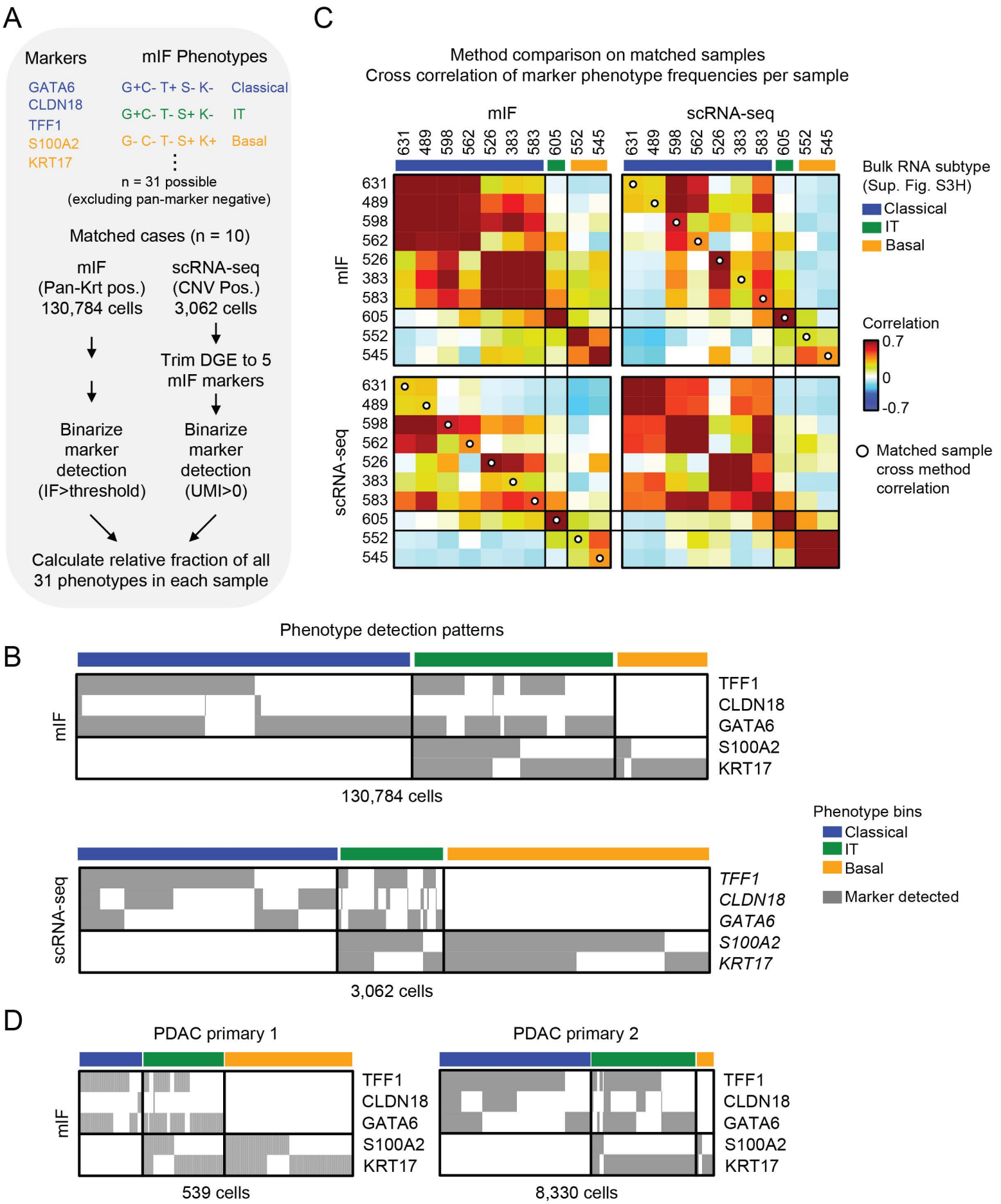

1356 **Supplemental Figure S4. Multiplex immunofluorescence is concordant with scRNA-seq and**
1357 **demonstrates intratumoral heterogeneity with the presence of IT cells.**
1358 *Related to Figure 2*
1359 **A**, Schematic for comparison of the matched datasets by combinatorial marker phenotypes.
1360 **B**, Marker detection in each single cell from the 10 samples in the mIF (top, 130,784 cells) and matched
1361 scRNA-seq datasets (bottom, 3,062 cells). Cells are sorted by their combinatorial phenotype outlined in
1362 **S4A**.
1363 **C**, Comparison within and between modalities on matched samples. Samples are sorted by the
1364 dendrogram in **Supplemental Figure S3G** and labeled with their pseudo-bulk RNA subtype identity.
1365 Correlation is performed over the fractional representation of each mIF phenotype (**S4A**) in each biopsy.
1366 Despite measuring different molecules (protein vs mRNA), the two approaches were highly concordant
1367 within RNA subtypes and on a case-by-case basis (white dots).
1368 **D**, mIF marker detection in each single cell from two primary PDAC samples shown in **Figure 2H**. Cells
1369 are sorted by their combinatorial phenotype outlined in **S4A**.

Supplemental Figure S5, related to Figure 4

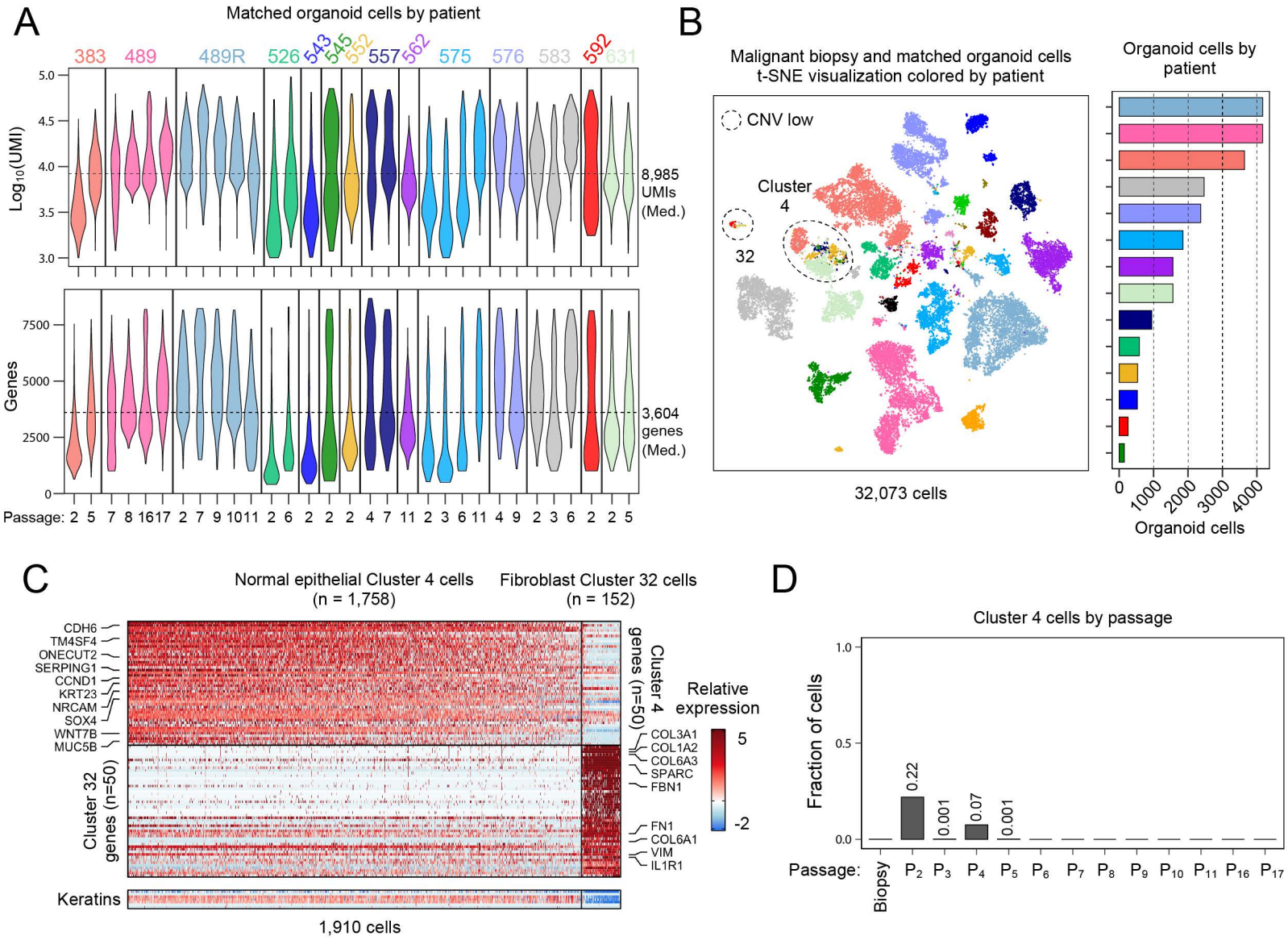

Supplemental Figure S5, related to Figure 4

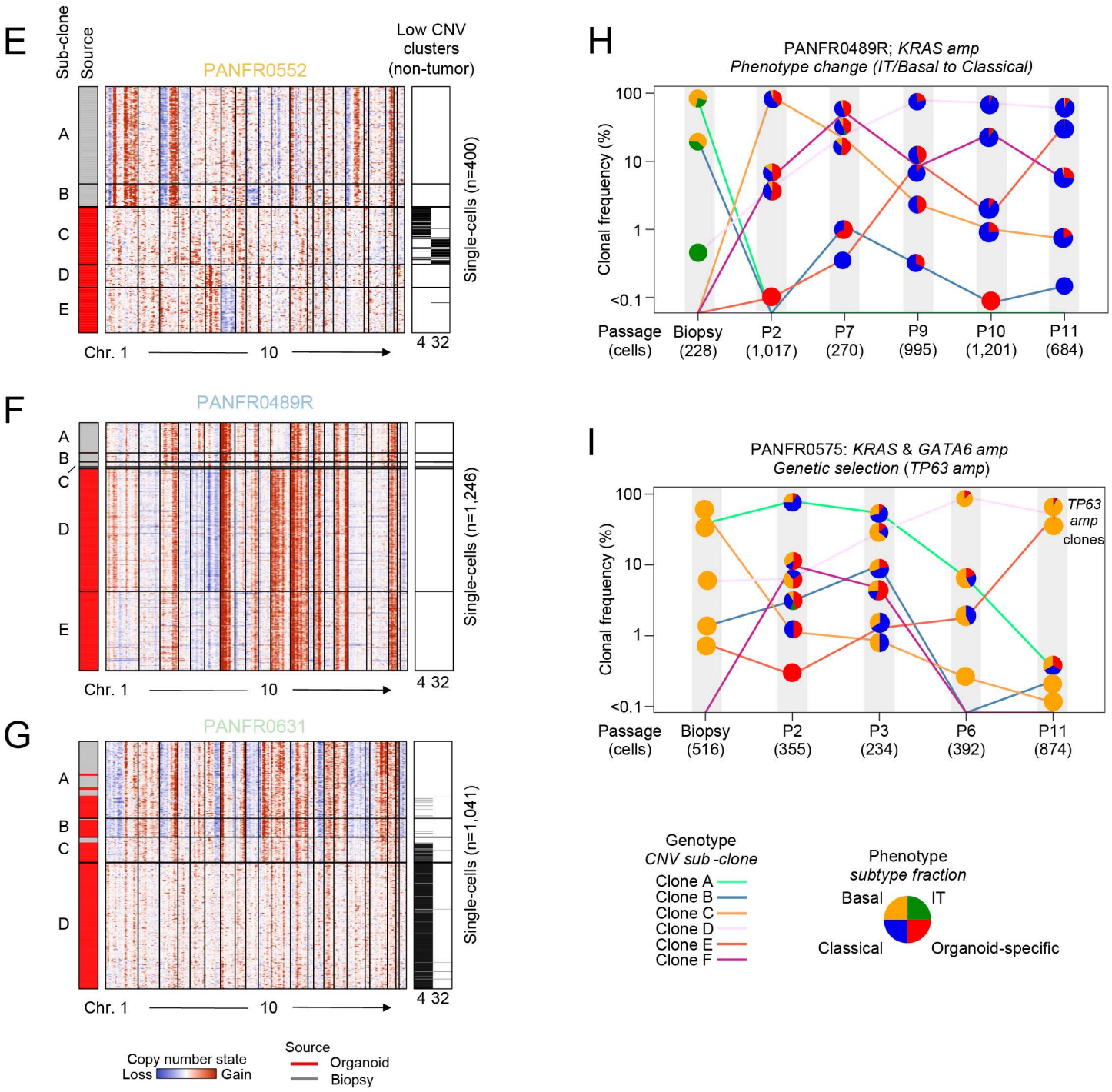

1370 **Supplemental Figure S5. Quality metrics, cell type identification, and serial sampling across the**
1371 **patient-matched organoid cohort.**
1372 *Related to Figure 4*
1373 **A**, Distribution of unique molecules and genes captured in quality cells per organoid sample, median
1374 values are indicated for each metric (dotted line) and violin plots are colored by patient ID (top,
1375 Log_{10}(UMIs); bottom, number of genes).
1376 **B**, *t*-SNE visualization of all biopsy and matched organoid cells from iterative passages, colored by patient
1377 ID. Dotted circles indicate the only two SNN clusters (4 and 32) with appreciably admixed clusters and
1378 low CNV scores, the rest were patient-specific. Bar chart shows number of organoid cells recovered per
1379 matched sample (right).
1380 **C**, Relative expression for genes defining cluster 4 (top) and cluster 32 (bottom; 1 versus rest DE with
1381 the cells in **S5B**). Cluster 4 had an ambiguous epithelial identity while cluster 32 cells were defined by
1382 canonical fibroblast genes and low to absent detection of CNVs.
1383 **D**, Fraction of cluster 4 cells at each passage. These cells did not survive iterative passaging suggesting
1384 that they were either untransformed or unfit in organoid culture.
1385 **E-G**, Heatmaps show inferred CNV copy number status for every cell in each of three biopsy/early
1386 passage organoid pairs. Cells are ordered by hierarchical clustering of their CNV profiles and letters on
1387 the far left indicate subclones that have significant statistical evidence for tree-splitting (**Methods**). Each
1388 cell's origin (biopsy tissue, grey; early passage organoid, red) is also noted ("Source" column). Right
1389 metadata bars indicate if that cell came from an admixed SNN cluster (4 or 32 in **S5B**).
1390 **H**, **I**, Matched phenotype and genotype evolution at each passage in PANFR0489R (**S5H**) and
1391 PANFR0575 (**S5I**). Frequencies of individual CNV clones at each time point (**Methods**, y axis) are tied
1392 by colored lines. Fill represents the transcriptional phenotype fraction for each CNV clone. In sample
1393 PANFR0575 (**S5I**), clones D and E had inferred *TP63* amplifications which expanded over time.

Supplemental Figure S6, related to Figures 5 & 6

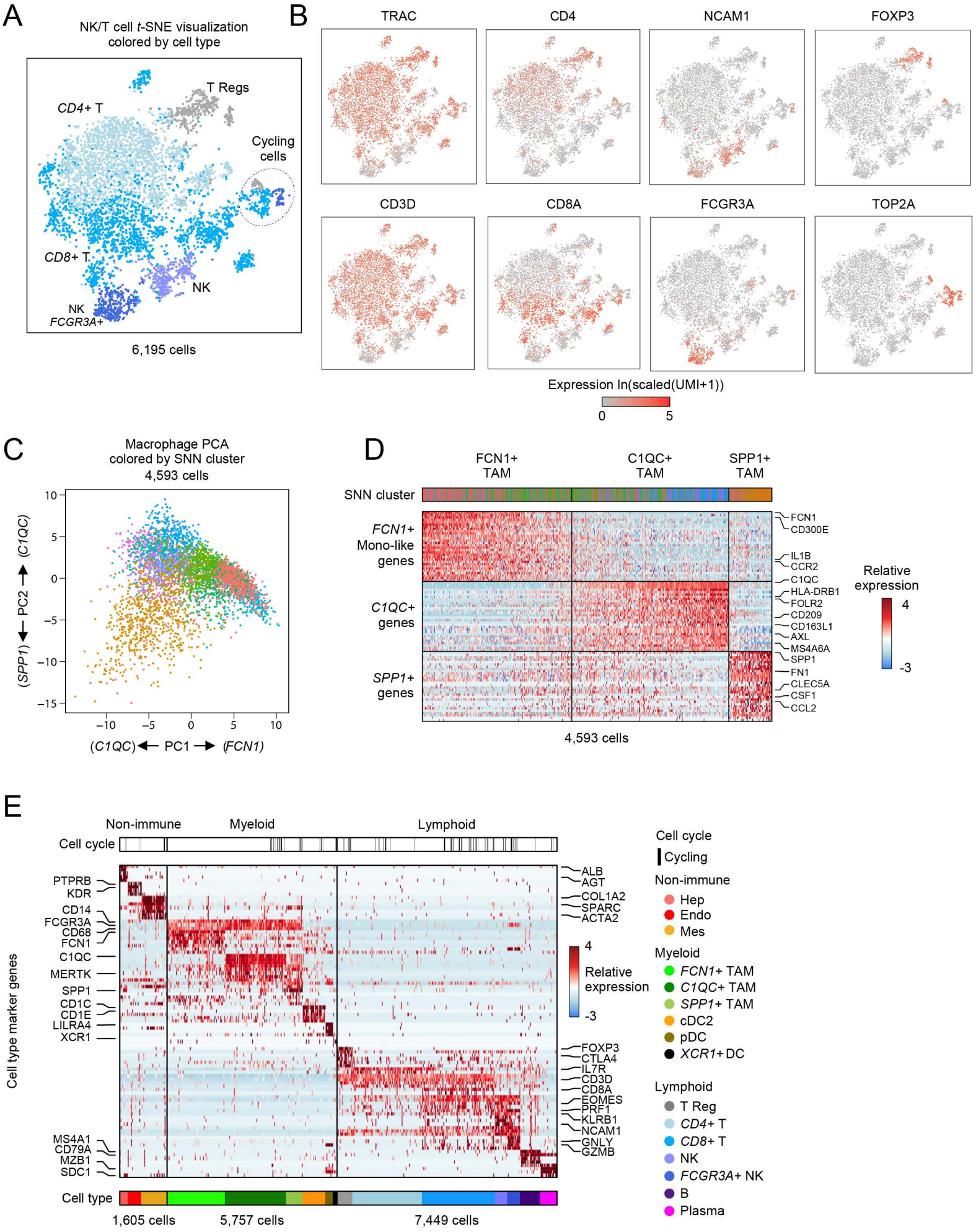

Supplemental Figure S6, related to Figures 5 & 6

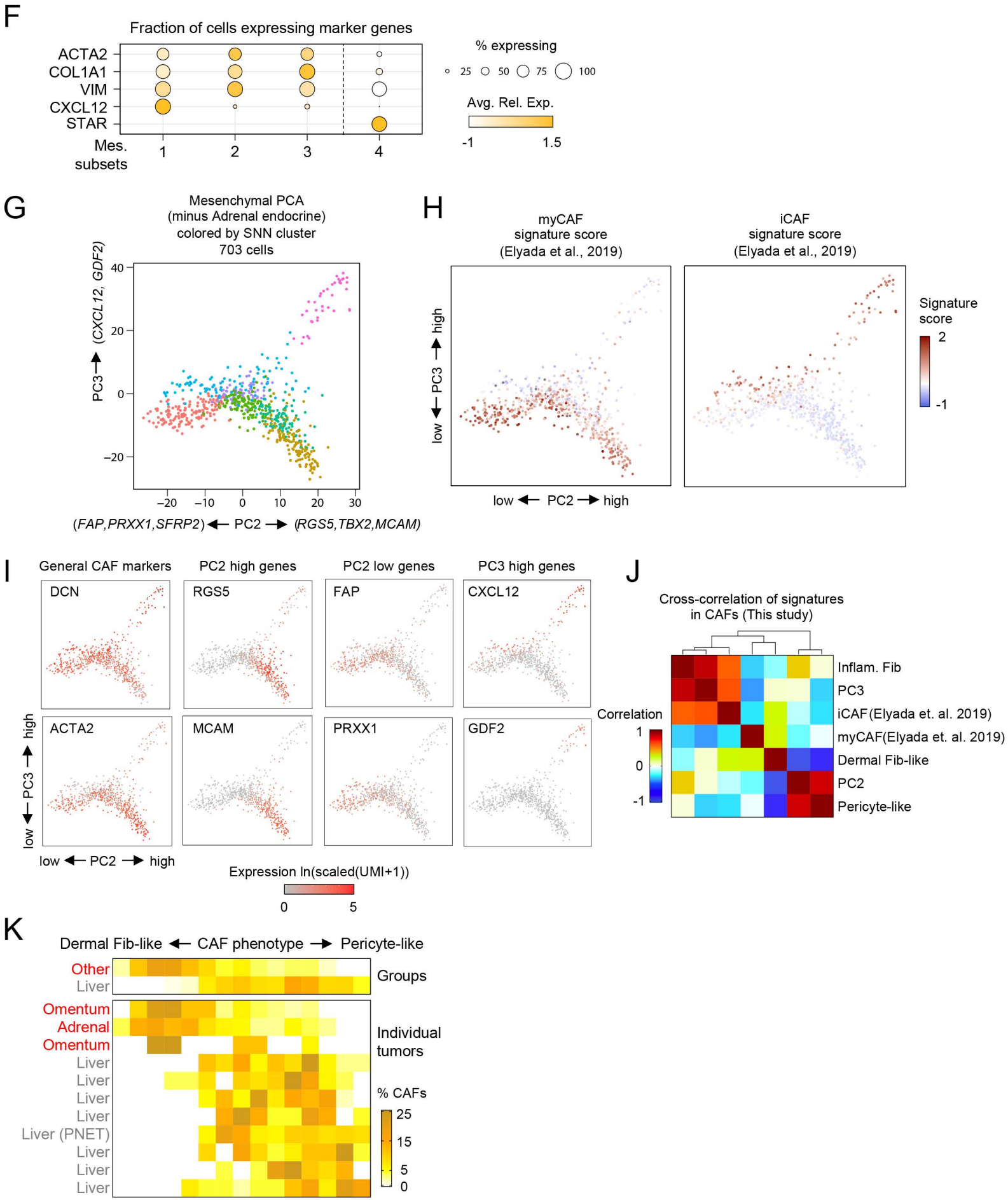

Supplemental Figure S6, related to Figures 5 & 6

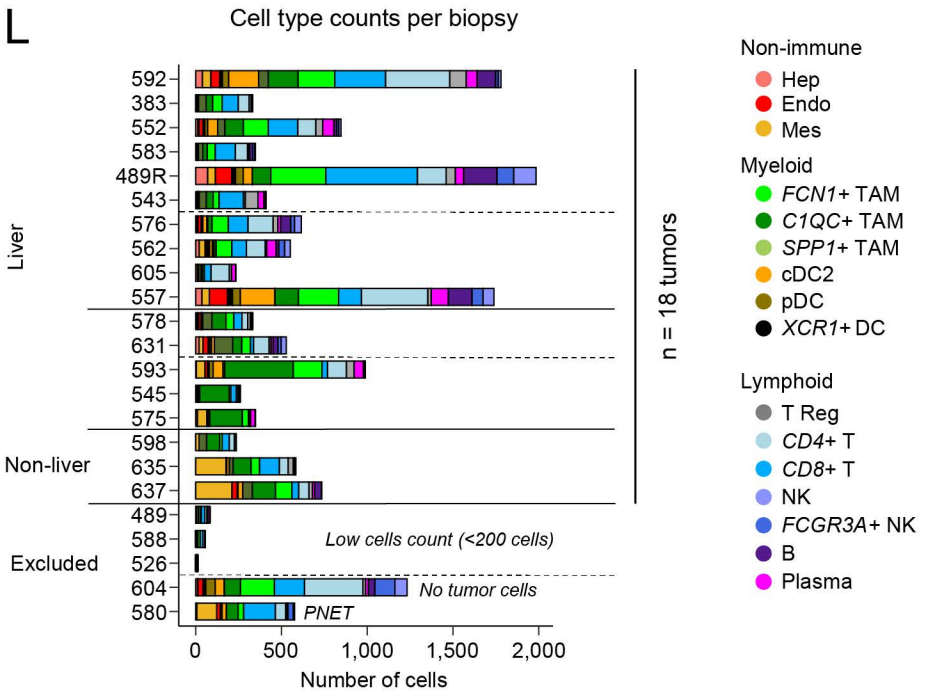

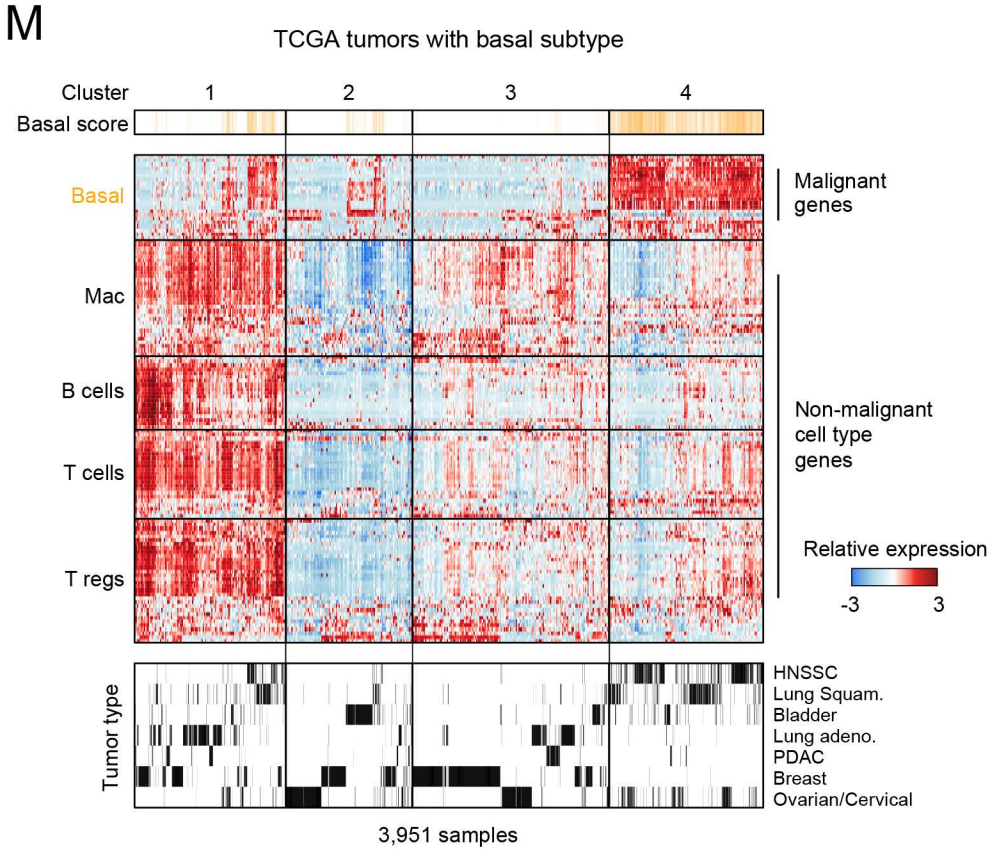

1394 **Supplemental Figure S6. Identification of T/NK, macrophage, and fibroblast heterogeneity in the**
1395 **metastatic microenvironment.**
1396 *Related to Figures 5 & 6*
1397 **A**, *t*-SNE visualization of sub-clustering (SNN) performed on T/NK cells in the metastatic cohort. Cells
1398 are colored by their type identity based on shared SNN cluster membership (Methods).
1399 **B**, Select cell type marker expression overlaid on the *t*-SNE visualization from **S6A.**
1400 **C**, PCA identifies 3 major subsets of TAMs in the metastatic niche. PC1 largely separates *FCN1*+
1401 monocyte-like TAMs from more committed macrophage phenotypes. PC2 separates *SPP1*+ from *C1QC*+
1402 macrophage phenotypes.
1403 **D**, Heatmap visualization of the gene expression programs specific to each TAM subset identified by the
1404 PCA in **S6C** (**Methods**). Top metadata indicate SNN cluster as in **S6C**.
1405 **E**, Heatmap shows the relative expression for select cell type markers. Top bar indicates the binarized
1406 cell cycle program (black, cycling) and the bottom color bar corresponds to the cell type colors noted in
1407 **Figure 6A.**
1408 **F**, Dot plots for average expression of the indicated CAF and adrenal endocrine marker genes in each of
1409 the cell subsets (1-4) identified in **Figure 5C**. Size of the dot indicates fraction of cells expressing a given
1410 gene.
1411 **G**, PCA over fibroblasts in the cohort (excluding Adrenal endocrine cells; subset 4, **Figure 5C**). Scatter
1412 plot of PC2 vs PC3 defines 3 states for CAFs in our cohort (**Methods**).
1413 **H**, Same visualization in **S6B**, but cells are colored by previously identified myCaf or iCaf signature
1414 scores. myCaf is evenly distributed across PC2 and iCaf associates with higher PC3 scores.
1415 **I**, Expression for select markers overlaid on the PCA from **S6B**.
1416 **J**, Cross-correlation of fibroblast signatures in single-cells. New dermal- vs. pericyte-like signatures
1417 provide non-overlapping information. PC3 inflammatory phenotypes are similar to the previously reported
1418 iCaf phenotype (Elyada et al., 2019) and our PC3-derived inflammatory fibroblast signature.
1419 **K**, Distribution across the CAF continuum comparing site differences as groups (top) or individual tumors
1420 (bottom). Heat indicates the fraction of CAFs in that score bin.
1421 **L**, Bar plot shows the number of non-malignant cells in each biopsy, color fill indicates the number of
1422 each cell type captured in that sample. Five biopsies were excluded from the analysis in **Figure 6A**-**C**
1423 because they either had low cell capture or were from a tumor with indeterminant malignant
1424 transcriptional subtype. Relevant samples are organized as in **Figure 6A**.
1425 **M**, Cross TCGA analysis for basal and immune cell type markers in epithelial tumors with known basal
1426 subtypes (Cancer Genome Atlas Research et al., 2013). Tumors with strong basal gene expression do

1427 not associate with strong immune infiltrates. Clusters were determined by dendrogram splitting and
1428 disease type for each sample is indicated below.

Supplemental Figure S7, related to Figure 7

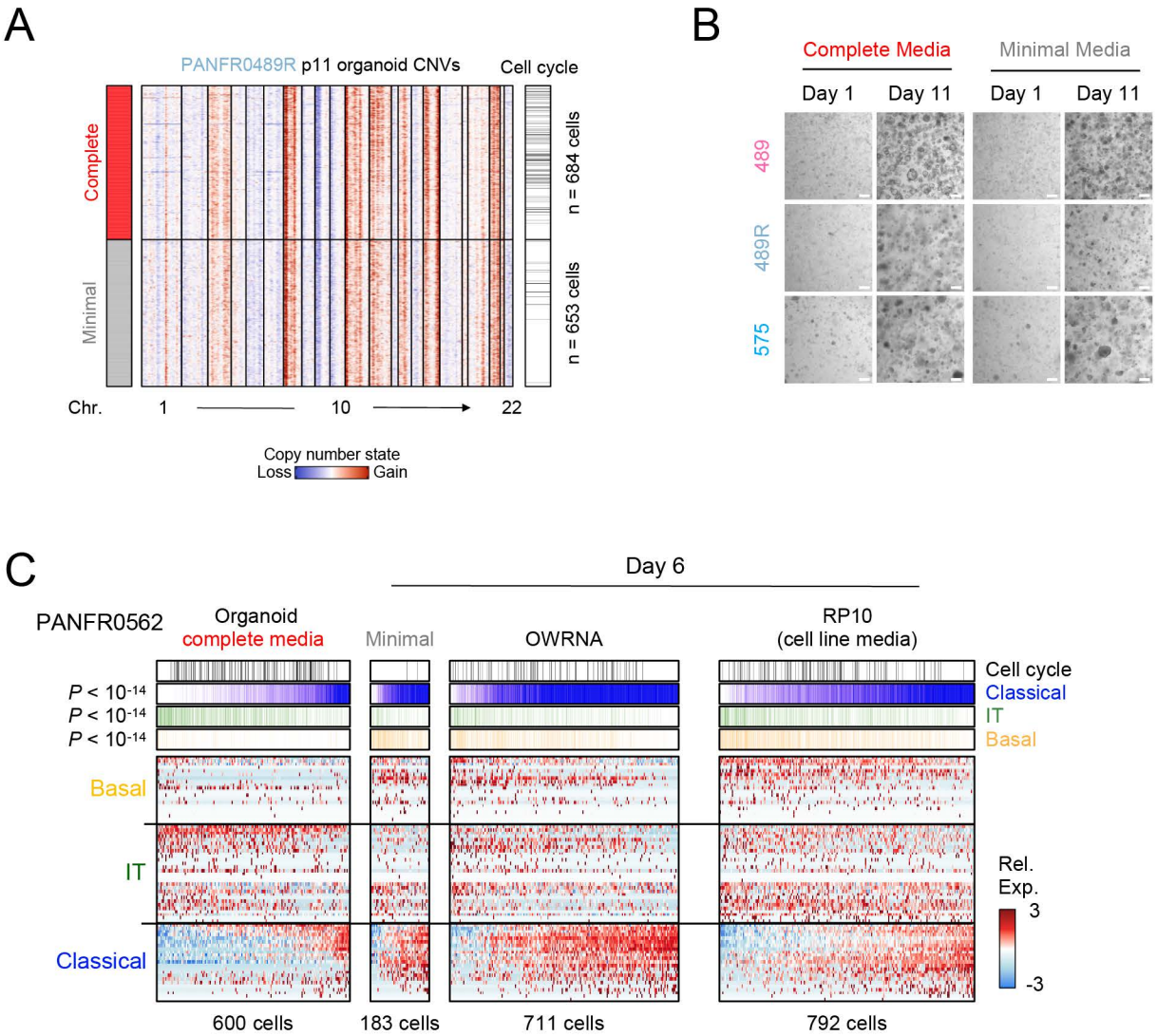

Supplemental Figure S7, related to Figure 7

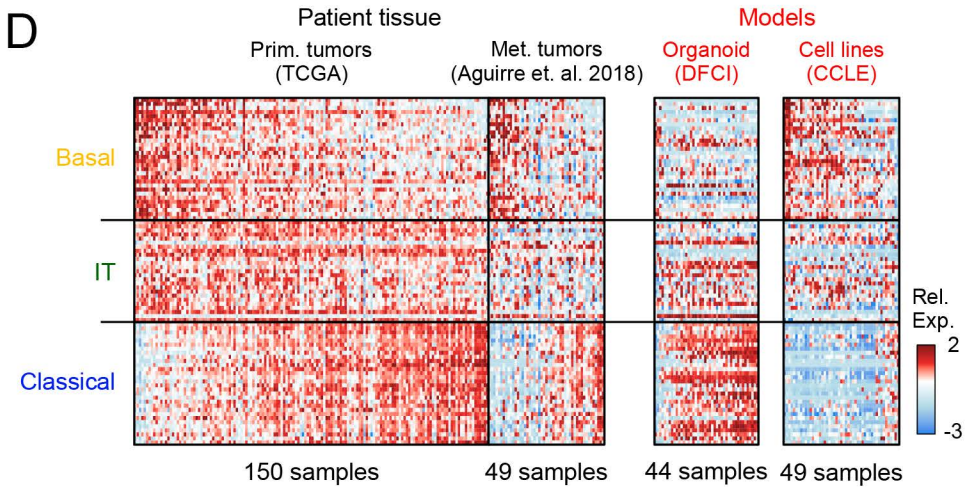

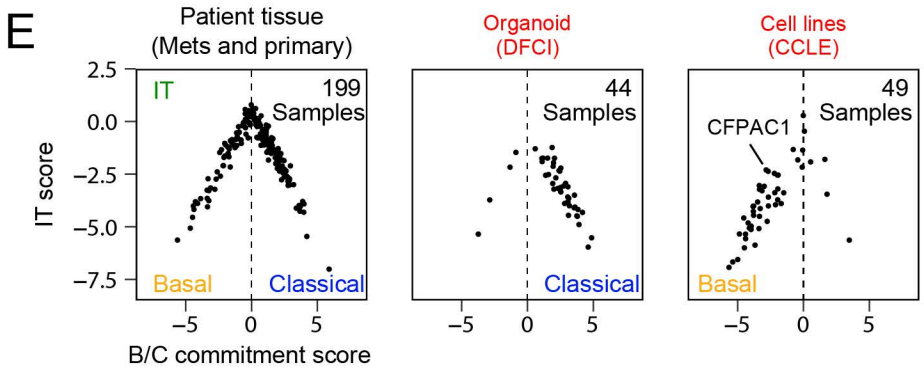

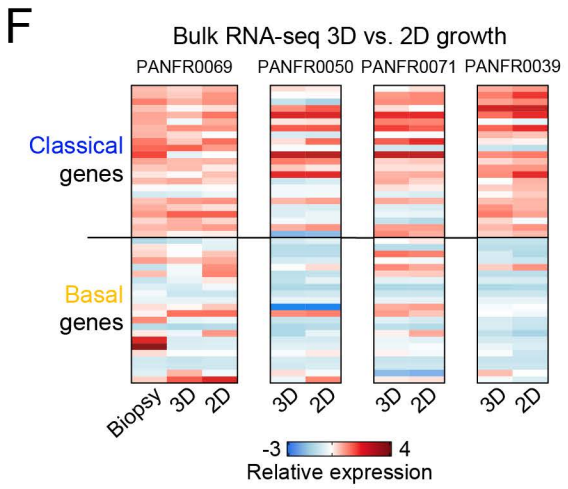

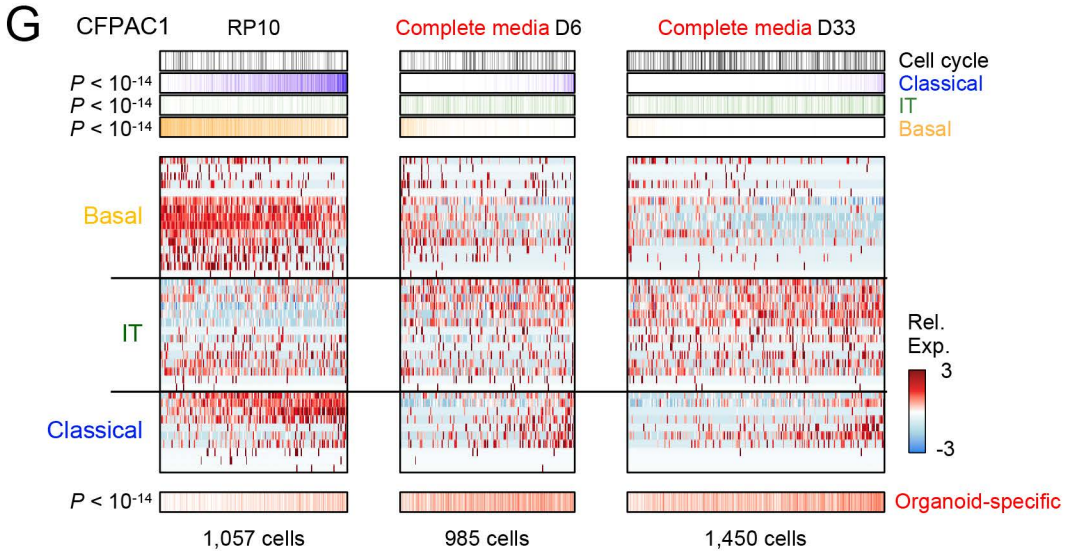

1429 **Supplemental Figure S7. Alterations to organoid media, but not matrix dimensionality, shift**
1430 **transcriptional phenotype.**
1431 *Related to Figure 7*
1432 **A**, Inferred CNVs for each cell from the PANFR489R samples cultured in either Minimal (grey) or
1433 Complete (red) organoid media conditions in **Figure 7B**.
1434 **B**, Brightfield images were obtained for organoids grown in standard organoid media ("Complete") or in
1435 media without any growth factors ("Minimal") at days 1 and 11 after seeding.
1436 **C**, Single organoid cells from model PANFR0562 (columns) cultured for 6 days in Complete medium,
1437 Minimal medium, OWRNA medium, or in RP10 ("cell line" medium, RPMI-1640 with 10% fetal bovine
1438 serum) and scored for basal, IT, and classical hierarchy phenotypes (rows). *P*-values for group
1439 differences were calculated by ANOVA followed by Tukey's HSD.
1440 **D**, Relative expression for 90 genes representing PDAC state programs across bulk RNA-seq samples
1441 from primary resections (TCGA) and metastatic biopsies (Panc-Seq), as well as organoid and cell line
1442 (CCLE) models (Aguirre et al., 2018; Barretina et al., 2012; Cancer Genome Atlas Research Network,
1443 2017; Ghandi et al., 2019).
1444 **E**, PDAC malignant state diagrams for average Basal-classical commitment score (x axis) and IT score
1445 (y axis) for bulk RNA-seq samples in **S7D**.
1446 **F**, Four established models were adapted to 2-dimensional culture in complete organoid media and
1447 measured via bulk RNA-seq. Rows indicate expression levels of basal-classical commitment score
1448 genes.
1449 **G**, Single cells from the established PDAC cell line CFPAC1 (columns) sampled in RP10 (standard "cell
1450 line" medium, RPMI-1640 with 10% fetal bovine serum) or at 2 timepoints in Complete organoid medium
1451 and scored for basal, IT, and classical phenotypes (rows). Bottom row indicates single cell organoid-
1452 specific gene expression (as described in **Figure 4B**) across all three conditions. *P*-values for group
1453 differences were calculated by ANOVA followed by Tukey's HSD.
1454

1455 **REFERENCES**

1456

1457 Abo, R.P., Ducar, M., Garcia, E.P., Thorner, A.R., Rojas-Rudilla, V., Lin, L., Sholl, L.M., Hahn, W.C.,
1458 Meyerson, M., Lindeman, N.I., *et al.* (2015). BreaKmer: detection of structural variation in targeted
1459 massively parallel sequencing data using kmers. Nucleic Acids Res *43*, e19.

1460 Aguirre, A.J., Nowak, J.A., Camarda, N.D., Moffitt, R.A., Ghazani, A.A., Hazar-Rethinam, M., Raghavan,
1461 S., Kim, J., Brais, L.K., Ragon, D., *et al.* (2018). Real-time Genomic Characterization of Advanced
1462 Pancreatic Cancer to Enable Precision Medicine. Cancer Discov *8*, 1096-1111.

1463 Alonso-Curbelo, D., Ho, Y.J., Burdziak, C., Maag, J.L.V., Morris, J.P.t., Chandwani, R., Chen, H.A.,
1464 Tsanov, K.M., Barriga, F.M., Luan, W., *et al.* (2021). A gene-environment-induced epigenetic program
1465 initiates tumorigenesis. Nature *590*, 642-648.

1466 Ascension, A.M., Fuertes-Alvarez, S., Ibanez-Sole, O., Izeta, A., and Arauzo-Bravo, M.J. (2020). Human
1467 Dermal Fibroblast Subpopulations Are Conserved across Single-Cell RNA Sequencing Studies. J Invest
1468 Dermatol.

1469 Aung, K.L., Fischer, S.E., Denroche, R.E., Jang, G.H., Dodd, A., Creighton, S., Southwood, B., Liang,
1470 S.B., Chadwick, D., Zhang, A., *et al.* (2018). Genomics-Driven Precision Medicine for Advanced
1471 Pancreatic Cancer: Early Results from the COMPASS Trial. Clin Cancer Res *24*, 1344-1354.

1472 Bailey, P., Chang, D.K., Nones, K., Johns, A.L., Patch, A.M., Gingras, M.C., Miller, D.K., Christ, A.N.,
1473 Bruxner, T.J., Quinn, M.C., *et al.* (2016). Genomic analyses identify molecular subtypes of pancreatic
1474 cancer. Nature *531*, 47-52.

1475 Balachandran, V.P., Beatty, G.L., and Dougan, S.K. (2019). Broadening the Impact of Immunotherapy to
1476 Pancreatic Cancer: Challenges and Opportunities. Gastroenterology *156*, 2056-2072.

1477 Barretina, J., Caponigro, G., Stransky, N., Venkatesan, K., Margolin, A.A., Kim, S., Wilson, C.J., Lehar,
1478 J., Kryukov, G.V., Sonkin, D., *et al.* (2012). The Cancer Cell Line Encyclopedia enables predictive
1479 modelling of anticancer drug sensitivity. Nature *483*, 603-607.

1480 Bartoschek, M., Oskolkov, N., Bocci, M., Lovrot, J., Larsson, C., Sommarin, M., Madsen, C.D., Lindgren,
1481 D., Pekar, G., Karlsson, G., *et al.* (2018). Spatially and functionally distinct subclasses of breast cancer-
1482 associated fibroblasts revealed by single cell RNA sequencing. Nat Commun *9*, 5150.

1483 Ben-David, U., Beroukhim, R., and Golub, T.R. (2019). Genomic evolution of cancer models: perils and
1484 opportunities. Nat Rev Cancer *19*, 97-109.

1485 Ben-David, U., Ha, G., Tseng, Y.Y., Greenwald, N.F., Oh, C., Shih, J., McFarland, J.M., Wong, B.,
1486 Boehm, J.S., Beroukhim, R., *et al.* (2017). Patient-derived xenografts undergo mouse-specific tumor
1487 evolution. Nat Genet *49*, 1567-1575.

1488 Ben-David, U., Siranosian, B., Ha, G., Tang, H., Oren, Y., Hinohara, K., Strathdee, C.A., Dempster, J.,
1489 Lyons, N.J., Burns, R., *et al.* (2018). Genetic and transcriptional evolution alters cancer cell line drug
1490 response. Nature *560*, 325-330.

1491 Benci, J.L., Xu, B., Qiu, Y., Wu, T.J., Dada, H., Twyman-Saint Victor, C., Cucolo, L., Lee, D.S.M., Pauken,
1492 K.E., Huang, A.C., *et al.* (2016). Tumor Interferon Signaling Regulates a Multigenic Resistance Program
1493 to Immune Checkpoint Blockade. Cell *167*, 1540-1554 e1512.

1494 Bernard, V., Semaan, A., Huang, J., San Lucas, F.A., Mulu, F.C., Stephens, B.M., Guerrero, P.A., Huang,
1495 Y., Zhao, J., Kamyabi, N., *et al.* (2019). Single-Cell Transcriptomics of Pancreatic Cancer Precursors

1496 Demonstrates Epithelial and Microenvironmental Heterogeneity as an Early Event in Neoplastic
1497 Progression. Clin Cancer Res *25*, 2194-2205.

1498 Bi, W.L., Greenwald, N.F., Ramkissoon, S.H., Abedalthagafi, M., Coy, S.M., Ligon, K.L., Mei, Y.,
1499 MacConaill, L., Ducar, M., Min, L.*, et al.* (2017). Clinical Identification of Oncogenic Drivers and Copy-
1500 Number Alterations in Pituitary Tumors. Endocrinology *158*, 2284-2291.

1501 Biffi, G., Oni, T.E., Spielman, B., Hao, Y., Elyada, E., Park, Y., Preall, J., and Tuveson, D.A. (2019). IL1-
1502 Induced JAK/STAT Signaling Is Antagonized by TGFbeta to Shape CAF Heterogeneity in Pancreatic
1503 Ductal Adenocarcinoma. Cancer Discov *9*, 282-301.

1504 Boj, S.F., Hwang, C.I., Baker, L.A., Chio, II, Engle, D.D., Corbo, V., Jager, M., Ponz-Sarvise, M., Tiriac,
1505 H., Spector, M.S.*, et al.* (2015). Organoid models of human and mouse ductal pancreatic cancer. Cell
1506 *160*, 324-338.

1507 Cancer Genome Atlas Research, N., Weinstein, J.N., Collisson, E.A., Mills, G.B., Shaw, K.R.,
1508 Ozenberger, B.A., Ellrott, K., Shmulevich, I., Sander, C., and Stuart, J.M. (2013). The Cancer Genome
1509 Atlas Pan-Cancer analysis project. Nat Genet *45*, 1113-1120.

1510 Cancer Genome Atlas Research Network (2017). Integrated Genomic Characterization of Pancreatic
1511 Ductal Adenocarcinoma. Cancer Cell *32*, 185-203 e113.

1512 Chan-Seng-Yue, M., Kim, J.C., Wilson, G.W., Ng, K., Figueroa, E.F., O'Kane, G.M., Connor, A.A.,
1513 Denroche, R.E., Grant, R.C., McLeod, J.*, et al.* (2020). Transcription phenotypes of pancreatic cancer
1514 are driven by genomic events during tumor evolution. Nat Genet *52*, 231-240.

1515 Collisson, E.A., Sadanandam, A., Olson, P., Gibb, W.J., Truitt, M., Gu, S., Cooc, J., Weinkle, J., Kim,
1516 G.E., Jakkula, L.*, et al.* (2011). Subtypes of pancreatic ductal adenocarcinoma and their differing
1517 responses to therapy. Nat Med *17*, 500-503.

1518 Connor, A.A., Denroche, R.E., Jang, G.H., Lemire, M., Zhang, A., Chan-Seng-Yue, M., Wilson, G., Grant,
1519 R.C., Merico, D., Lungu, I.*, et al.* (2019). Integration of Genomic and Transcriptional Features in
1520 Pancreatic Cancer Reveals Increased Cell Cycle Progression in Metastases. Cancer Cell *35*, 267-282
1521 e267.

1522 Di Carlo, S.E., and Peduto, L. (2018). The perivascular origin of pathological fibroblasts. J Clin Invest
1523 *128*, 54-63.

1524 Elyada, E., Bolisetty, M., Laise, P., Flynn, W.F., Courtois, E.T., Burkhart, R.A., Teinor, J.A., Belleau, P.,
1525 Biffi, G., Lucito, M.S.*, et al.* (2019). Cross-Species Single-Cell Analysis of Pancreatic Ductal
1526 Adenocarcinoma Reveals Antigen-Presenting Cancer-Associated Fibroblasts. Cancer Discov *9*, 1102-
1527 1123.

1528 Fabre, M., Ferrer, C., Dominguez-Hormaetxe, S., Bockorny, B., Murias, L., Seifert, O., Eisler, S.A.,
1529 Kontermann, R.E., Pfizenmaier, K., Lee, S.Y.*, et al.* (2020). OMTX705, a Novel FAP-Targeting ADC
1530 Demonstrates Activity in Chemotherapy and Pembrolizumab-Resistant Solid Tumor Models. Clin Cancer
1531 Res *26*, 3420-3430.

1532 Fan, J., Lee, H.O., Lee, S., Ryu, D.E., Lee, S., Xue, C., Kim, S.J., Kim, K., Barkas, N., Park, P.J.*, et al.*
1533 (2018). Linking transcriptional and genetic tumor heterogeneity through allele analysis of single-cell RNA-
1534 seq data. Genome Res *28*, 1217-1227.

1535 Filbin, M.G., Tirosh, I., Hovestadt, V., Shaw, M.L., Escalante, L.E., Mathewson, N.D., Neftel, C., Frank,
1536 N., Pelton, K., Hebert, C.M.*, et al.* (2018). Developmental and oncogenic programs in H3K27M gliomas
1537 dissected by single-cell RNA-seq. Science *360*, 331-335.

1538 Garcia, E.P., Minkovsky, A., Jia, Y., Ducar, M.D., Shivdasani, P., Gong, X., Ligon, A.H., Sholl, L.M., Kuo,
1539 F.C., MacConaill, L.E., *et al.* (2017). Validation of OncoPanel: A Targeted Next-Generation Sequencing
1540 Assay for the Detection of Somatic Variants in Cancer. Arch Pathol Lab Med *141*, 751-758.

1541 Ghandi, M., Huang, F.W., Jane-Valbuena, J., Kryukov, G.V., Lo, C.C., McDonald, E.R., 3rd, Barretina,
1542 J., Gelfand, E.T., Bielski, C.M., Li, H., *et al.* (2019). Next-generation characterization of the Cancer Cell
1543 Line Encyclopedia. Nature *569*, 503-508.

1544 Gierahn, T.M., Wadsworth, M.H., 2nd, Hughes, T.K., Bryson, B.D., Butler, A., Satija, R., Fortune, S.,
1545 Love, J.C., and Shalek, A.K. (2017). Seq-Well: portable, low-cost RNA sequencing of single cells at high
1546 throughput. Nat Methods *14*, 395-398.

1547 Groger, C.J., Grubinger, M., Waldhor, T., Vierlinger, K., and Mikulits, W. (2012). Meta-analysis of gene
1548 expression signatures defining the epithelial to mesenchymal transition during cancer progression. PLoS
1549 One *7*, e51136.

1550 Hayashi, A., Fan, J., Chen, R., Ho, Y.-j., Makohon-Moore, A.P., Lecomte, N., Zhong, Y., Hong, J., Huang,
1551 J., Sakamoto, H., *et al.* (2020). A unifying paradigm for transcriptional heterogeneity and squamous
1552 features in pancreatic ductal adenocarcinoma. Nature Cancer *1*, 59-74.

1553 Ho, W.J., Jaffee, E.M., and Zheng, L. (2020). The tumour microenvironment in pancreatic cancer - clinical
1554 challenges and opportunities. Nat Rev Clin Oncol *17*, 527-540.

1555 Hosaka, K., Yang, Y., Seki, T., Fischer, C., Dubey, O., Fredlund, E., Hartman, J., Religa, P., Morikawa,
1556 H., Ishii, Y., *et al.* (2016). Pericyte-fibroblast transition promotes tumor growth and metastasis. Proc Natl
1557 Acad Sci U S A *113*, E5618-5627.

1558 Hovestadt, V., Smith, K.S., Bihannic, L., Filbin, M.G., Shaw, M.L., Baumgartner, A., DeWitt, J.C., Groves,
1559 A., Mayr, L., Weisman, H.R., *et al.* (2019). Resolving medulloblastoma cellular architecture by single-cell
1560 genomics. Nature *572*, 74-79.

1561 Hughes, T.K., Wadsworth, M.H., 2nd, Gierahn, T.M., Do, T., Weiss, D., Andrade, P.R., Ma, F., de
1562 Andrade Silva, B.J., Shao, S., Tsoi, L.C., *et al.* (2020). Second-Strand Synthesis-Based Massively
1563 Parallel scRNA-Seq Reveals Cellular States and Molecular Features of Human Inflammatory Skin
1564 Pathologies. Immunity *53*, 878-894 e877.

1565 Hyman, D.M., Taylor, B.S., and Baselga, J. (2017). Implementing Genome-Driven Oncology. Cell *168*,
1566 584-599.

1567 Kim, C., Gao, R., Sei, E., Brandt, R., Hartman, J., Hatschek, T., Crosetto, N., Foukakis, T., and Navin,
1568 N.E. (2018). Chemoresistance Evolution in Triple-Negative Breast Cancer Delineated by Single-Cell
1569 Sequencing. Cell *173*, 879-893 e813.

1570 Kim, J.H., Park, S.Y., Jun, Y., Kim, J.Y., and Nam, J.S. (2017). Roles of Wnt Target Genes in the Journey
1571 of Cancer Stem Cells. Int J Mol Sci *18*.

1572 Li, J., Byrne, K.T., Yan, F., Yamazoe, T., Chen, Z., Baslan, T., Richman, L.P., Lin, J.H., Sun, Y.H., Rech,
1573 A.J., *et al.* (2018). Tumor Cell-Intrinsic Factors Underlie Heterogeneity of Immune Cell Infiltration and
1574 Response to Immunotherapy. Immunity *49*, 178-193 e177.

1575 Li, Y., He, Y., Peng, J., Su, Z., Li, Z., Zhang, B., Ma, J., Zhuo, M., Zou, D., Liu, X., *et al.* (2021). Mutant
1576 Kras co-opts a proto-oncogenic enhancer network in inflammation-induced metaplastic progenitor cells
1577 to initiate pancreatic cancer. Nature Cancer *2*, 49-65.

1578 Ligorio, M., Sil, S., Malagon-Lopez, J., Nieman, L.T., Misale, S., Di Pilato, M., Ebright, R.Y., Karabacak,
1579 M.N., Kulkarni, A.S., Liu, A., *et al.* (2019). Stromal Microenvironment Shapes the Intratumoral
1580 Architecture of Pancreatic Cancer. Cell *178*, 160-175 e127.

1581 Macosko, E.Z., Basu, A., Satija, R., Nemesh, J., Shekhar, K., Goldman, M., Tirosh, I., Bialas, A.R.,
1582 Kamitaki, N., Martersteck, E.M., *et al.* (2015). Highly Parallel Genome-wide Expression Profiling of
1583 Individual Cells Using Nanoliter Droplets. Cell *161*, 1202-1214.

1584 Miyabayashi, K., Baker, L.A., Deschênes, A., Traub, B., Caligiuri, G., Plenker, D., Alagesan, B., Belleau,
1585 P., Li, S., Kendall, J., *et al.* (2020). Intraductal Transplantation Models of Human Pancreatic Ductal
1586 Adenocarcinoma Reveal Progressive Transition of Molecular Subtypes. Cancer Discovery *10*, 1566-
1587 1589.

1588 Moffitt, R.A., Marayati, R., Flate, E.L., Volmar, K.E., Loeza, S.G., Hoadley, K.A., Rashid, N.U., Williams,
1589 L.A., Eaton, S.C., Chung, A.H., *et al.* (2015). Virtual microdissection identifies distinct tumor- and stroma-
1590 specific subtypes of pancreatic ductal adenocarcinoma. Nat Genet *47*, 1168-1178.

1591 Muzumdar, M.D., Chen, P.Y., Dorans, K.J., Chung, K.M., Bhutkar, A., Hong, E., Noll, E.M., Sprick, M.R.,
1592 Trumpp, A., and Jacks, T. (2017). Survival of pancreatic cancer cells lacking KRAS function. Nat
1593 Commun *8*, 1090.

1594 Nam, A.S., Chaligne, R., and Landau, D.A. (2021). Integrating genetic and non-genetic determinants of
1595 cancer evolution by single-cell multi-omics. Nat Rev Genet *22*, 3-18.

1596 Neftel, C., Laffy, J., Filbin, M.G., Hara, T., Shore, M.E., Rahme, G.J., Richman, A.R., Silverbush, D.,
1597 Shaw, M.L., Hebert, C.M., *et al.* (2019). An Integrative Model of Cellular States, Plasticity, and Genetics
1598 for Glioblastoma. Cell *178*, 835-849 e821.

1599 O'Kane, G.M., Grunwald, B.T., Jang, G.H., Masoomian, M., Picardo, S., Grant, R.C., Denroche, R.E.,
1600 Zhang, A., Wang, Y., Lam, B., *et al.* (2020). GATA6 Expression Distinguishes Classical and Basal-like
1601 Subtypes in Advanced Pancreatic Cancer. Clin Cancer Res.

1602 Ohlund, D., Handly-Santana, A., Biffi, G., Elyada, E., Almeida, A.S., Ponz-Sarvise, M., Corbo, V., Oni,
1603 T.E., Hearn, S.A., Lee, E.J., *et al.* (2017). Distinct populations of inflammatory fibroblasts and
1604 myofibroblasts in pancreatic cancer. J Exp Med *214*, 579-596.

1605 Patel, A.P., Tirosh, I., Trombetta, J.J., Shalek, A.K., Gillespie, S.M., Wakimoto, H., Cahill, D.P., Nahed,
1606 B.V., Curry, W.T., Martuza, R.L., *et al.* (2014). Single-cell RNA-seq highlights intratumoral heterogeneity
1607 in primary glioblastoma. Science *344*, 1396-1401.

1608 Pelon, F., Bourachot, B., Kieffer, Y., Magagna, I., Mermet-Meillon, F., Bonnet, I., Costa, A., Givel, A.M.,
1609 Attieh, Y., Barbazan, J., *et al.* (2020). Cancer-associated fibroblast heterogeneity in axillary lymph nodes
1610 drives metastases in breast cancer through complementary mechanisms. Nat Commun *11*, 404.

1611 Philippeos, C., Telerman, S.B., Oules, B., Pisco, A.O., Shaw, T.J., Elgueta, R., Lombardi, G., Driskell,
1612 R.R., Soldin, M., Lynch, M.D., *et al.* (2018). Spatial and Single-Cell Transcriptional Profiling Identifies
1613 Functionally Distinct Human Dermal Fibroblast Subpopulations. J Invest Dermatol *138*, 811-825.

1614 Porter, R.L., Magnus, N.K.C., Thapar, V., Morris, R., Szabolcs, A., Neyaz, A., Kulkarni, A.S., Tai, E.,
1615 Chougule, A., Hillis, A., *et al.* (2019). Epithelial to mesenchymal plasticity and differential response to
1616 therapies in pancreatic ductal adenocarcinoma. Proc Natl Acad Sci U S A.

1617 Puram, S.V., Tirosh, I., Parikh, A.S., Patel, A.P., Yizhak, K., Gillespie, S., Rodman, C., Luo, C.L., Mroz,
1618 E.A., Emerick, K.S., *et al.* (2017). Single-Cell Transcriptomic Analysis of Primary and Metastatic Tumor
1619 Ecosystems in Head and Neck Cancer. Cell *171*, 1611-1624 e1624.

1620 Qadir, M.M.F., Alvarez-Cubela, S., Klein, D., van Dijk, J., Muniz-Anquela, R., Moreno-Hernandez, Y.B.,
1621 Lanzoni, G., Sadiq, S., Navarro-Rubio, B., Garcia, M.T., *et al.* (2020). Single-cell resolution analysis of
1622 the human pancreatic ductal progenitor cell niche. Proc Natl Acad Sci U S A *117*, 10876-10887.

1623 Sade-Feldman, M., Yizhak, K., Bjorgaard, S.L., Ray, J.P., de Boer, C.G., Jenkins, R.W., Lieb, D.J., Chen,
1624 J.H., Frederick, D.T., Barzily-Rokni, M.*, et al.* (2019). Defining T Cell States Associated with Response
1625 to Checkpoint Immunotherapy in Melanoma. Cell *176*, 404.

1626 Sahai, E., Astsaturov, I., Cukierman, E., DeNardo, D.G., Egeblad, M., Evans, R.M., Fearon, D., Greten,
1627 F.R., Hingorani, S.R., Hunter, T.*, et al.* (2020). A framework for advancing our understanding of cancer-
1628 associated fibroblasts. Nat Rev Cancer *20*, 174-186.

1629 Schleger, C., Verbeke, C., Hildenbrand, R., Zentgraf, H., and Bleyl, U. (2002). c-MYC activation in primary
1630 and metastatic ductal adenocarcinoma of the pancreas: incidence, mechanisms, and clinical significance.
1631 Mod Pathol *15*, 462-469.

1632 Sholl, L.M., Do, K., Shivdasani, P., Cerami, E., Dubuc, A.M., Kuo, F.C., Garcia, E.P., Jia, Y., Davineni,
1633 P., Abo, R.P.*, et al.* (2016). Institutional implementation of clinical tumor profiling on an unselected cancer
1634 population. JCI Insight *1*, e87062.

1635 Siegel, R.L., Miller, K.D., and Jemal, A. (2020). Cancer statistics, 2020. CA Cancer J Clin *70*, 7-30.

1636 Somerville, T.D.D., Xu, Y., Miyabayashi, K., Tiriac, H., Cleary, C.R., Maia-Silva, D., Milazzo, J.P.,
1637 Tuveson, D.A., and Vakoc, C.R. (2018). TP63-Mediated Enhancer Reprogramming Drives the Squamous
1638 Subtype of Pancreatic Ductal Adenocarcinoma. Cell Rep *25*, 1741-1755 e1747.

1639 Spurr, L.F., Touat, M., Taylor, A.M., Dubuc, A.M., Shih, J., Meredith, D.M., Pisano, W.V., Meyerson, M.L.,
1640 Ligon, K.L., Cherniack, A.D.*, et al.* (2020). Quantification of aneuploidy in targeted sequencing data using
1641 ASCETS. Bioinformatics.

1642 Suva, M.L., and Tirosh, I. (2019). Single-Cell RNA Sequencing in Cancer: Lessons Learned and
1643 Emerging Challenges. Mol Cell *75*, 7-12.

1644 Tiriac, H., Belleau, P., Engle, D.D., Plenker, D., Deschenes, A., Somerville, T.D.D., Froeling, F.E.M.,
1645 Burkhart, R.A., Denroche, R.E., Jang, G.H.*, et al.* (2018). Organoid Profiling Identifies Common
1646 Responders to Chemotherapy in Pancreatic Cancer. Cancer Discov *8*, 1112-1129.

1647 Tirosh, I., Izar, B., Prakadan, S.M., Wadsworth, M.H., 2nd, Treacy, D., Trombetta, J.J., Rotem, A.,
1648 Rodman, C., Lian, C., Murphy, G.*, et al.* (2016a). Dissecting the multicellular ecosystem of metastatic
1649 melanoma by single-cell RNA-seq. Science *352*, 189-196.

1650 Tirosh, I., Venteicher, A.S., Hebert, C., Escalante, L.E., Patel, A.P., Yizhak, K., Fisher, J.M., Rodman, C.,
1651 Mount, C., Filbin, M.G.*, et al.* (2016b). Single-cell RNA-seq supports a developmental hierarchy in human
1652 oligodendroglioma. Nature *539*, 309-313.

1653 van Galen, P., Hovestadt, V., Wadsworth Ii, M.H., Hughes, T.K., Griffin, G.K., Battaglia, S., Verga, J.A.,
1654 Stephansky, J., Pastika, T.J., Lombardi Story, J.*, et al.* (2019). Single-Cell RNA-Seq Reveals AML
1655 Hierarchies Relevant to Disease Progression and Immunity. Cell *176*, 1265-1281 e1224.

1656 Venteicher, A.S., Tirosh, I., Hebert, C., Yizhak, K., Neftel, C., Filbin, M.G., Hovestadt, V., Escalante, L.E.,
1657 Shaw, M.L., Rodman, C.*, et al.* (2017). Decoupling genetics, lineages, and microenvironment in IDH-
1658 mutant gliomas by single-cell RNA-seq. Science *355*.

1659 Zhang, L., Li, Z., Skrzypczynska, K.M., Fang, Q., Zhang, W., O'Brien, S.A., He, Y., Wang, L., Zhang, Q.,
1660 Kim, A.*, et al.* (2020). Single-Cell Analyses Inform Mechanisms of Myeloid-Targeted Therapies in Colon
1661 Cancer. Cell *181*, 442-459 e429.

1662 Zilionis, R., Engblom, C., Pfirschke, C., Savova, V., Zemmour, D., Saatcioglu, H.D., Krishnan, I., Maroni,
1663 G., Meyerovitz, C.V., Kerwin, C.M.*, et al.* (2019). Single-Cell Transcriptomics of Human and Mouse Lung
1664 Cancers Reveals Conserved Myeloid Populations across Individuals and Species. Immunity *50*, 1317-
1665 1334 e1310.